Incoherent LADAR Detection Technique to Identify and Characterize Multilayer Samples at Long-Range Distances

Mémoire

MICHEL GOSSELIN

Maîtrise en génie électrique
Maître ès sciences (M.Sc.)

Québec, Canada

Résumé

Ce mémoire décrit le développement d'une technique incohérente de détection LADAR à l'aide d'une diode laser à longueur d'onde accordable afin d'identifier un échantillon multicouches à distance avec une résolution submillimétrique. Les principes de LADAR ainsi que les techniques d'interférométrie utilisés pour la détection d'un échantillon multicouches sont présentés. Par la suite, les concepts théoriques essentiels pour ce mémoire sont décrits, en particulier l'interféromètre à fréquence accordable, la comparaison des mesures prises en réflexion et transmission, et l'effet des mesures prises à un angle d'incidence. La phase expérimentale consistait en une série d'essais en laboratoire pour valider le montage expérimental, ainsi qu'un programme diversifié de mesures extérieures avec une multitude de configurations d'échantillons multicouches. Les résultats concluants démontrent la capacité d'identifier et de définir des échantillons multicouches à distances, incluant lorsque mesurés à un angle d'incidence.

Summary

This thesis outlines the development of an incoherent LADAR detection technique using a tunable laser diode source to identify and characterize multilayer samples with sub-millimeter resolution at long-range distances. The principles of LADAR and interferometry techniques currently being utilized to detect a stratified medium are first described. This is followed by the theoretical concepts that underline the work of this thesis, where in particular the frequency swept interferometer, the comparison of measurements performed in reflection versus transmission, and the effects of off-axis measurements are explained. The experimental phase consisted of a series of indoor tests to validate the experimental setup and the signal analysis code, and a wide-ranging outdoor measurement programme with numerous configurations of multilayer samples. The results successfully demonstrate the ability to identify and characterize multilayer samples at long-range distances, including when there is an angle of incidence on the substrate.

Table of Contents

List of Tables

List of Figures

List of Acronyms and Abbreviations

APD	Avalanche Photodiode
BS	Beam Splitter
COPL	Centre d'Optique, Photonique et Laser
DFB	Distributed Feedback
ECL	External Cavity Laser
EDFA	Erbium-Doped Fibre Amplifier
FFT	Fast Fourier Transform
FMCW	Frequency Modulated Continuous Wave
FOV	Field of View
FTIR	Fourier-Transform Infrared Spectroscopy
FTS	Fourier-Transform Spectrometer
FWHM	Full Width at Half Maximum
HP	Hewlett Packard
IFFT	Inverse Fast Fourier Transform
InGaAs	Indium Gallium Arsenide
IR	Infrared
LADAR	Laser Detection and Ranging
LIDAR	Light Detection and Ranging
MATLAB	Matrix Laboratory (numerical computing environment by MathWorks)
NASA	National Aeronautics and Space Administration
NIST	National Institute of Standards and Technology
OCT	Optical Coherence Tomography
OPD	Optical Path Delay
PMMA	Poly(methyl methacrylate)
PVB	Polyvinyl Butyral
RADAR	Radio Detection and Ranging
SLED	Super Luminescent Diode
SNR	Signal to Noise Ratio
SWIR	Short Wave Infrared
TEC	Thermoelectric Cooler

Acknowledgements

The pursuit of a post-graduate degree is a task that must not be taken lightly, especially when returning after years out of school. These last two years have been an enlightening learning experience. In addition to acquiring the required academic knowledge, I have learned a great deal about the problem solving and the discipline required to successfully complete a Master's degree.

First, I must acknowledge the Canadian Armed Forces and the Department of National Defence for the incredible opportunity that was offered to me to pursue a post-graduate degree.

I would like to thank my thesis advisor, Dr. Jérome Genest, for his continuous support and patience with me throughout the duration of my thesis. Without hesitation, he took me on as one of his graduate students and was always available to offer me assistance. I must also thank my co-thesis advisor, Dr. Simon Roy, for his guidance and encouragement during the last two years.

A special thanks goes out to Simon Levasseur, our laboratory technician, whom without his help, none of this would have been a success. His incredible work on this research project and willingness to teach me the basics of working in an optics laboratory were greatly appreciated.

Members of this remarkable research group, Jean-Daniel Deschênes, Simon Potvin, Sylvain Boudreau and Alex Côté, have also been a great help during my time at Université Laval. They offered constant support and were always willing to answer any of my questions.

Finally, I must also thank my family for their constant support and encouragement. In particular, I must thank my father for taking the time from his busy schedule to review this thesis on multiple occasions and whose comments were always welcomed.

1 Introduction

"Ipsa Scientia Potestas Est - Knowledge itself is power" – Sir Francis Bacon, 1597

1.1 General

The remote detection and identification of multilayer samples has been one of great interest – and research – in recent years for Université Laval.

As part of a research project pursued by Dr. Jérome Genest's group at Université Laval, the detection of multilayer samples was demonstrated using frequency combs for hyper spectral light/laser detection and ranging (LIDAR/LADAR) measurements. In the first series of experiments conducted in 2011-2012 at distances of 10m and 30m inside the laboratory, the goal was to demonstrate the successful detection of hard targets, aerosol and gas cells, as well as obtain the target's spectral signature and ranging information. One of the hard targets used was a high-density polyethylene bottle. Through signal analysis, it was observed that an additional peak on the target's interferogram was detected at what corresponded to be the bottle's thickness [1].

The second series of experiments were conducted in the fall of 2012 using the long-range setup from the Centre d'Optique, Photonique et Laser's (COPL) third floor remote sensing laboratory. The goal was the same as the first series of experiments, but at a distance of approximately 170m, to the roof of the Abitibi-Price Pavilion. The successful long-range detection of the polyethylene bottle's thickness subsequently initiated interest to detect multilayer samples through the use of frequency combs [2].

The frequency comb approach, however, resulted in some limitations and proved to be a complex experimental setup, which is what led to the desire to use a tunable laser as a source [3]. Additionally, as will be seen in Chapter 2, Historical Background, several commercially available products have been developed using various interferometry techniques with the goal of detecting a sample's thickness. Most of these products, however, are limited by their design as tabletop products.

1.2 Aim of Thesis

Due to the limitations and the setup complexity of using frequency combs to detect multilayer samples, a simpler and more robust setup was desired to perform their detection. The purpose of this thesis was therefore to develop a LADAR detection technique using a tunable laser diode source to identify and characterize multilayer samples at long-range distances. Additionally, to fulfill a field ability requirement, the experimental setup needed to be as small and inexpensive as possible. With the ability to perform long-range multilayer LADAR detection, such a product could prove to be an important instrument for police and military forces.

The objectives of this thesis can be stated as:

Use a simple and inexpensive tunable laser diode in order to:

1) Detect the thickness of the individual layers of a stratified medium;

2) Identify the number of layers;

3) Retrieve the total thickness;

4) Perform these measurements outdoors at a distance of approximately 170m; and

5) Perform these measurements away from specular reflection at high incidence angles.

It is expected that frequency modulated continuous wave (FMCW) LIDARs enable such detections, as hinted by the performance of laser sources used in devices such as the Bridger Photonics SLM series described in the following chapter. One original aspect of this thesis is the optimal use of scene characteristics to reduce the complexity of the detection setup, to a point where a small field able instrument is possible.

1.3 Scope of Thesis

In order to achieve these objectives, an indoor laboratory phase and an outdoor measurement campaign were conducted, as described in detail in Chapter 4. The indoor laboratory phase was critical and served to perform the initial designs of the experimental

setup, including the tunable laser source and the reference interferometer. Additionally, measurements of several multilayer samples were performed in the laboratory to serve as a proof of concept that the chosen techniques could be successful. The measurements would then be analyzed using MATLAB for thickness retrieval. Once completed, outdoor measurement experiments were performed, measuring a total of 10 samples of various layer combinations and thicknesses. The measurements were performed on the Université Laval campus during a two-week period at a distance of 170m with multiple angles of incidence being used.

1.4 Thesis Outline

This thesis is broken into six chapters. After this introductory chapter, Chapter 2 provides a brief review of LADAR systems and of several interferometry techniques used for multilayer detection, as well as previous research and experiments conducted in this area of study. This is followed in Chapter 3 by a description of the main theoretical concepts that underlie the work undertaken in this thesis. The experimental setup, its various components and the complete test programme are described in detail in Chapter 4. The results of the measurements, performed both indoors and outdoors, are provided and analyzed in Chapter 5. A short concluding chapter summarizes the main findings of this thesis, along with recommendations and proposals for further study and research.

1.5 Relevant Introductory Notes

For this thesis, metric units are used throughout this document, as all measurements were taken in metric units; the only exception is for identifying original product specifications, which are listed in accordance in the manufacturer's imperial units (with converted metric units in bracket).

From a terminology standpoint, LIDAR is typically associated with terrain mapping or atmospheric information collection whereas LADAR is used for the location and characterization of small point targets like vehicles. LADAR is the main application studied in this thesis.

2 Historical Background

The following chapter will provide a review of the background, fundamentals and applications of LADAR systems followed by key interferometry techniques that have been applied in recent years to detect multilayer samples. Finally, commercially available products and previous experiments conducted for the detection of multilayer samples are presented to conclude the chapter.

2.1 Laser Detection and Ranging

2.1.1 LADAR Background

The relentless quest to collect information about potential enemies contributed significantly to the development of radio detection and ranging (RADAR) systems by multiple nations before and during the Second World War. Initially designed to provide vital advance information with regards to the detection and tracking of air, ground and sea targets for the military, this technology evolved to the point where it is currently being used for air traffic control, airborne collision avoidance systems, marine navigation, short-term weather forecasting as well as vehicle speed monitoring by law enforcement [4]. These technical developments, which contributed to the expansion of RADAR applications, progressively led to the research on different wavelength ranges for the transmitted signal, first in the 50cm range and later down into the millimeter and microwave regions [5].

The first instance of pulsed light sources and optical detectors being used was in 1938 when the base height of clouds was measured. With the development of Q-switched pulsed lasers in 1962, these sources became available for LIDAR applications [5]. The National Aeronautics and Space Administration (NASA) Apollo 15 mission to the Moon in 1971, where astronauts used a laser altimeter to map the surface of the moon, eventually led to the demonstration of the technology's accuracy and usefulness [6].

2.1.2 LADAR Fundamentals

Similar to RADAR systems, LADAR functions by transmitting and receiving electromagnetic energy; the difference being the frequency band in which the system operates. The laser's wavelength, ranging from 250nm to 11μm, is selected based on such factors as the target's material properties and atmospheric propagation windows. Launching the photons towards the target is usually accomplished through the use of a

beam expander or a telescope. The telescope is also used to collect the returning photons and a photodiode allows the conversion of these photons to an electrical signal. This light-induced current of the photodiode is proportional to the intensity of the incident radiation and is the signal that is transferred to other subsystems within the receiver [5,7]. Figure 1 provides a simplified graphical representation of a typical LADAR arrangement, with these same key components being utilized in this thesis' experimental setup, as seen in Chapter 4.

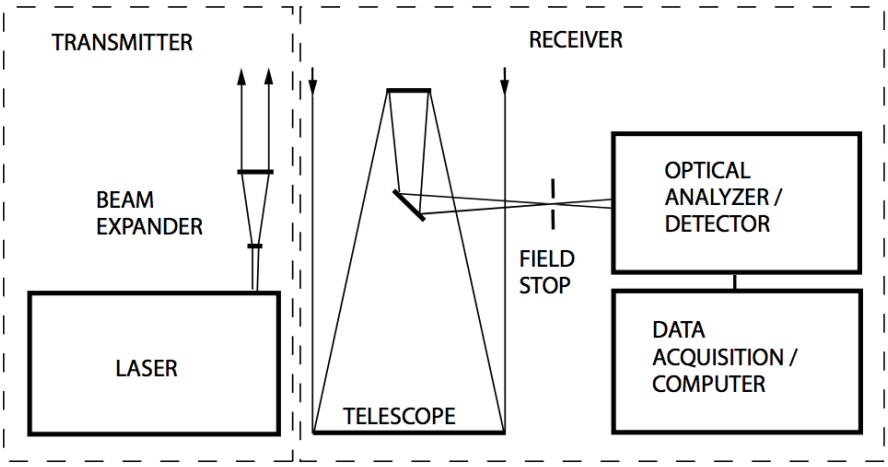

Figure 1 – Principal Setup of a LADAR System, from [7].

Finally, just like RADAR systems, LADAR often utilizes the well-known relationship between the range, R, and the round-trip time, t, of electromagnetic energy travelling at the speed of light in free space, c [7]:

$$t = \frac{2R}{c}. \tag{1}$$

2.1.3 LADAR Applications

LADAR has become an extremely popular technology, with an ever-increasing number of applications being developed each and every day. Such applications include the use of airborne mounted LADAR systems for high-resolution digital elevation maps for the purpose of geomorphology[1] as well as the analysis of canopy heights, biomass measurements and leaf area for forestry studies [8]. A visual demonstration of the application of an airborne mounted LADAR system is shown in Figure 2. LADAR systems have also been used in the fields of agriculture [9], archaeology [10], autonomous vehicles

[1] Branch of geoscience concerned with the evolution of Earth's surface topography.

[11], meteorology and atmospheric environment [12], astronomy, robotics as well as spaceflight [13]. The combination of a LADAR system with interferometry features has been a field of interest for many researchers and companies, and is one foundation behind this thesis.

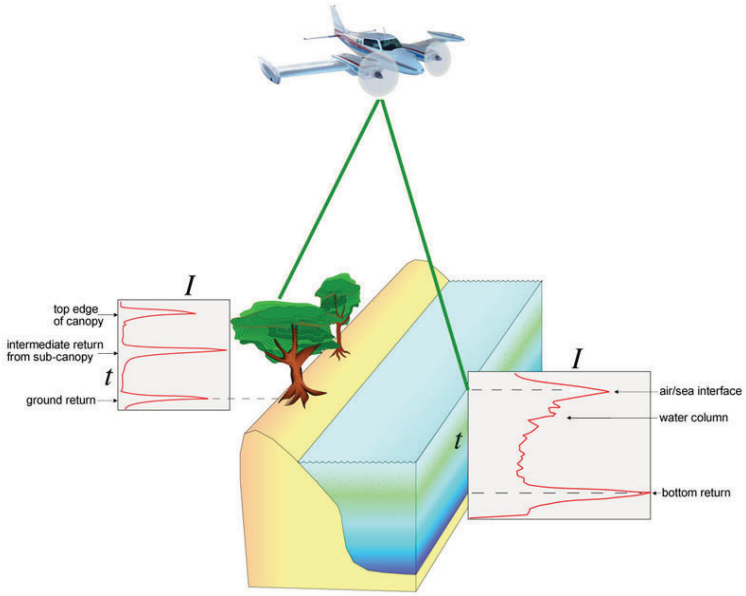

Figure 2 – Application of Airborne LADAR for Terrain Mapping, from [14].

2.2 Interferometry

2.2.1 Basic Principles of Interferometry

Optical interferometry is a technique currently being used in numerous fields including, but not limited to, the accurate measurement of distances, displacements and vibrations; test of optical systems; studies of surface topography, measurements of temperature, pressure and electrical and magnetic fields; high-resolution spectroscopy as well as medical imaging. The fundamental concept behind interferometry is the utilization of the principle of superposition, along with a quadrature detector, to combine waves in order to extract useful information about the optical field [15]. This concept is further explained in Chapter 3.

With the numerous applications of optical interferometry currently being employed, Fourier-transform spectroscopy (FTS), optical coherence tomography (OCT) and frequency modulated continuous wave LADAR (FMCW LADAR) are of immediate interest for the experimental programme of thesis, and are discussed below.

2.2.2 Fourier-Transform Spectroscopy

The Fourier-transform spectrometer is an instrument that allows the light spectral information to be retrieved by performing a Fourier analysis on a measured interference signal. It essentially uses a Michelson-type interferometer with a movable mirror. In a Michelson interferometer, an incoming light wave is divided into two paths, reflected back with one beam being retarded with respect to the other, and subsequently recombined. Allowing the translation of one of the mirrors and measuring the interference condition for many discrete positions of the mirror, one is able to capture the intensity of the interference as a function of the optical path delay (OPD). The interference signal measured, also known as the interferogram, is an estimate of the optical field autocorrelation. Its spectrum can thus be calculated using the Fourier transform as stated by the Wiener-Khintchine theorem [16]. Figure 3 presents the typical setup of an FTS system.

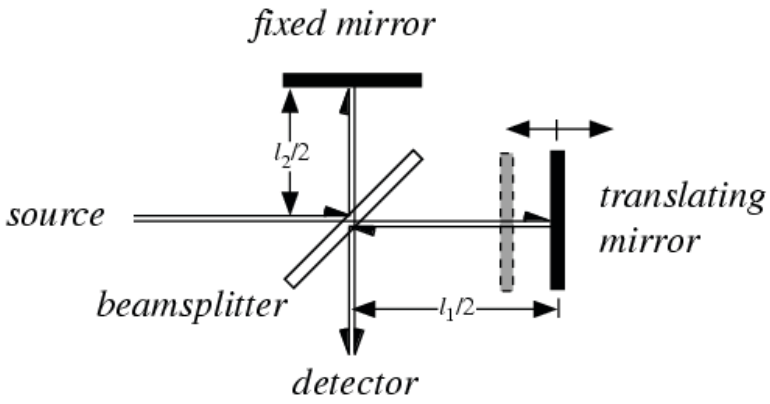

Figure 3 – Fourier-Transform Spectrometer Setup, from [17].

Through the use of an FTS system on an infrared (IR) spectrum, the absorption (or emission) lines can be studied to provide information with regards to the geometric structure of molecules, as well as their rotational and vibrational behaviour. Using this information, through the spectral signatures, a sample's chemical composition or even the composition of a distant star can be identified [18,19]. Figure 4 provides the graphical representation of interferogram and the spectrum obtained of the α Herculis star, with the Fourier transform being the link between the two.

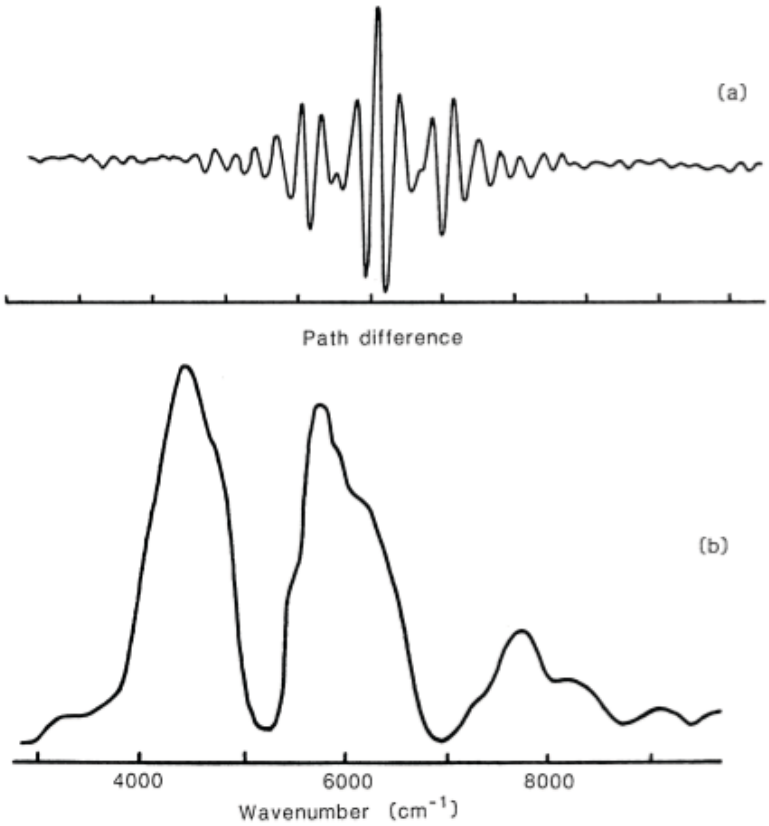

Figure 4 – (a) The Interferogram and (b) the Spectrum Obtained of the 3.5 Magnitude, α Herculis, from [15].[2]

2.2.3 Optical Coherence Tomography

Another field of study for interferometry is OCT, which has been utilized for the detection of multilayer samples. With this denomination, it was initially conceptualized as a medical imaging technique using low-coherence interferometry to provide tomographic visualization of biological tissue, in particular the human eye. Figure 5 displays the results of the OCT scan of a human retina. At the core of an OCT system is also a Michelson interferometer. It is however used to determine the depth profile of a sample. Low-coherence interferometry through the use of broadband light source (i.e. super luminescent diodes (SLED)) enables OCT systems to achieve sub-micrometer resolution, making them perfect for biomedical imaging applications [20].

[2] While not identified, the interfogram path difference is typically identified in cm.

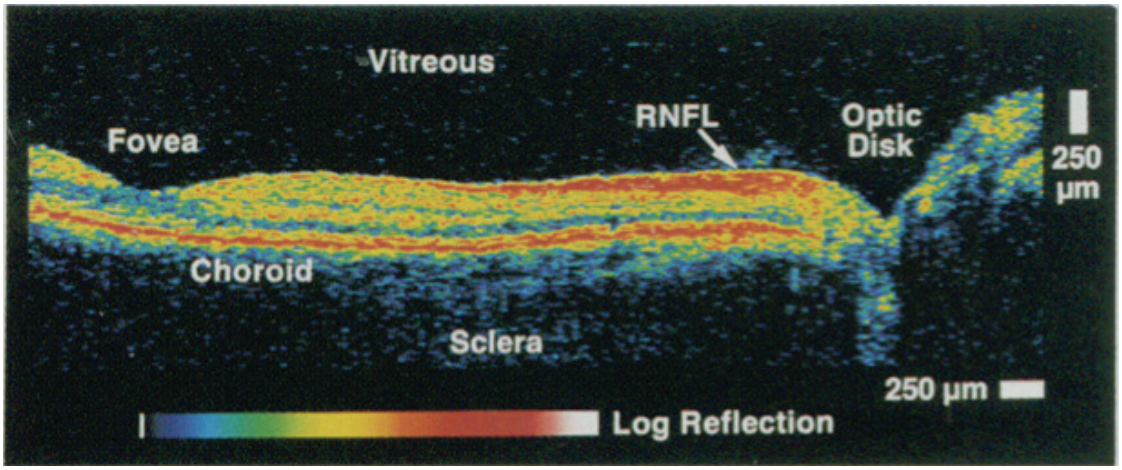

Figure 5 – OCT Scan of Human Retina Along the Papillomacular Axis, from [21].

As seen in Figure 6, an OCT system functions by having light split into two arms – a sample arm (containing the sample under test) and a reference arm (typically a mirror). The combination of the reflected light between the sample and the reference arm produces an interference pattern when light from both arms travel the same OPD, and this within the source coherence length [22]. By allowing the reference mirror to scan, the reflected optical data from each point is detected as an interference pattern and recorded as a depth profile. Scanning the probe across the sample will generate a cross-section and combining multiple cross-sections will allow 3D volumetric images to be created [23].

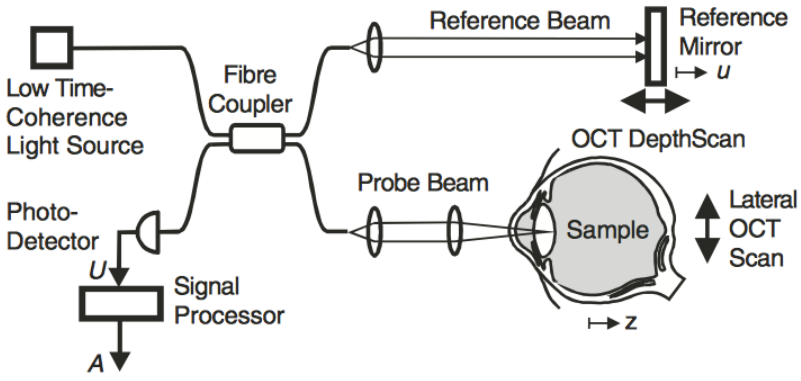

Figure 6 – Time Domain OCT in Fibre Optics Technology, from [24].

A variation of OCT that is of great interest is a swept source OCT (also known as a time encoded frequency domain OCT). Rather than using a super luminescent diode and a moving mirror, one fixes the position of the reference mirror and uses a frequency sweeping laser source. The detector captures the spectrum of the interference pattern as

a function of time and the Fourier transform allows the conversion of this spectrum to the interferogram in the OPD domain. From this perspective, the frequency swept OCT is the Fourier transform of a Fourier-transform spectrometer. In an FTS, the interferogram is acquired and Fourier transformed to get the desired spectrum. In a frequency swept OCT, the complex spectrum is acquired and transformed to obtain the desired interferogram.

As will be discussed in the following chapters, this same technique will be utilized for the detection of multilayer samples. The benefit of this technique lies in the high signal-to-noise ratio (SNR) detection and the system's ability to perform and maintain sensitivity at high scanning speeds (> 20 kHz) [23]. These benefits were further highlighted in 2003 when researchers from the University of Vienna presented a study of the noise sources observed in Fourier domain OCT (FDOCT) setups compared to the time domain OCT systems. Their work demonstrated how FDOCT systems had a large sensitivity advantage when compared to time domain OCT and allowed for sensitivities well above 80dB, even in situations with low light levels and high-speed detection [25].

In addition to the medical field, OCT has also become an increasingly prevalent technology in industrial applications such as non-destructive testing, art diagnostics, penetration depths in various polymer materials as well as thickness measurements of thin silicon wafers [26]. Several commercially available products make use of this technology for the tabletop detection of multilayer samples.

2.2.4 Frequency Modulated Continuous Wave LADAR

A variation of LADAR systems that has gained prominence in recent years and that utilizes interferometry is FMCW LADARs. Just like its RADAR counterpart, FMCW LADARs function the exact same way as the classical parallel-beam Michelson interferometer with the exception that the light source is a frequency-modulated laser. The beat signal produced by the recombination of the two reflected beams, shown in Figure 7, allows for the measurement of the frequency and the phase of the beat signal, which enables the determination of the distance, displacement and speed of the target [27].

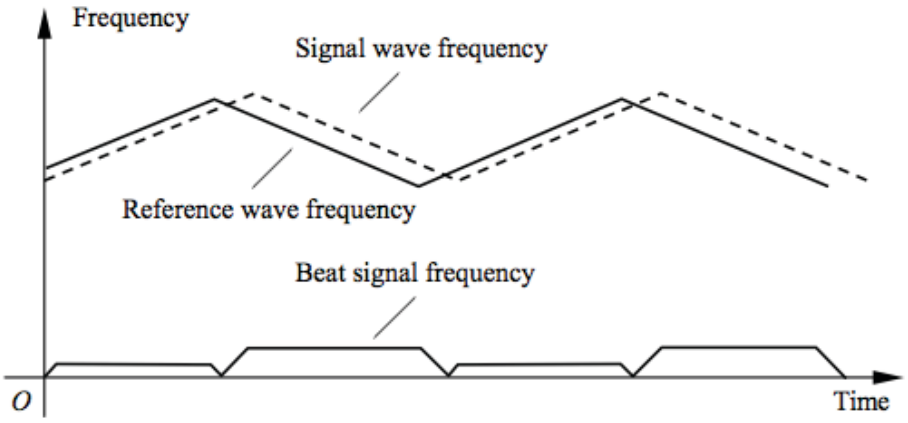

Figure 7 – Frequency-Time Relationship in FMCW LADAR, from [27].

One shall note that FMCW and OCT are in fact the same technique, but applied to two different domains. The recent advent of narrow line width tunable lasers enabled the use of coherent reflectometry over longer ranges, hence allowing the migration from biomedical applications, where few millimeters of coherent length are required, to remote sensing, where hundreds of meters to kilometers are needed [28]. For the FMCW coherent LADAR systems requiring a long coherence length, this implies high quality, complex and expensive lasers. These lasers are required to have a narrow line width and be tunable on a large range. As such, the laser is required to be coherent with itself once recombined. The laser's coherence time can be defined as [24]:

$$\tau_c = \frac{L_c}{c} = \frac{1}{\Delta f}, \qquad (2)$$

where L_c is the coherence length, c the speed of light in vacuum and Δf is the laser's line width in Hertz.

For example, to be able to successfully probe a target at a distance of 1km requires a laser to have a line width smaller than 300kHz. As will be seen in the following chapter, the resolution is dependent on the tuning range of the laser. Using Eq. (16) provided further below, one finds that achieving 1mm resolution with a laser operating at 1550nm requires a tuning range of 1.125nm. The laser line width and tuning range are two critical characteristics that will be of significance when performing long-range measurements of multilayer samples for this thesis.

Many experiments have been recently performed to maximize the benefits of FMCW LADARs. In 1994, Dieckmann demonstrated the implementation of a FMCW LIDAR using a tunable twin-guide laser diode. The use of twin-guide laser diode allowed a large continuous tuning range of the emission frequency. This frequency tuning range of 230GHz thus produced highly accurate distance measurements [29]. At about the same time that Dieckmann was publishing his work, Nöding and Amann pursed this aspect further by exploring the influence of the tuning behaviour on the distance measurement, ultimately demonstrating that the non-linear characteristic had to be corrected for high-speed applications [30].

In addition, in an article published in 2008, NASA reported on their work exploring the development of an all-fibre linear FMCW laser RADAR to perform high-resolution range measurements, as well as their attempts to obtain high precision horizontal and vertical velocity measurements. Their experimental setup was designed in order to take advantage of the system's ability to measure directly the platform velocity by extracting the Doppler shift generated from the motion. The goal of their experiment was to satisfy their space exploration initiative, which would require landing a spacecraft at locations with high scientific value [31]. More recently, two researchers from the University of Kansas, Gao and Hui, pursued a FMCW LIDAR for heterodyne detection, utilizing an electro-optic I/Q modulator to generate carrier-suppressed and frequency-shifted FM modulation. They were able to demonstrate that such a technique allowed for the use of a much wider modulation bandwidth to improve range resolution [32].

Finally, in 2013, several researchers from the National Institute of Standards and Technology (NIST) were able to demonstrate a comb-calibrated FMCW LADAR system for absolute distance measurements. Their system, shown in Figure 8, used a compact external cavity laser (ECL) that was swept quasi-sinusoidally over 1THz at a 1kHz rate. They simultaneously recorded the heterodyne FMCW laser signal and the instantaneous laser frequency at sweep rates up to 3400THz/s, as measured against a free-running frequency comb. By demodulating the instantaneous laser frequency, they were able to obtain the range to the target with 1ms update rates, bandwidth-limited 130μm resolution (ΔR) and approximately 100nm accuracy that was directly linked to the counted repetition rate of the comb. The experiments performed by the NIST researchers demonstrated how a large optical bandwidth greatly increased the resolution compared to typical LADAR

systems. Moreover, the coherent detection lead to a shot-noise limited SNR and extremely high range precision of approximately ΔR/SNR [33].

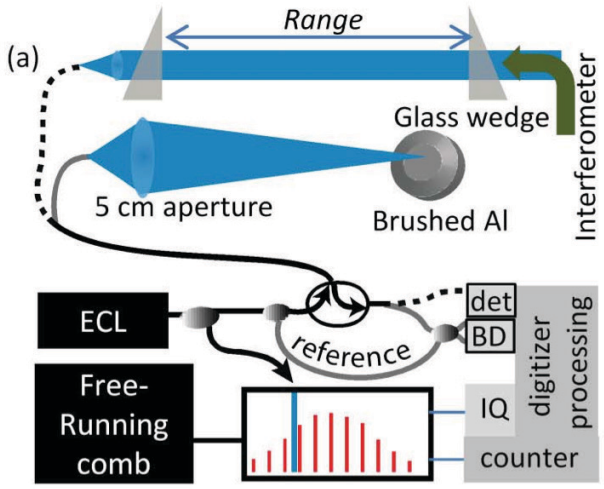

Figure 8 – Experimental Setup of NIST's Comb-Calibrated FMCW LADAR System, from [33].

The results of all these experiments with FMCW LADARs, in particular the tuning range for accurate measurements and high resolution, would factor significantly into the design of this thesis' experimental setup.

2.3 Multilayer Detection

The following sub-section presents multiple commercially available products that utilize interferometry for non-contact thickness measurements, in addition to previous experiments conducted for the detection of multilayer samples.

2.3.1 Commercially Available Products for Multilayer Detection

There are already many commercially available products that benefit from non-contact thickness measurements. Lumetrics Inc. produces the OptiGauge MLS, a precision multilayer thickness measurement system that is capable of providing the thickness of up to 20 individual layers as well as the total overall thickness through the use of low-coherence interferometry and a SLED. The OptiGauge MLS is capable of determining the thickness of a sample measuring from 12μm to 8mm [34].

Also employing low-coherence interferometry, Novacam Technologies Inc., which manufactures high-precision optical metrology systems for 3D non-contact inspection and

imaging, developed their own thickness measurement system titled MicroCam. MicroCam, shown in Figure 9, is a fibre-based optical non-contact 3D profilometer capable of delivering thickness, roughness and vibration measurements as well as high-speed surface and cross-sectional inspections. This profilometer is capable of measuring samples ranging from 10µm to 8mm from a standoff distance of up to 100mm [35]. Finally, Filmetrics Inc. has multiple products capable of measuring thin-film thickness through the use of spectral reflectance. Their F70 thin-film analyzer is limited to two-layer samples ranging from 0.5mm to 15mm from a working distance of 21mm [36].

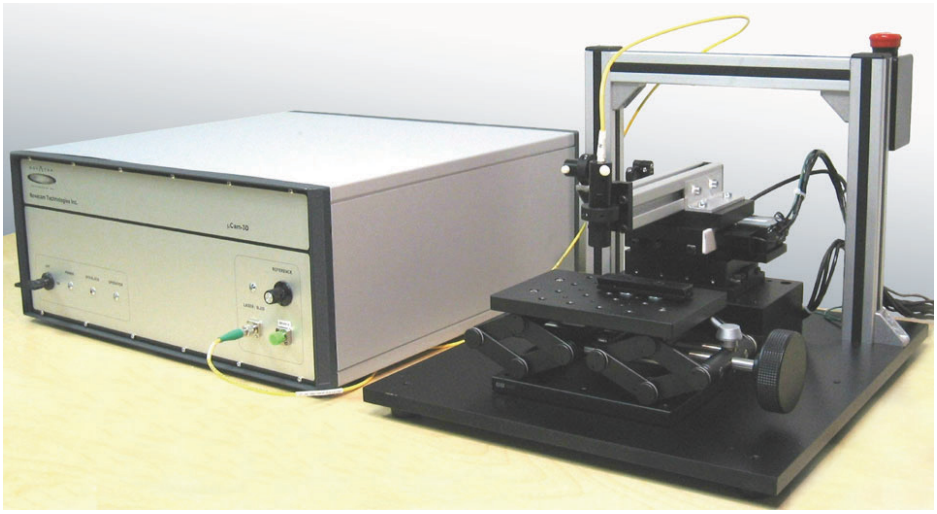

Figure 9 – Novacam Inc.'s MicroCam Profilometer, from [35].

These are all products that are typically used to measure the thickness of multilayer films, semiconductor wafers, as well as employed for quality assurance. The difference between these products and the experimental setup of this thesis lies in the long-range detection, since these products are all considered tabletop instruments. In addition to measuring the samples at long distances and at an angle, the samples measured for this thesis typically have larger thicknesses. It also can't be assumed that the sample will be cooperative when performing the measurements, i.e. the user will not always have complete control over all the sample and its alignment.

Bridger Photonics, a leader in precision LIDAR/LADAR and advanced imaging systems, has recently developed the SLM Series, an absolute distance measurement system based on the principles of FMCW LADAR as well as swept source OCT. Through

the use of a frequency swept laser source, they are able to interferometrically combine the returned light from the sample of interest with a local oscillator to coherently determine the distance. The SLM Series is capable of providing measurements for target detection, surveying, 3D and surface mapping as well as wafer thickness. The SLM is also capable of resolving multiple targets on the same line of sight with a specification of 1.5mm full width at half maximum (FWHM) at a distance of 10km. It is capable of achieving such resolution at long range by employing a laser with an extremely narrow line width of approximately 30kHz and sweeping over a bandwidth of 100GHz [37]. This is an extremely interesting product that utilizes the same fundamental concept of this thesis, a swept laser source for performing interferometry measurements. The work presented here will however use techniques that make possible the use of lasers having a much larger line width, reducing the cost and complexity while increasing the robustness and field ability.

2.3.2 Previous Experiments of Multilayer Detection

Multiple attempts have been made for the detection of a stratified medium sample, using a variety of techniques. Time-domain OCT was used in 1971 by Patten to measure the separation between glass plates [38]. In 1992, experiments by researchers Sorin and Gray using optical low-coherence reflectometry were conducted to determine the physical thickness and group index of a sample. Using a Michelson interferometer setup, they were able to take two optical path length measurements to determine both the physical distance and group index of an unknown sample. These measurements were accomplished by placing the device under test in between the probe and a fixed mirror whose location was known from a previous reflectometry scan, shown on Figure 10. A new reflectometry scan then measured the locations of the front and back surfaces of the sample and the apparent displaced location of the mirror. These optical path distances provided the information necessary to solve for both the sample thickness and its group index. Fused silica samples of 9mm and 12mm were successfully measured using this experimental setup [39].

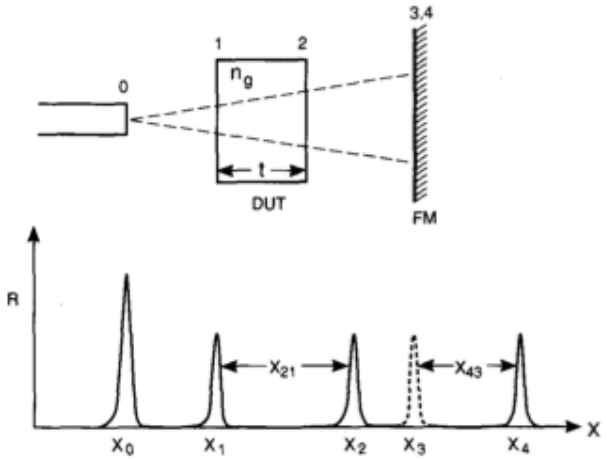

Figure 10 – Arrangement Used to Measure the Thickness and Group Index of the Device Under Test, from [39].

Several Italian researchers demonstrated a new method for measuring the refractive index and the thickness of transparent plates in 2003. Their setup consisted of employing a finely tuned distributed feedback (DFB) diode laser source to introduce a phase shift into the detected signal, and subsequently rotating the sample to produce a variable lateral shear. As seen on Figure 11, a collimated beam from a DFB laser diode traveled through the sample under investigation. The laser diode's wavelength was tuned through temperature variations over a range of 0.76nm. Following an even number of reflections at the sample-air interfaces, the emerging wave fronts were laterally sheared, with a shear that was dependent on the angle of incidence. When the sample was rotated at a constant angular speed, -25^{o} to $+25^{o}$ for these experiments, the intensity detected was a chirped interference signal. Through the use of either a phase-shifting algorithm or a fast Fourier transform, they were able to analyze the interferometric signal and determine the thickness and refractive index of the sample. Capable of detecting samples measuring 500µm, their lateral-shear, wavelength-scanning interferometer was, however, limited to only measuring single-layer structures [40].

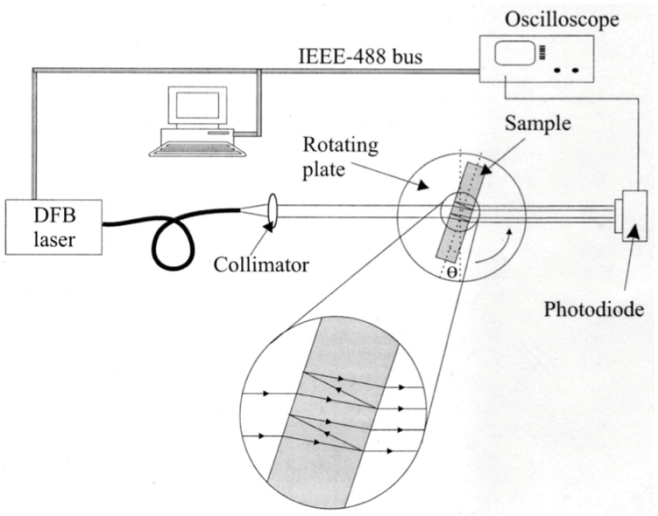

Figure 11 – Experimental Setup for Determining both Refractive Indices and Thicknesses of Transparent Plates, from [40].

In 2008, scientists from the Gwangju Institute of Science and Technology successfully demonstrated the simultaneous measurements of the phase index, group index and geometrical thickness of an optically transparent object by combining optical low-coherence interferometry and confocal optics. The low-coherence interferometer was used to obtain the geometrical thickness and group index of the measured sample, and the confocal optics allowed the ratio of the thickness to the phase index to be obtained. As seen on Figure 12, a collimated beam from a SLED was launched to a beam splitter (BS) and split into the reference and sample arms. They began by shifting the objective lens in the sample arm (OBJ1) to have its focal point on the front surface of the sample and positioning the reference arm objective lens (OBJ2) and the reference mirror (RM) to obtain maximum interference contrast. Subsequently, OBJ1 was moved closer to the sample so that its focal point was located on the rear surface of the sample, providing the confocal distance Δz. The RM was then shifted to have another maximum interference contrast resulting from the rear surface of the sample, which gave the low-coherence distance $\Delta\ell$. These two distances, along with the numerical aperture of OBJ1, were then utilized to determine the three sample parameters. Samples of BK7 and fused silica were measured with thicknesses up to 5.1mm [41].

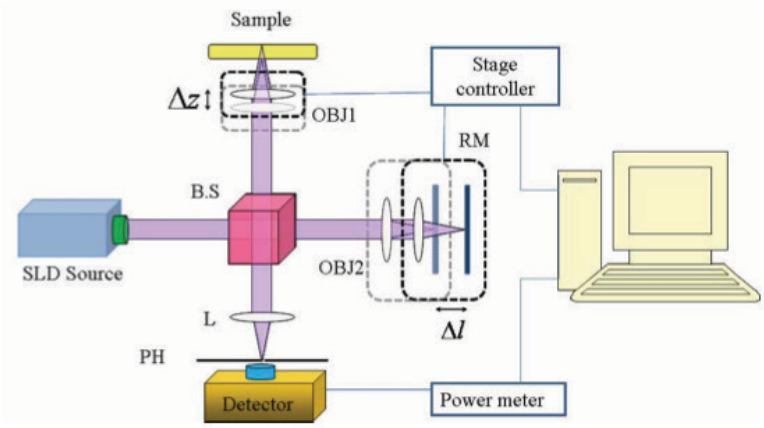

Figure 12 – Schematic of the Experimental Setup Based on a Low-Coherence Interferometer and Confocal Optics, from [41].

In addition, as part of her 2010 Master's thesis at Université Laval, Geneviève Taurand was able to demonstrate the detection of four cover slides stacked on top of a microscope glass slide using an OCT setup with dual-comb interferometers [42]. During the same timeframe, Italians Fathi and Donati were able to conduct experiments that demonstrated the use of a single and two-channel self-mixing interferometer to detect the thickness and refractive index of transparent plates. To accomplish their experiments, the reflected beams retraced the forward path back to the laser cavity and were received by the photo detector placed behind the laser diode, shown on Figure 13. The optical phase shift was measured by a self-mixing interferometer as a function of the angle of incidence on the sample. To simultaneously determine the thickness and the refractive index, analysis of the derivative of the phase difference with respect to the rotation angle was performed. While capable of performing measurements at angles up to 65^{o}, their measurements were limited to samples thinner than 1mm placed at a distance of 20cm [43,44].

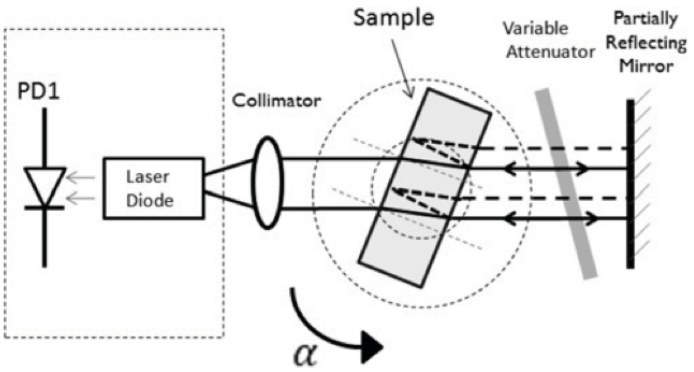

Figure 13 – Experimental Setup Used for Self-Mixing Interferometer, from [44].

Finally, in 2012, researchers from the National Institute of Lasers and Optronics in Pakistan and the University of North Carolina were able to use femtosecond and terahertz pulses to simultaneously determine the thickness and refractive index of parallel-plane samples. The time-of-flight measurements of the pulses with and without the sample were exploited to determine these parameters. They were successfully capable of measuring samples of fused silica and BK7 measuring up to 10.18mm from a distance of 30cm and at angles up to 45^{o} [45].

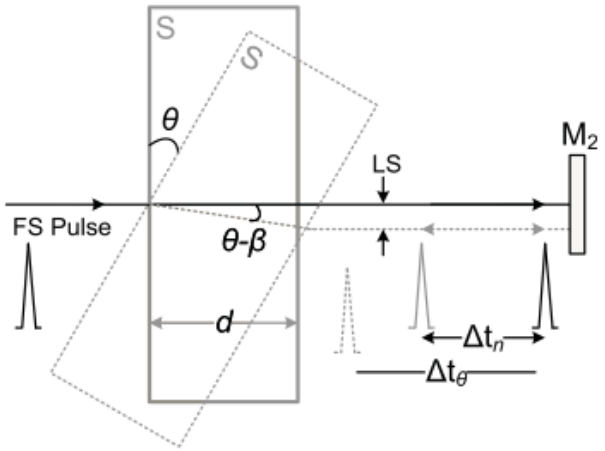

Figure 14 – Schematic Showing Relative Delays in the Femtosecond Pulse when Sample is Inserted at Normal and at an Angle θ, from [45].

With the exception of Bridger Photonics' SLM Series, the commercially available products and the experiments mentioned above were restricted to laboratory measurements with collaborative samples, often with mirrors to return the light after passing it through the sample. Little if no experiment performed multilayer detection and identification at long range. This thesis aims partly to address this gap.

3 Theoretical Concepts

In this chapter, the main theoretical concepts and mathematical tools underlying the work of this thesis are reviewed, with particular emphasis on the retrieval of the peaks leading to the layer thickness detection. This review is best achieved starting with the frequency swept interferometer.

3.1 Frequency Swept Interferometer

The frequency swept interferometer used in this thesis is defined by two key characteristics which stand out in comparison to previously mentioned OCT and FMCW LADAR setups: the detection method and the spatial resolution. As such, the selection of the laser source and the type of detection are critical to the successful retrieval of the individual layer thicknesses.

3.1.1 Coherent Detection Method

A coherent measurement, shown in Figure 15, refers to mixing, while preserving a deterministic phase relation, the field that probed the sample of interest with the field of an internal source, often called the local oscillator. In this type of measurement, similar to those of OCT and FMCW LADAR systems, the intensity and phase of the field of interest are capable of being measured, provided the same parameters of the local oscillator are known. This detection method allows the complex transfer function of the sample in the frequency domain to be measured, and the impulse response to be computed using the inverse Fourier transform [3].

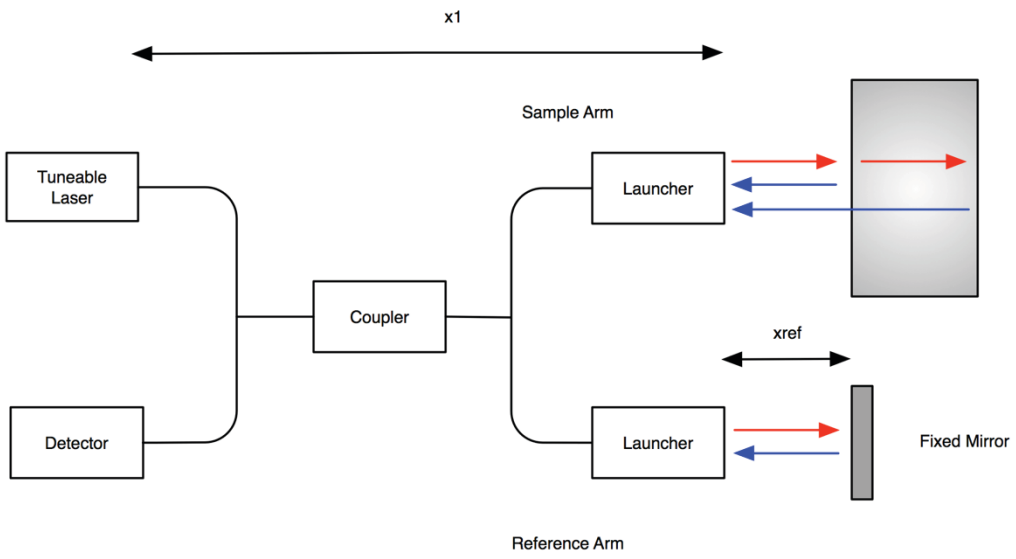

Figure 15 – Coherent Detection Method.

The concept of a coherent detection can be understood by considering the phasor of the field traveling in each arm of the instrument. The field that travels in the reference arm, prior to being recombined in the fibre coupler, can be defined as [3]:

$$E_{ref}(\omega) = E_{in} e^{jx_1\omega/c} \frac{e^{j3\pi/4}}{\sqrt{2}} e^{j2x_{ref}\omega/c}, \quad (3)$$

where E_{in} is the initial field emitted by the source at a particular frequency ω, x_1 is the propagation distance between the source and the coupler and x_{ref} is the propagation distance in the reference arm after the coupler (the factor 2 accounts for the round-trip in the arm). The 3π/4 and the square root of two arise from the interaction with a perfect coupler separating the intensity in half.

The field in the sample arm can be written as:

$$E_{sample}(\omega) = E_{in} e^{jx_1\omega/c} \frac{e^{j\pi/4}}{\sqrt{2}} H(\omega), \quad (4)$$

where H(ω) is the sample transfer function at the frequency ω. The light reflected from the sample and the reference arm are subsequently recombined within the coupler, with the output field defined as:

$$E_{out}(\omega) = \frac{1}{\sqrt{2}} \left(E_{sample}(\omega) \frac{e^{j3\pi/4}}{\sqrt{2}} + E_{ref}(\omega) \frac{e^{j\pi/4}}{\sqrt{2}} \right), \quad (5)$$

$$E_{out}(\omega) = \frac{E_{in}}{2} e^{jx_1\omega/c} e^{j\pi} \left[H(\omega) + e^{j2x_{ref}\omega/c} \right]. \quad (6)$$

The current measured by the detector is therefore:

$$I_{out}(x_{ref}, \omega) = \frac{|E_{out}(\omega)|^2}{2\eta}, \quad (7)$$

$$I_{out}(x_{ref}, \omega) = \frac{1}{2\eta} \frac{|E_{in}(\omega)|^2}{4} \left[|H(\omega)|^2 + H(\omega) e^{-j2x_{ref}\omega/c} + H(\omega)^* e^{j2x_{ref}\omega/c} \right], \quad (8)$$

where η is the impedance. The complex transfer function of the sample can be measured, in amplitude and phase, on the term modulated by the complex exponential $e^{-j2x_{ref}\omega/c}$. This term can be isolated through a filtering process to obtain:

$$\tilde{I}_{out}(x_{ref}, \omega) = \frac{I_{in}(\omega)}{4} H(\omega) e^{-\frac{j2x_{ref}\omega}{c}}. \quad (9)$$

By scanning the wavelength of the tunable laser, one can thus measure frequency by frequency the transfer function of the sample multiplied by the intensity of the source modulated on a complex exponential depending on the reference arm's length. By computing the inverse Fourier transform of measured signal, the desired impulse response, h(t), is retrieved which provides the necessary information to determine the thickness of the sample under test.

When considering the coherent measurement of a stratified medium, each interface of the medium will return light with a different path length and interfere with the light from the reference arm. In all cases, this information is held in h(t). This type of result is shown in Figure 16 for a 10cm sample with a refractive index of 1.5 located at a distance of 15cm from the launcher. The sample's transfer function modulus, $|H(\sigma)|$, is displayed in wavenumbers. The impulse response, computed using the inverse Fourier transform (IFFT) of $H(\sigma)$, is shown in Figure 17, where the absolute distance of the sample is measured and calculating the difference between the two peaks retrieves the sample's thickness.

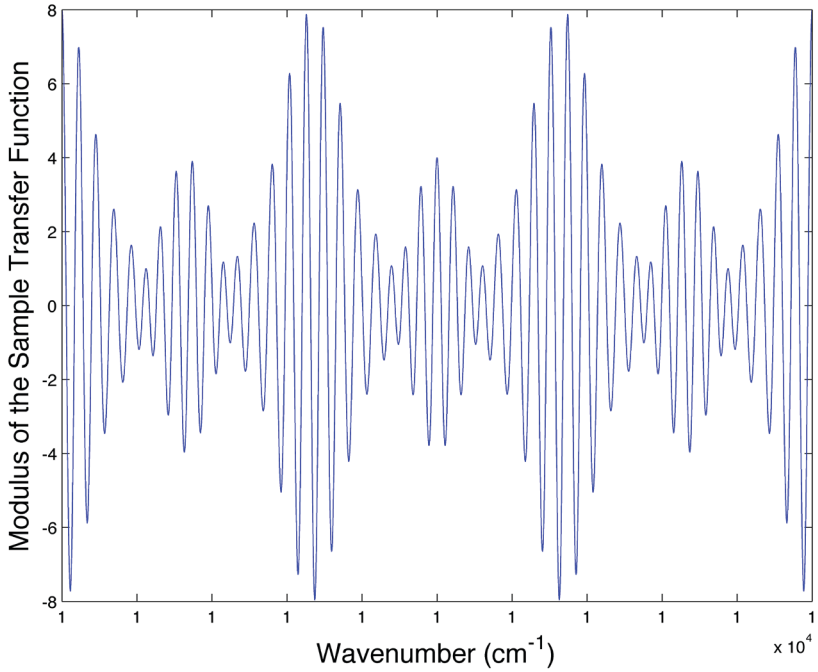

Figure 16 – Example of $|H(\omega)|$ for a 10cm Sample Using the Coherent Detection Method.

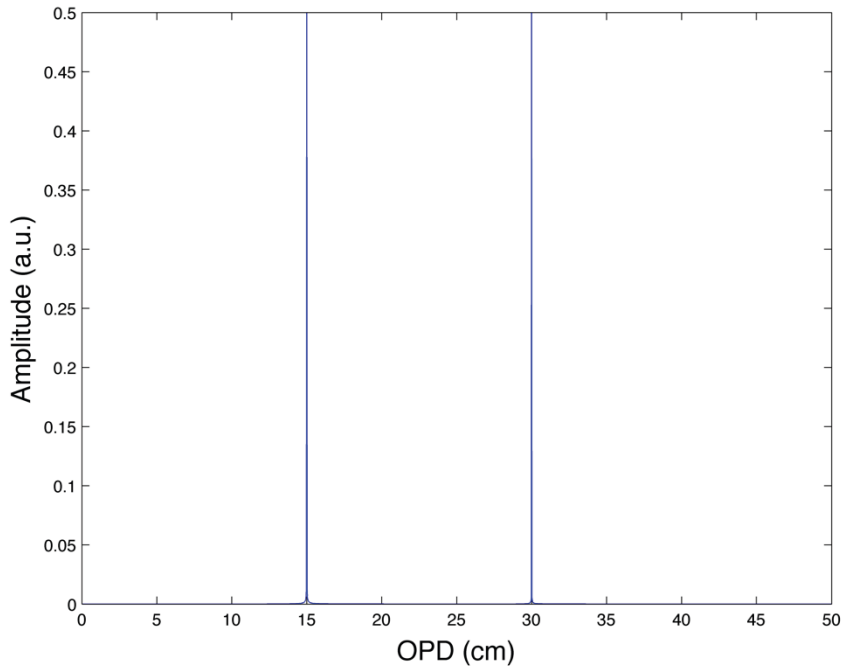

Figure 17 – Impulse Response for a 10cm Sample Using the Coherent Detection Method.

3.1.2 Incoherent Detection Method

In contrast, an incoherent measurement, shown in Figure 18, implies that there is no further mixing prior to detection and only the intensity of the field of interest is obtained since the field is directly sent to a square law detector. In such a detection method, both phasor fields are multiplied by the scene transfer function and one can show by following a development similar to the one presented in the preceding section that the transfer function square modulus is detected on the interference term. This means that the measured interferogram (or the inverse Fourier transform of the amplitude spectrum) is the autocorrelation of the sample's impulse response. The autocorrelation will thus have a main peak at the zero path delay (ZPD) and two side peaks corresponding to the sample's thickness [3].

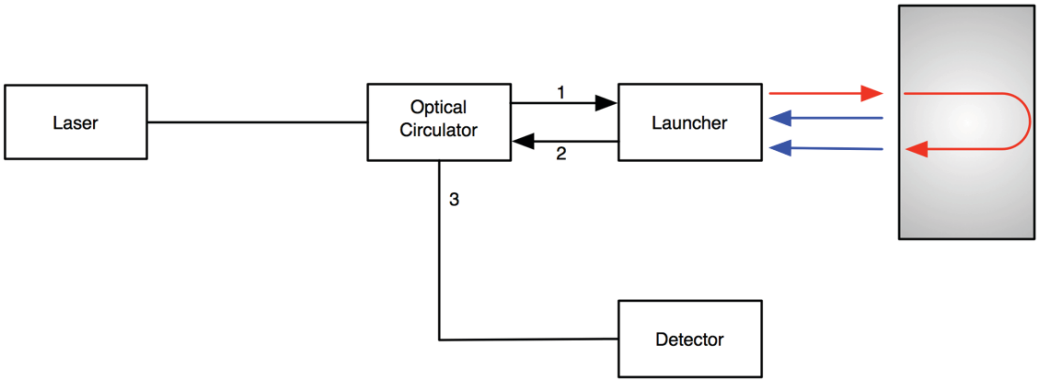

Figure 18 – Incoherent Detection Method.

Detection of multiple interfaces can also be understood by considering multiple reflections in a Fabry-Pérot etalon, also known as a Fabry-Pérot interferometer. This type of interferometer makes use of two partially reflective parallel surfaces. A portion of the light wave is transmitted each time it reaches the second boundary, resulting in multiple beams, which can interfere with each other [15]. The interference pattern produced by the multiple reflections of light becomes the subject of the analysis. Figure 19 provides a visual representation of the multiple reflections that the input beam undergoes as it traverses the etalon at an angle.

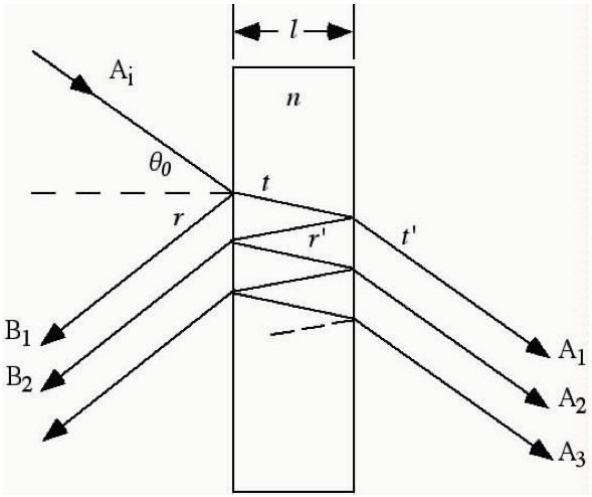

Figure 19 – Fabry-Pérot Etalon, from [46].

Through the use of a frequency swept source, the reflection spectrum of the etalon can be detected which will exhibit a periodic pattern with crests repeating at twice the optical path length of the etalon. The period of this signal can be related to the phase difference between successive reflected beams (B1 and B2 on Figure 19), and is given by [46]:

$$\Delta\varphi = \left(\frac{2\pi}{\lambda}\right) 2n\ell\cos\theta, \qquad (10)$$

where the phase relation will depend on the wavelength (λ) of the light source, the angle the light travels through the etalon (θ), the thickness of the etalon (ℓ), and the refractive index of the material between the reflecting surfaces (n).

This phase difference is essential in the signal analysis to determine the thickness of the sample. The amplitudes and relative phases of each of the reflected waves can be written as [46]:

$$B_1 = rA_i;\ B_2 = tt'r'e^{j\Delta\varphi}A_i;\ B_3 = tt'r'^3e^{j2\Delta\varphi}A_i, \cdots \qquad (11)$$

Utilizing the properties that $r = r'$, $R = |r|^2 = |r'|^2$ and $T = tt' = 1 - R$, the sum of the reflected waves can therefore be written as:

$$B_r = rA_i\left[1 - tt'e^{j\Delta\varphi}(1 + r'^2e^{j2\Delta\varphi} + \cdots)\right] = rA_i\frac{1 - e^{j2\Delta\varphi}}{1 - Re^{j2\Delta\varphi}}. \qquad (12)$$

The reflectance of the etalon, or reflection spectrum, can then be defined as:

$$R_{etalon} = \left|\frac{B_r}{A_i}\right|^2 = \frac{4\mathrm{R}\sin^2(\Delta\varphi/2)}{(1-\mathrm{R})^2 + 4\mathrm{R}\sin^2(\Delta\varphi/2)}. \quad (13)$$

The reflection spectrum for the incoherent detection of a 10cm etalon with a refractive index of 1.5 is shown in Figure 20. As seen on Figure 21, the autocorrelation, obtained by calculating the IFFT of the reflection spectrum, has a peak located at the ZPD and two peaks at the thickness of the sample. The peak at ZPD can be eliminated during signal analysis through calibration of the reflection spectrum signal, as will be performed for this thesis.

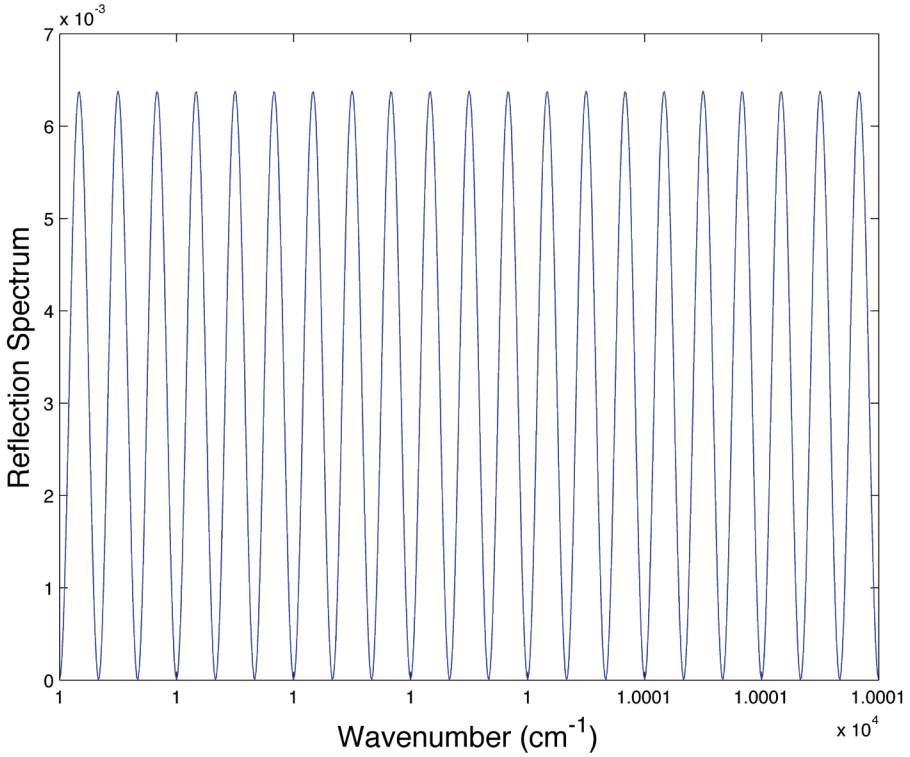

Figure 20 – Reflection Spectrum of a 10cm Fabry-Pérot Etalon Using the Incoherent Detection Method.

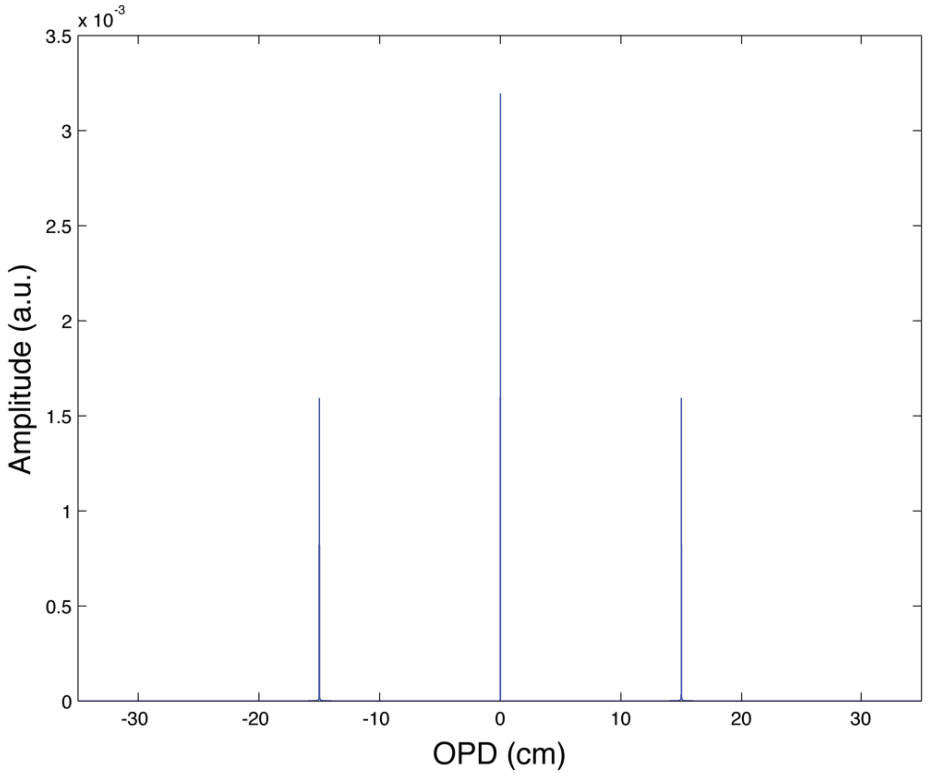

Figure 21 – Autocorrelation of a 10cm Fabry-Pérot Etalon Using the Incoherent Detection Method.[3]

Since multiple reflections within a Fabry-Pérot etalon are considered for this analysis, a peak will typically be present at each OPD of the etalon. As such, for the example of a 10cm etalon, peaks will also be present at OPDs of 30cm, 45cm and so on. They are not present on Figure 21, however, since their amplitudes are too small compared to the main peaks to be noticed. This is caused by the degradation of the signal amplitude following each additional reflection within the etalon. This concept of signal degradation is further explored in Section 3.5. The plotting of the autocorrelation on a logarithmic scale does enable the second and third harmonics of the sample thickness to be identified, as shown in Figure 22.

[3] The peak is located at 15cm due to the refractive index of 1.5.

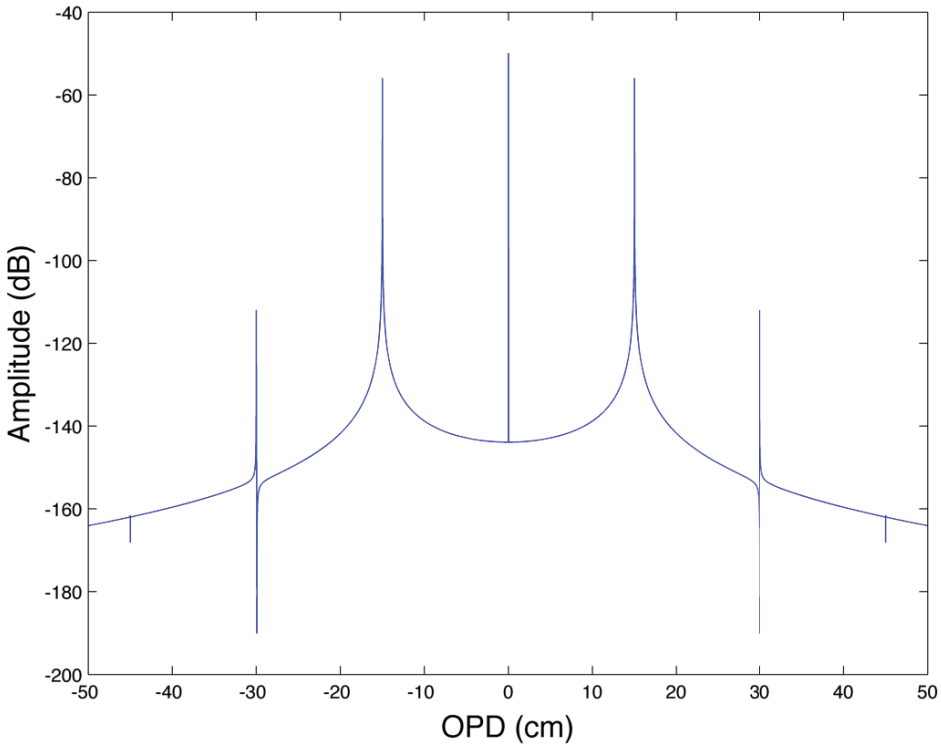

Figure 22 – Autocorrelation of a 10cm Fabry-Pérot Etalon Using the Incoherent Detection Method on a Logarithmic Scale.

3.1.3 Comparison of Coherent and Incoherent Detection Methods

The following paragraphs are mainly derived from a Université Laval report detailing the techniques that could be used to perform long distance reflectometry [3].

There are evidently advantages and disadvantages to both detection methods. In the coherent mode, the maximal delay for the interference of the fields in the two arms is directly related to the maximal distance that one wishes to scan. The laser must therefore remain coherent along the entire length of the measurement. As shown earlier, for a range of 1km, this implies a laser line width better than 300kHz, a rather severe limitation. By comparison, in the incoherent mode, the maximal delay between the fields is dictated by the maximal thickness of the sample under test since the laser only needs to be coherent within the sample. As such, for the desired measurement of a 10cm total optical thickness, the laser line width only needs to be better than 3GHz. This is an easily achievable line width since most laser diodes have line widths ranging from 1MHz to 10MHz [47].

One main advantage that the coherent detection method has in comparison to the incoherent case is that the geometric losses are 1/R rather than $1/R^2$, where R is the range between the instrument and the target. In the coherent detection method, the intensity term holding the interferometric information is the cross term multiplying the field of interest with the local oscillator field, which has not seen propagation losses. By comparison, the fact that the losses are 1/R on the field and sent to square law detector generate the $1/R^2$ losses for the incoherent detection method. The coherent detection method can thus provide orders of magnitude more signal at substantial distances.

In addition, due to the multiplication of the local oscillator with the field of interest, varying the strength of the local oscillator therefore provides gain on the signal; and this prior to photo detection. This coherent gain makes it easier to have a strong signal at detection and in practice one can increase the local oscillator power until the photo detector thermal noise is not the limiting noise source. The coherent detection method therefore reduces the difficulty in ensuring that the measurements are limited by the shot noise of the field of interest.

A final factor to consider for the detection method is the wave front quality upon detection. All surface irregularities will alter the reflected wave front and the modulation efficiency will be reduced when the non-identical wave fronts are recombined. In practice, surface irregularities produce speckle patterns and coherent detection can't average on beam sizes larger than a few speckles before the signal is lost. By comparison, an incoherent system can collect light in large throughputs, as each point on the detector can be considered independent in terms of its intensity.

The main factors enabling the comparison between the coherent and incoherent detection methods are outlined in Table 1.

Table 1 – Comparison of Coherent and Incoherent Detection Methods.

Factor	**Coherent**	**Incoherent**
Geometrical Losses	1/R	$1/R^2$
Coherent Gain	Yes (shot noise attainable)	No (detector noise limited)
Speckle Averaging / Wave Front Quality	Only a few speckles / Sensitive	Arbitrary Throughput / Not Sensitive
Measurement	Sample impulse response (absolute distance)	Sample auto-correlation (relative distance / thickness)
Laser Line Width	< 1MHz	< 1GHz

As will be seen in Chapter 4, the experimental setup adopted for this thesis is considered incoherent. While less information is acquired in an incoherent setup, the complexity of the measurement is reduced considerably since there is no necessity for the field coming from the scene to be perfectly superimposed to the local oscillator field for the interference to be optimal.

3.1.4 Spatial Resolution

Another characteristic of importance for this thesis is the spatial resolution. As per the Fourier transform relation, the time resolution is proportional to the inverse of the frequency span. The spatial resolution can therefore be defined as:

$$\Delta R = \frac{1}{\Delta f}. \qquad (14)$$

Converting this equation to wavelengths yields:

$$\Delta R = \frac{\lambda_0^2}{2\Delta\lambda_{max}}, \qquad (15)$$

where $\Delta\lambda_{max}$ is the tuning range of the laser.

As such, the goal of employing the tunable laser is to achieve a rapidly tuned laser over a broad range [3]. These concepts were supported by experiments conducted by Dieckmann and Amann [29] (as discussed above in Chapter 2) as well as by Burrows and Liou [48], with both being able to achieve high-resolution measurements.

To achieve a 0.5mm resolution, this implies that a laser operating at 1550nm require a tuning range of 2.40nm [33]. A 2nm tuning range was therefore the goal when performing the setup of the laser diode, leading to a resolution of 0.6mm.

3.2 Reference Interferometer

The reference interferometer is the key that allows the precise calculation of the thickness of the measured sample. The reference arm interferometer can be used to properly calibrate the laser's wavelength sweep, which is never perfectly linear in practice. The reference interferometer utilizes the principles of a Michelson interferometer where the signal emanating from the laser is divided into two arms, with one arm having a known delay with respect to the other. A simple bloc diagram of the reference interferometer is shown in Figure 23.

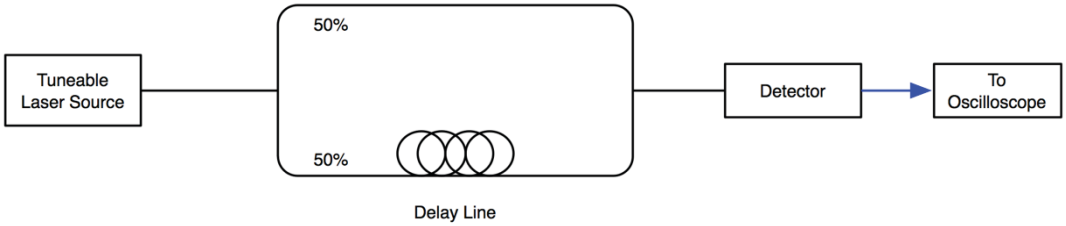

Figure 23 – Reference Interferometer Bloc Diagram.

Figure 24 provides a graphical representation of a triangular frequency modulation of a cosine signal. The signal detected at the output of the reference interferometer will resemble the frequency-modulated signal from the figure below, where the laser's wavelength is swept on a linear scale, but with a much faster sinusoid and hence a larger number of cycles. By extracting the instantaneous phase of the interference signal generated from the recombination of both arms of the reference interferometer, the laser's wavelength sweep can be properly calibrated through interpolation. With the knowledge the length of the delay line, it can then be used as a comparative tool in order to extract the thickness of the layer(s) of the multilayer sample.

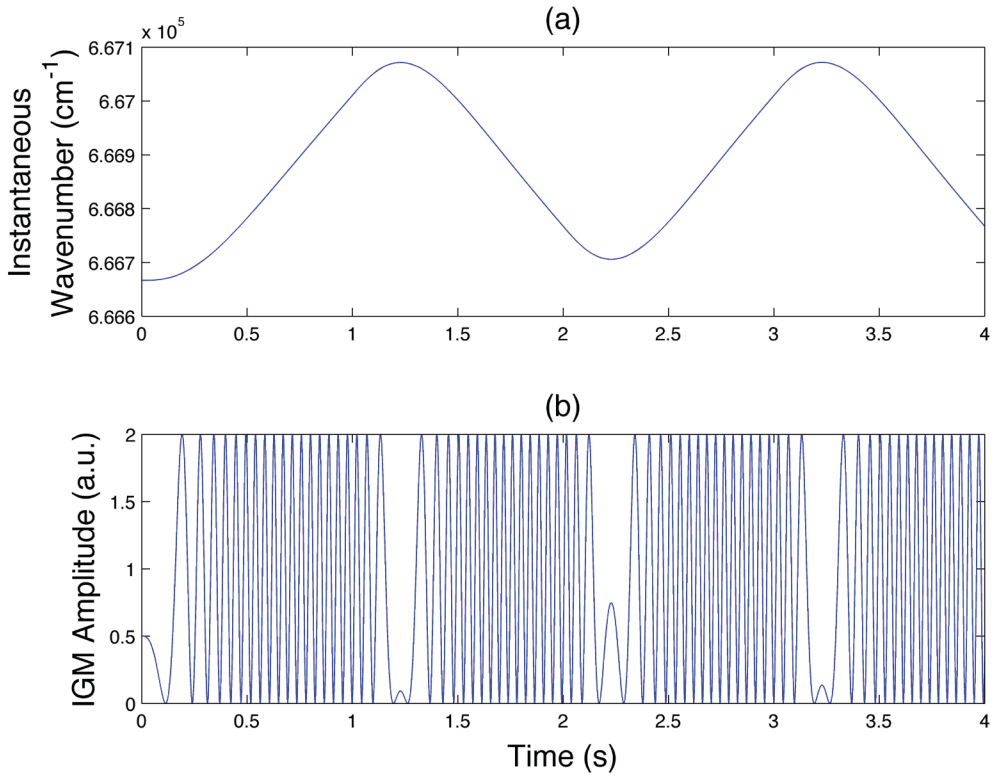

Figure 24 – (a) Frequency Evolution of Signal and (b) Frequency-Modulated Signal.

The interference pattern measured at the output of the reference interferometer is the one from a two-beam interferometer with a fixed delay Δx and a variable wavenumber σ [49]:

$$1 + \cos(2\pi\sigma\Delta x). \qquad (16)$$

When the wavenumber sweep of the laser is linear, a cosine interferogram is measured. Any deviation from a linear sweep will be perceived as a phase fluctuation on the reference interferogram. From Eq. (16), one can see that one cycle of the reference interferogram corresponds to a wavenumber evolution of $\sigma = 1/\Delta x$. Performing a phase extraction on the reference interferogram and tracking the phase evolution therefore allows to precisely follow the evolution of the frequency sweep of the tunable laser. This will allow the complex frequency response of the sample on a known frequency grid to be obtained. One can also see that this instrument is actually comparing the unknown thickness of the samples to the length of the reference interferometer, and is doing so across the tunable laser.

3.3 Fourier Transform

Since the frequency swept interferometer is measuring the spectral response of the sample frequency by frequency, the inverse Fourier transform of the measured signal needs to be computed in order to obtain either the impulse response or the autocorrelation of the sample.

Fundamentally, the Fourier transform enables the function's spatial or temporal domain to be related to its frequency domain. In this work, the inverse Fourier transform will be applied to relate the spectral wavenumbers ($\sigma = f/c$) to the spatial optical delay domain (Δx). The wavenumber is usually expressed in cm^{-1} since the delays of interests are often in cm.

The Fourier and inverse Fourier transforms of a particular function can be defined as [49]:

$$F(\sigma) = \int_{-\infty}^{+\infty} f(x) e^{-2\pi j \sigma x}\, dx, \qquad (17)$$

$$f(x) = \int_{-\infty}^{+\infty} F(\sigma) e^{2\pi j \sigma x}\, d\sigma. \qquad (18)$$

This definition can be applied to a cosine signal to mathematically obtain its inverse Fourier transform:

$$\mathcal{F}_{\sigma}^{-1}[\cos(2\pi\sigma x_0)](x) = \int_{-\infty}^{+\infty} e^{2\pi j \sigma x} \left(\frac{e^{2\pi j \sigma x_0} + e^{-2\pi j \sigma x_0}}{2} \right) d\sigma, \qquad (19)$$

$$\mathcal{F}_{\sigma}^{-1}[\cos(2\pi\sigma x_0)](x) = \frac{1}{2} \int_{-\infty}^{+\infty} \left[e^{2\pi j \sigma (x - x_0)} + e^{2\pi j \sigma (x + x_0)} \right] d\sigma, \qquad (20)$$

$$\mathcal{F}_{\sigma}^{-1}[\cos(2\pi\sigma x_0)](x) = \frac{1}{2} [\delta(x - x_0) + \delta(x + x_0)], \qquad (21)$$

where δ(x) is defined as the Dirac's delta function. Figure 25 provides a few graphical examples of signals with single and multiple cosine components. As can be seen, the inverse Fourier transform of these respective signals returns a spatially localized peak for each of the component OPDs.

In practice, the discrete Fourier transform is used on the acquired data to retrieve the impulse responses or their autocorrelations.

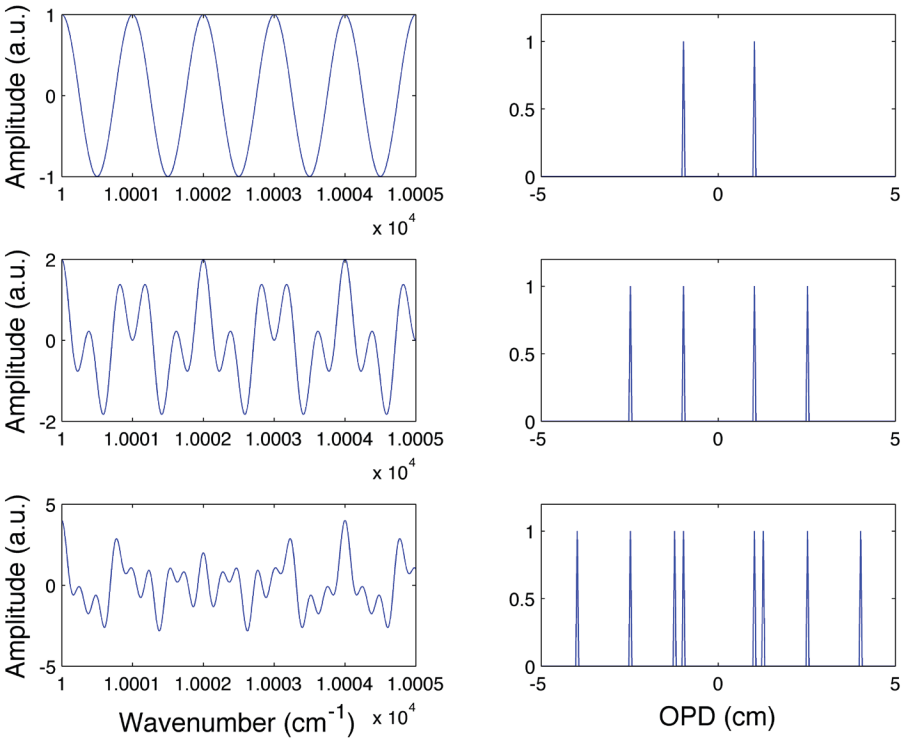

Figure 25 – A Cosine Signal with its Associated FFT for Simulated Thicknesses of (a) 1cm (b) 1cm & 2.5cm (c) 1cm, 1.25cm, 2.5cm & 4cm.

3.4 Signal Analysis

To precisely track the frequency evolution of the tunable laser, a reference interferometer having a known delay is used, as previously demonstrated in Section 3.2. As the tunable laser sweeps in frequency, the reference signal generates a cosine whose phase evolution provides information on the frequency evolution as a function of time. The instantaneous phase of the reference signal is thus first extracted. The use of an optical hybrid allows the detection of both the reference signal (0^o) and an offset version of the reference signal ($+90^o$). Applying MATLAB's four-quadrant inverse tangent (atan2) between the reference signal and its offset enables the extraction of the instantaneous phase of the reference signal.

By applying the concept that constructive interference is obtained when two waves are in phase and at multiples of 2π, and the fact that the phase between the two arms of the reference interferometer can be written as:

$$\Delta\varphi = 2\pi\Delta\sigma n\ell = 2\pi, \quad (22)$$

$$\Delta\sigma = \frac{1}{n\ell}, \quad (23)$$

a time vector is interpolated for every multiple of 2π of the unwrapped instantaneous phase of the reference signal, which allows the extraction of the points where the wavenumber increment is an integer of the length of the delay line (ℓ) multiplied by the refractive index of the fibre optic cable (n), as seen in Eq. (23). This same time vector can be used to interpolate the sample signal, allowing the sample signal to be resampled on an equidistant grid of known wavenumber increments. Figure 26 provides a graphical representation of a cosine signal and its associated wrapped and unwrapped instantaneous phase. It can be observed on Figure 26 that each point of 2π on subplot (c) corresponds to a maximum (or crest) on subplot (a).

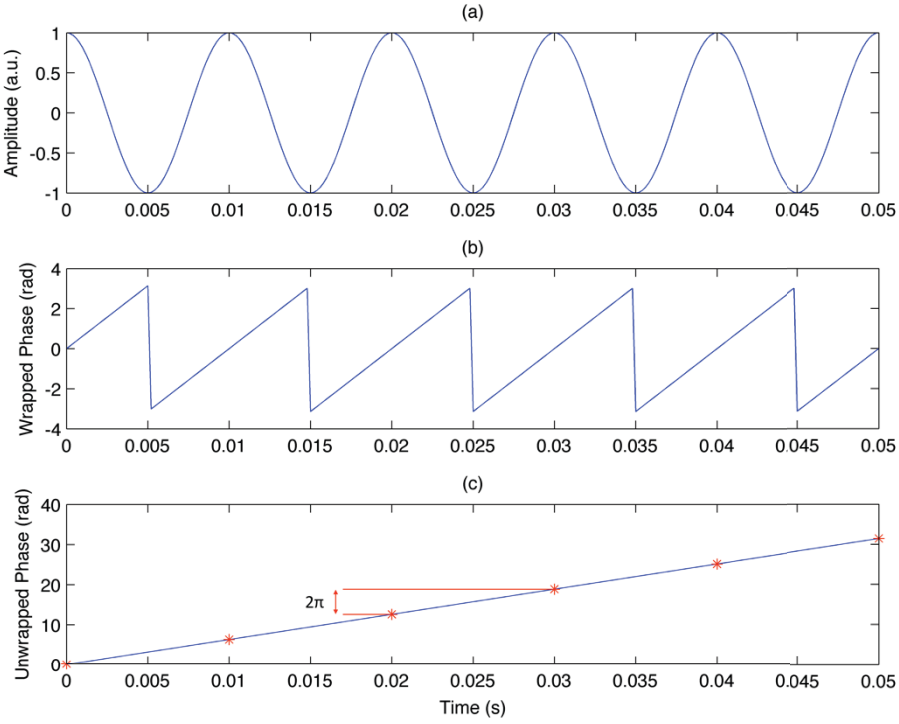

Figure 26 – (a) Reference Signal (b) Wrapped Phase (c) Unwrapped Phase with 2π Interpolation.

Now that the sample signal wavenumber scale has been properly calibrated, the inverse Fourier transform can be applied on the interpolated sample signal to determine the individual thicknesses, since each peak will be associated to a sample's OPD.

Using the result from Eq. (23) and the properties from the Fourier transform [19], the OPD axis is calculated as:

$$\Delta X_{max} = \frac{1}{\Delta\sigma} = n_{fibreoptic}\ell_{delayline}. \quad (24)$$

In order to retrieve the physical thickness of the multilayer sample, the phase relation from a Fabry-Pérot etalon in Eq. (10), as well as the result from Eq. (24), are used to determine the following relationship:

$$2\pi = (2\pi\Delta\sigma)2n_{material}\ell_{material}cos\theta, \quad (25)$$

$$n_{fibreoptic}\ell_{delayline} = 2n_{material}\ell_{material}cos\theta, \quad (26)$$

$$\ell_{material}cos\theta = \frac{n_{fibreoptic}\ell_{delayline}}{2n_{material}}. \quad (27)$$

After performing the inverse Fourier transform, each peak position will equal $2n_{material}\ell_{material}cos\theta$ on the OPD axis, provided that $n_{fibreoptic}$ is properly taken into account in the calibration. As will be seen, this is done automatically by the manner used to characterize $n_{fibreoptic}\ell_{delayline}$. For this thesis, it was chosen to divide the OPD axis by two prior to plotting the single sided inverse Fourier transform. This decision was based on having figures that are representative to having this setup perform measurements in the field where the characteristics of the sample are unknown. The effective optical thickness of an individual layer can subsequently be defined as:

$$\zeta = n_{material}\ell_{material}cos\theta. \quad (28)$$

3.5 Stratified Medium Interference

The multilayer samples, or stratified medium, can be regarded as the combination of multiple Fabry-Pérot etalons. Each individual layer, as well as the combination of any two interfaces, will contribute towards the detected reflection and/or transmission spectrum. As such, calculating the inverse Fourier transform of the amplitude spectrum will generate an interferogram with peaks located at the OPDs of the etalon, as well as combinations and harmonics of the OPDs.

The following paragraphs are mainly derived from an ABB/Université Laval report describing the development of a stratified medium prediction algorithm [50].

The detection of the stratified medium is based on parasitic reflections at the interfaces. Assuming the material is glass, the parasitic reflection will be around 4% in intensity, for air/material interfaces. To measure the sample thickness, at least two parasitic reflections are needed (see calculations in next section). Of course, multipath interference is possible, as light can do several round-trips in the etalon. These beams will however need additional parasitic reflections and the corresponding signals will thus be at least an order of magnitude lower.

In a multilayer sample, the parasitic reflections can occur at any two interfaces. For example, a two-layer medium will generate three peaks, one for each individual layer and one for the sum of the two layers. A three-layer medium will produce six dominant peaks. Figure 27 provides a visual representation of a three-layer medium with the additional combinations. In the general case, a N-layer stratified medium will produce:

$$N_{2RX} = \frac{(N+1)!}{2!\,(N-1)!} = \frac{N(N+1)}{2} \qquad (29)$$

peaks on the single-side autocorrelation (considering only positive OPDs, as the autocorrelation is symmetrical).

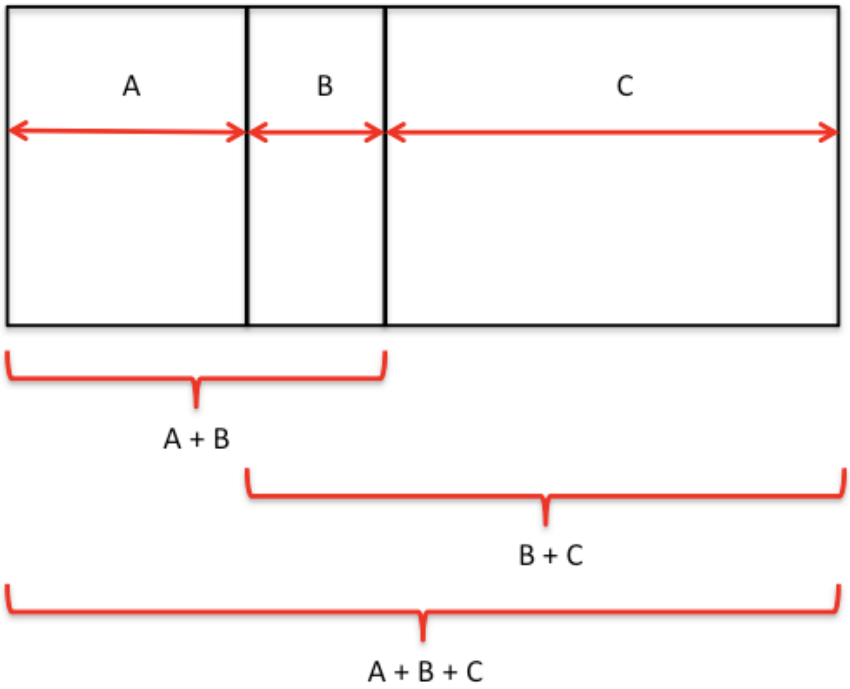

Figure 27 – Three-Layer Medium with Combinations.

It is evident that some cases might lead to non-unique solutions, such as thin layers having unresolved peaks (due to limited spectral range) or layers, layer harmonics and layer combinations having similar thicknesses. This is an important element that will need to be taken into consideration during the data analysis process. A lack of contrast between the refractive index of two adjacent layers might also limit the number of layers that can be identified.

In addition to the number of peaks expected per the number of layers, additional information can be taken into account for the peak positions with respect to the OPD locations on the interferogram. Firstly, the peak located at the smallest OPD is associated to the effective thickness of the thinnest resolved layer of the stratified medium. If multiple peaks are observed, the peak located at the second smallest OPD will be associated to the second smallest effective thickness of the second thinnest layer, and so forth. Additionally, the major peak located at the largest OPD will be associated to the total effective thickness of the medium and should, in theory, have the one of the largest magnitudes due to the large change of refractive index between the medium and the air.

3.6 Measurements in Reflection versus in Transmission

As with any field experiment, achieving perfect testing conditions are extremely difficult. It is evident that the ideal solution for the measurement of a multilayer sample is a perfect perpendicular alignment, where the angle of incidence between the probing beam and the sample is 0^{o}, thus achieving the detection of specular reflection. This, however, is particularly difficult to achieve, as a minute shift in the alignment will alter the angle of incidence, having great impact at large detection distances. Since the samples are more often than not going to be detected at an angle with respect to the probing beam, the question remains if the measurements are better to be performed in reflection or in transmission, assuming a lambertian reflector is located behind them. The difference between the specular and diffuse reflection of incident light is demonstrated in Figure 28.

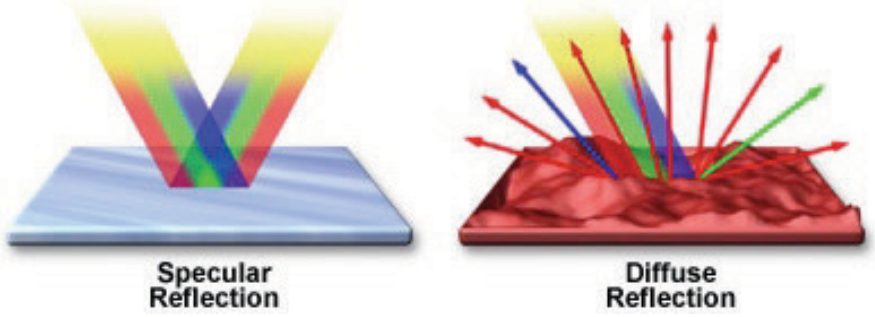

Figure 28 – Specular vs. Diffuse Reflection, from [51].

The following paragraphs are mainly derived from a Université Laval report detailing the various techniques that could be used to perform long distance reflectometry [3]. The calculations have been modified to take into account the error in the report with regards to the need to consider the product of the square root of the power of the fields that interfere.

If we assume standard tempered glass with a refractive index of 1.5, we can expect the parasitic reflectance between the air and glass interface to be approximately 4%. Since the glass samples are typically polished to a high quality, this means that the majority of the parasitic reflection is specular (red lines on Figure 29), which leaves only a small fraction of diffuse light (D_r) to be reflected (blue lines on Figure 29), of which only a fraction (C_r) is captured by the telescope's field-of-view (FOV). The remaining light will traverse the sample and continue propagating away from the instrument. The fraction of reflected light, in intensity, detected for the first interface can be written as:

$$F_{r1} = 0.04 \times D_r \times C_r \,, \qquad (30)$$

while the fraction detected for the second interface, after traversing through the sample and being reflected, can be expressed as:

$$F_{r2} = (1 - 0.04)^2 \times 0.04 \times D_r \times C_r \,. \qquad (31)$$

The interference detected for the probing of a glass sample in reflection can be considered as:

$$F_{RX} = \sqrt{F_{r1}} \times \sqrt{F_{r2}} = (1 - 0.04) \times 0.04 \times D_r \times C_r \,. \qquad (32)$$

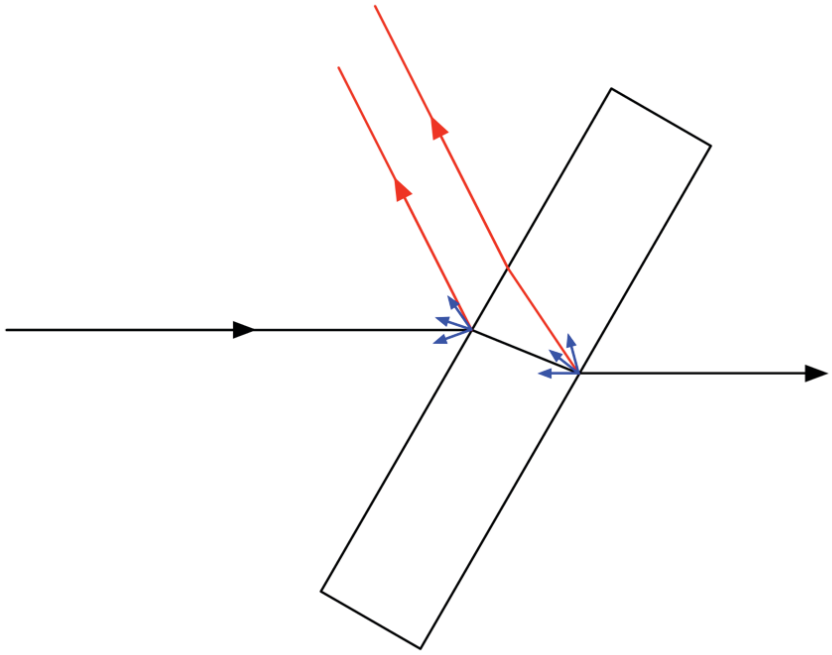

Figure 29 – Probing of a Sample in Reflection, from [3].

In the actual field measurements of a sample at long range, it is not uncommon to have another target situated behind the sample under test. This target is considered to likely be a diffuse reflector, such as a painted wall. Since these surfaces are not polished, they will return the light via diffuse reflection, as shown on Figure 30. This means that the diffuse reflection coefficient of the reflector (D_t) is expected to be much greater than its specular reflection coefficient, while the FOV coefficient will be roughly equal in reflection and transmission (C_r and C_t). In transmission measurements, we must rely on two successive parasitic reflections (specular light in this case) to achieve the detection of the

sample. The fraction of transmitted light detected for the two interfering paths following their reflection off the diffuse reflector and back through the sample are defined as:

$$F_{t1} = (1 - 0.04)^4 \times D_t \times C_t \,, \qquad (33)$$

$$F_{t2} = (1 - 0.04)^4 \times [0.04 \times (1 - D_r)]^2 \times D_t \times C_t \,. \qquad (34)$$

The interference detected from a transmission measurement can thus be expressed as:

$$F_{TX} = \sqrt{F_{t1}} \times \sqrt{F_{t2}} = (1 - 0.04)^4 \times [0.04 \times (1 - D_r)] \times D_t \times C_t \,. \qquad (35)$$

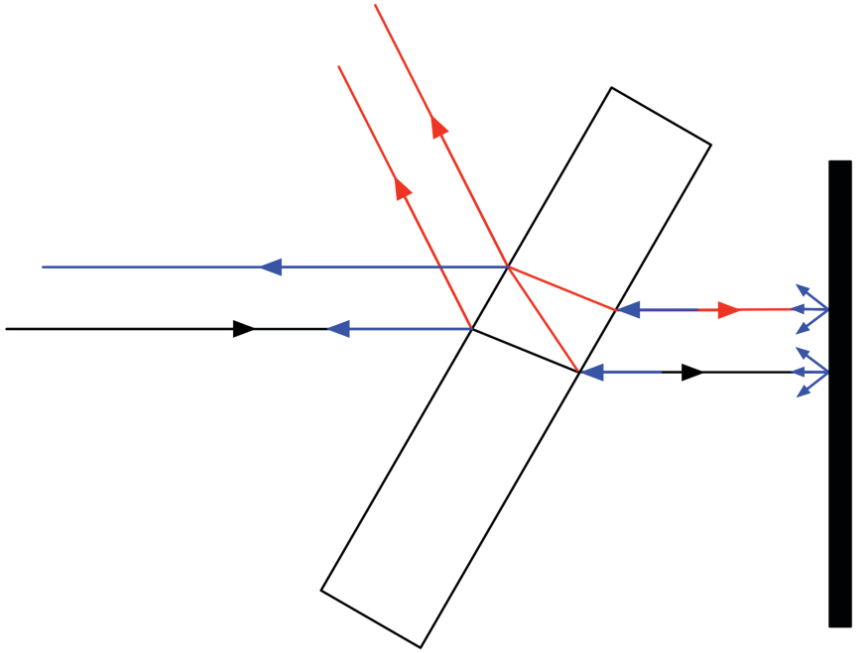

Figure 30 – Probing of a Sample in Transmission with Diffuse Reflector, from [3].

Comparing Eq. (32) with Eq. (35), it is determined that for F_{TX} to be greater than F_{RX}:

$$(1 - 0.04)^4 \times 0.04 \times (1 - D_r) \times D_t \times C_t > (1 - 0.04) \times 0.04 \times D_r \times C_r \,, \qquad (36)$$

$$(1 - 0.04)^3 \times D_t > \frac{D_r}{(1 - D_r)} \,. \qquad (37)$$

Since D_r is significantly smaller than 1, the right hand term is effectively equal to D_r. The above equation can be simplified to:

$$D_t > 1.13\, D_r\ . \qquad (38)$$

Equation (38) implies that as long as diffuse reflection of the reflector behind the sample is 1.13 times greater than the diffuse reflection at the air/glass interface, it will be more feasible to gather the information from the transmission in the sample rather than from the reflection of each individual interface.

As it will be seen in the next chapter detailing the experimental setup, a spectralon block (approximately 99% diffuse reflectance) is placed behind the sample to act as a diffuse reflector[4], enabling the detection of the transmission spectrum of the sample.

3.7 Off Axis Effect

One important factor to take into consideration in the experiments while performing the measurements is the angle of incidence of the incoming beam in relation to the sample. This is important since the light beam, after having traversed through the sample, will enter the collection instrument with a shear [16]. The shear observed will only be present during the measurements performed in transmission since, for the case of detecting in reflection, the light returned via diffuse reflection will return towards the instruments along its incoming path (see Figures 28 and 29). Using Snell-Descartes law, the refracted angle is calculated as [49]:

$$n_1 sin\theta_1 = n_2 sin\theta_2, \qquad (39)$$

$$\theta_2 = sin^{-1}\left(\frac{n_1 sin\theta_1}{n_2}\right). \qquad (40)$$

With the aid of Figure 31, the shear observed can be calculated to be:

$$\Delta Y = e * tan\theta_2, \qquad (41)$$

$$\Delta Y = e * tan\left(sin^{-1}\left(\frac{n_1 sin\theta_1}{n_2}\right)\right). \qquad (42)$$

[4] A piece of paper can also be used to replace the spectralon block, achieving near identical results.

When it is considered that the beam of light will travel through the sample twice when observed through the telescope, the shear detected can be defined as [3]:

$$\Delta Y = 2e * tan\left(sin^{-1}\left(\frac{n_1 sin\theta_1}{n_2}\right)\right). \quad (43)$$

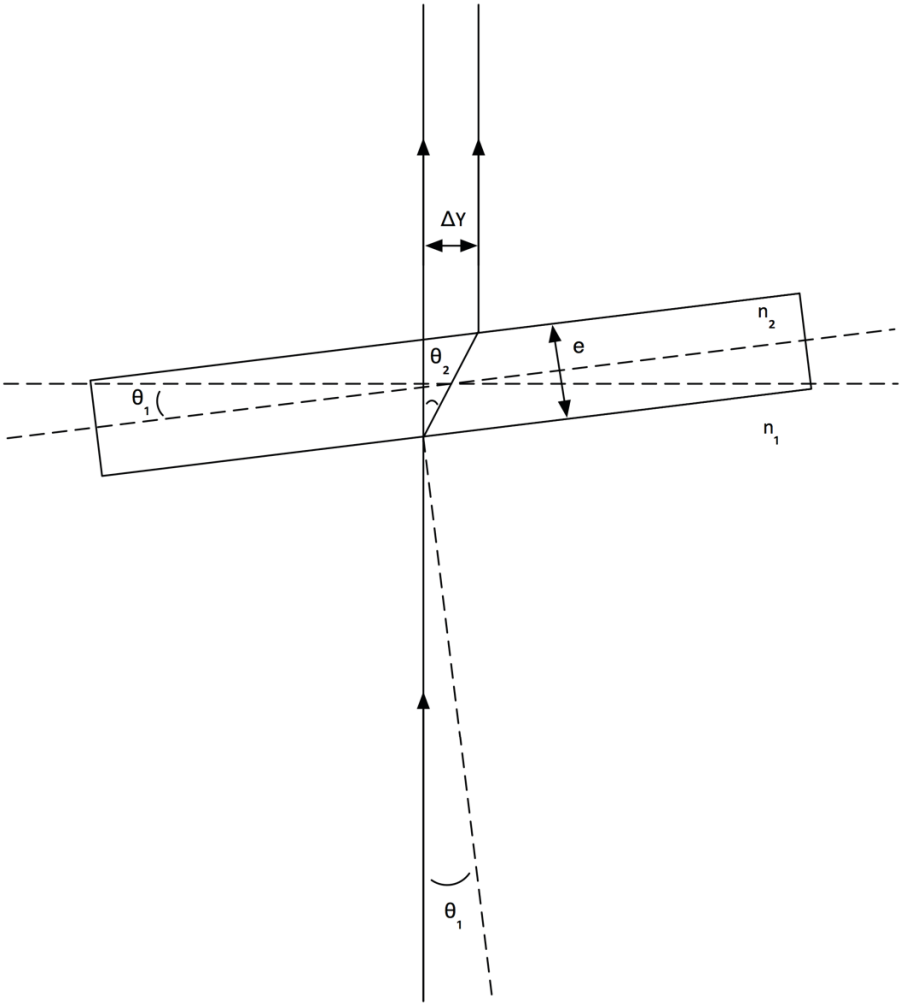

Figure 31 – Shear Due to Off Axis Effect.

Similar to a misaligned interferometer, this shear combined with the divergence of the incoming beam will lead to a loss of the modulation efficiency of the interference [50], which can be defined as [16]:

$$Mod.Eff.= 2\frac{J_1(2\pi\sigma\Delta Y\theta_m)}{(2\pi\sigma\Delta Y\theta_m)}, \quad (44)$$

where J_1 is the first order Bessel function, σ is the wavenumber of the light and θ_m is the maximum divergence half-angle of the beam. The function $2J_1(x)/x$, plotted in Figure 32, is often labeled as the "jinc" function. Considering that it is desired to maintain a modulation efficiency loss higher than 60% for the purpose of these experiments, the argument of the Bessel function must be kept smaller than two.

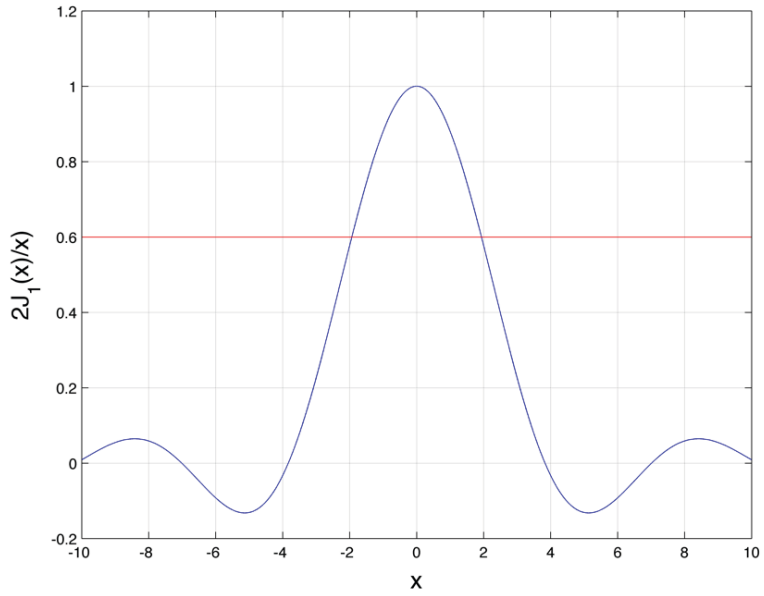

Figure 32 – Jinc Plot with 60% Modulation Efficiency Cut Off.

For example, if a 10cm thick glass window is being measured with a laser operating at a wavelength of 1550nm and it is desired to perform measurements up to 30° angle of incidence; the maximal half-beam divergence will be limited to 6.98μrad. This will be an important factor to consider for the LADAR head geometry of the experiments as well as the limitations imposed on the angle of incidence.

This off-axis effect puts some counterweight to the previously stated fact that, in theory, the total thickness should produce the largest peak because of the large refractive

index contrast. This shear effect when probing in transmission will reduce the amplitude of the peak detected for thicker layer combinations.

3.8 Refractive Index for Stratified Medium

One is able to observe, through Eq. (28) above, that the refractive index of the material is an important factor in the measurement of the thickness of the multilayer sample. Since different sample materials were chosen to perform the measurements, knowing the refractive index for the wavelength of the experimental setup is essential in order to precisely determine the thickness of the individual layers. For the cases where different materials are stacked together to create the multilayer sample, the average refractive index must be considered when calculating the thickness of these combined layers.

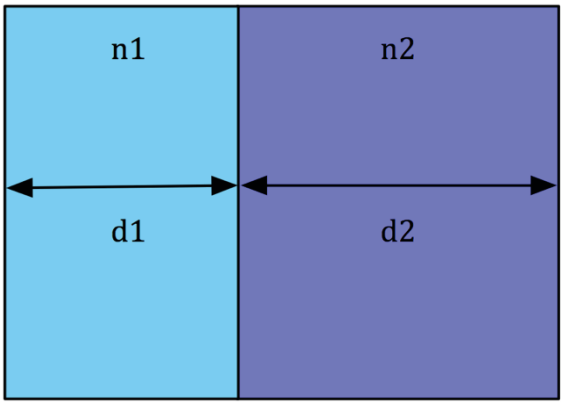

Figure 33 – Two-Layer Stratified Medium.

Looking at a two-layer sample with refractive indexes of n_1 and n_2 and thickness d_1 and d_2 respectively, shown in Figure 33, the average refractive index will be [49]:

$$\bar{n} = \frac{n_1 d_1 + n_2 d_2}{d_1 + d_2}. \quad (45)$$

This equation essentially calculates the contribution of each layer's refractive index with regards to the overall thickness of that layer combination. This equation can also be used to calculate the average refractive index for the layer combination of three and four layers, adding $n_x d_x$ to the numerator and d_x to the denominator.

3.9 Theoretical Concepts – Concluding Remarks

In summary, several theoretical concepts were presented in this chapter that all contributed to the detection of the thickness of the individual layers of a multilayer sample. The consideration of the stratified medium, or multilayer sample, as several Fabry-Pérot etalons stacked together allowed the thickness of the individual layers to be retrieved. In this work, this was achieved by the use of a rapidly sweeping tunable laser diode and extracting the instantaneous phase of a reference interferometer to decompose the signal generated from the interference of the sample's layers. The inverse Fourier transform of the detected transmission spectrum allowed the peaks located at the OPDs of the etalon to be retrieved. As will be seen in the following chapter, these theoretical concepts were all considered for the experimental setup and programme.

4 Experimental Concept and Setup

The purpose of this chapter is to explain the experimental methodology developed for this thesis, and to outline in detail the experimental setup used to perform the measurements in the indoor and outdoor conditions. The following sections will provide an overview of the general experimental concept, together with details about specific components of the experimental setup, including: the tunable laser diode setup, the delay line calibration, the optical hybrid, the beam launching, and the telescope and detection subsystem. A discussion of the LADAR head and its effect on the limitations of the angle of incidence are also included. Finally, a description of the outdoors experimental programme will be provided.

4.1 Experimental Concept

The experimentation process was conducted in two phases: an indoor laboratory phase and the outdoor measurement campaign. The goals of the indoor laboratory phase were to select a tunable laser source, design and calibrate the reference arm of the interferometer setup as well as take measurements of single and multilayer samples for the development of the MATLAB code used for signal processing. In addition, these indoor measurements would serve as an initial proof of concept that the thickness of individual layers as well as total thickness of multilayer samples could indeed be retrieved using the selected laser diode.

Once the results of the indoor measurements were successful and proved the detection of the individual layers of multilayer samples, the main testing phase was conducted outdoors on the Université Laval campus. The laboratory setup was moved to the third floor remote detection laboratory in the COPL and was connected to the telescope and launcher setup assembly, which was already optimized for outdoor measurements from previous experiments [3].

All the stratified medium samples, with the exception of the three industrially manufactured samples, were assembled in house at Université Laval. Four acrylic samples and one BK7 sample were cut and sized to fit in the sample mount assembly. The sample thicknesses were chosen so that their harmonics would not overlap which would complicate the layer identification process for this first demonstration. To build multilayer samples, the various samples would simply be stacked together within the

mounting assembly, using latex gloves and cleaning the samples with compressed air to avoid as much contamination as possible. The next sections will detail the steps taken during the indoor laboratory phase to detect these samples.

4.2 Tunable Laser Source Setup

The first step in designing the experimental setup was to select a tunable laser source. Many factors contributed to the decision to use a laser diode as a source, including their low cost and the availability of such products in the laboratory inventory. There also existed large quantity of laser diodes in stock with identical central wavelengths, which meant that backups existed if ever one of the diodes ended up being damaged through the experimentation process. In addition, if ever it was desired in the future to field deploy this experimental setup, laser diodes would be the ideal choice due to their small, compact and rugged nature. The laser diodes are also capable of having their performance characteristics optimized for specific applications, including power, modulation speed, spectral line width and operating wavelength [52].

While a laser diode is not a tunable laser by definition, one is still able to modify its wavelength by varying the diode's temperature or current. Since a 2nm sweep was the objective to achieve the desired resolution of 0.6mm, a standard laser diode was deemed sufficient as the laser source for this thesis. In addition, the laser diode could also be used for this application due to the relaxed constraints on the laser's line width required in this incoherent approach. Moreover, since the laser only needs remain coherent within the sample itself, a standard OCT laser source could also be adopted for a field instrument of this application. This arises from the fact that there are no stringent requirements on the laser's line width. There are therefore a large variety of commercially available lasers that could be used for such a field instrument.

The Hewlett-Packard (HP) LSC2641 DFB laser diode, which was adopted for this experiment, has a central wavelength of 1562.0nm and can be controlled either by modulating its temperature or its current. Tests in the laboratory were performed using both methods to determine which was more precise and could generate the largest bandwidth sweep in terms of its wavelength. Figures 33 and 34 provide a graphical representation of data acquired from the optical spectrum analyzer for both modulation methods. These standalone tests were performed by manually varying the temperature and/or the current while the laser source was connected to the spectrum analyzer.

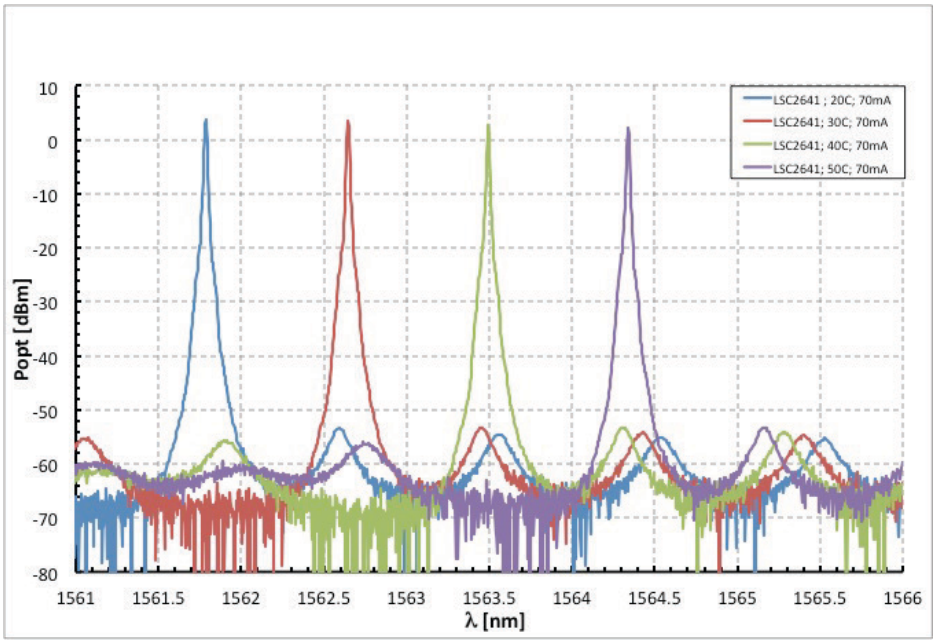

Figure 34 – Wavelength of HP LSC2641 with Temperature Variations.

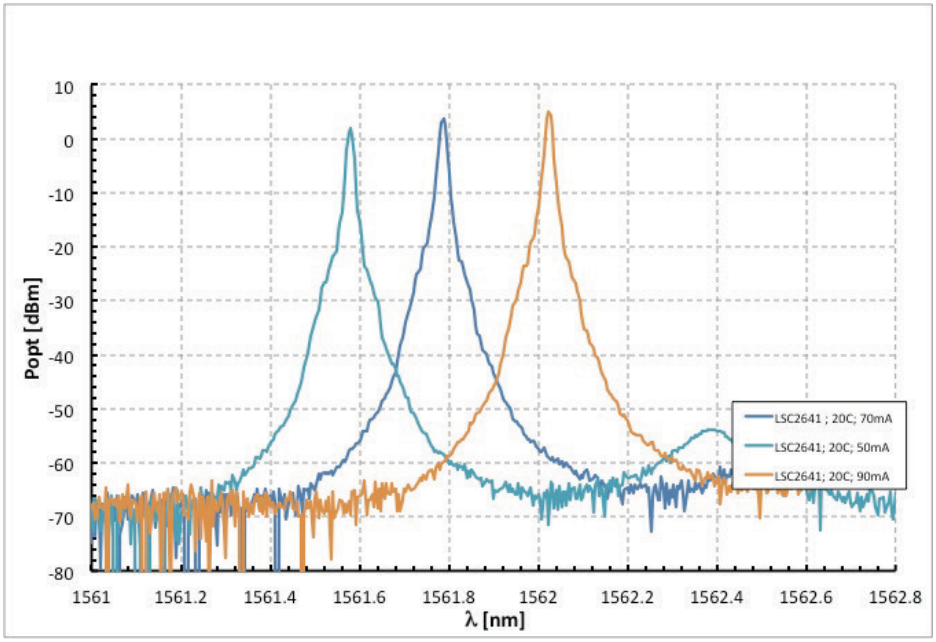

Figure 35 – Wavelength of HP LSC2641 with Current Variations.

The tests clearly demonstrated that varying the laser diode's wavelength by modulating its temperature generated a larger sweep, which meant a better spatial resolution. The laser diode was then connected to an ILX Lightwave Modular Laser Diode Controller in order to track the diode's temperature and current variations. A method was

developed to create a continually sweeping laser source through temperature modulation. To achieve this continuous sweep, a simple circuit setup was designed.

As seen in Figure 36, an 8kΩ resistor, placed in parallel with an ON/OFF switch, is connector in series with the laser's thermistor. A function generator producing a square wave at the start of the circuit allows the switch to toggle between being open or closed. The control circuit, which is connected to the ILX Lightwave controller, essentially "fools" the controller into believing the laser diode is a specific temperature. The controller is always attempting to maintain total resistance of 12kΩ, thereby modifying the value of the laser's thermistor to accomplish this control.

Two stages must be considered to properly understand how the control circuit functions to enable the laser's wavelength to sweep. The first stage (represented by 'a' on the square wave plot of Figure 36) is considered when the function generator's input is 0V, which means the switch is closed. The ILX controller calibrates the laser's thermistor, Rth_laser, to the 12kΩ control value, equivalent to a 20^{o}C temperature setting. The second stage (represented by 'b' on the square wave plot of Figure 36) is considered when there is a 5V input by the function generator, which causes the switch to open. At the initial instant of stage 'b', the total resistance seen by the controller is 20kΩ, the sum of 8kΩ and thermistor's present value of 12kΩ. This is equivalent to a 10^{o}C temperature setting. Since the controller is constantly attempting to calibrate to the 20^{o}C setting, but believes the laser has a temperature of 10^{o}C, it must heat the laser to achieve its desired setting. The laser's thermistor must therefore be adjusted to obtain the desired total resistance of 12kΩ. The thermistor is subsequently modified to a value of 4kΩ; the difference between the desired total resistance of 12kΩ and the 8kΩ already present in the circuit. The 4kΩ resistance implies that the controller heats the laser to a temperature setting of 47^{o}C during the stable section of stage 'b'. This simple circuit design thus allows the continuous sweep of the laser diode's wavelength.

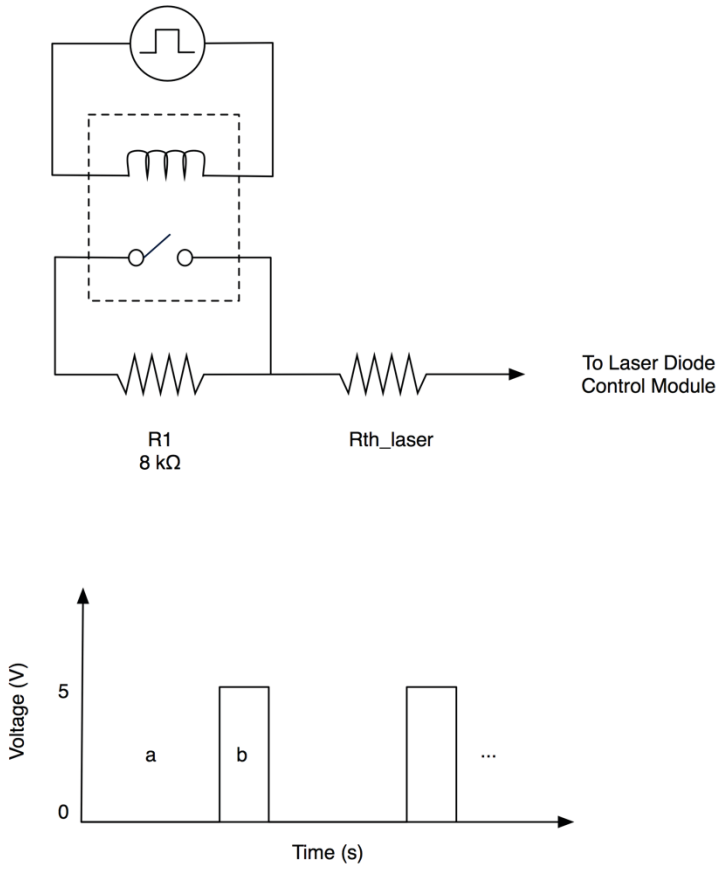

Figure 36 – Laser Diode Control Circuit Diagram.

For the experimental setup of this project using the HP LSC2641 DFB laser diode, the settings for the function generator are in Table 2. They allowed a sweep covering a wavelength bandwidth of approximately 2nm, achieving the tuning range objective established in Chapter 3. Using Eq. (15), it was determined that the 2nm tuning range allowed a spatial resolution of 0.609mm to be achieved. The square wave also served as a trigger for the oscilloscope during the detection process. This meant that the frequency of the square wave determined the duration of one acquisition cycle, i.e. 5.71s for the complete sweep of the laser's wavelength.

In addition, the thermoelectric cooler (TEC) was seen to be constantly at its limit, all the while remaining within safe operation. This meant that the laser diode was continually being pushed to its maximum, and a larger or faster sweep could not be achieved. The life cycle of the laser diode must be taken into account since these types of laser diodes are not meant to have their temperature constantly varied. A typical laser diode will have an average life span of approximately 10,000 hours, but this life span will decrease by 50%

for each variation of 10°C above the ambient temperature. While the 50% decrease can only considered a general rule of thumb, the correlation between life expectancy of a laser diode and its operating temperature was supported by research conducted by ILX Lightwave Corp. in 2006 [53].

Table 2 – Function Generator Settings.	
Peak-to-Peak	5 V
Offset	2.5 V
Frequency	175 mHz
Duty Cycle	30%

4.3 Delay Line Calibration

Once the settings of the tunable laser were established, the next step was the design of the reference interferometer. As stated in Chapter 3, introducing a delay line into one of the arms would generate an interferogram, and the length of this delay line was required for signal analysis. The length of the delay line needed to fulfill two requirements: be sufficiently longer than the desired sample thickness to be measured but remain shorter than the coherence length of the laser. The length of the delay line thus ensured that the signal of the reference interferometer was generated while the laser remained within its coherent state and sufficient points existed on the reference signal to properly perform the interpolation process to achieve resampling on an equidistant frequency grid. Selected with the goal of measuring a 10cm sample, the delay line needed to be at least ten times larger than the sample thickness but shorter than the laser's approximately 30m coherence length.

In order to determine the precise length of the delay line, a frequency comb was used as an input source, with a repetition rate of 100MHz, or a period of 10ns. Knowing the time delay between the pulses corresponding to each arm of the reference interferometer then allowed the calculation of the precise length of the delay line, as shown on Figure 37. A rough estimate was initially carried out using a measuring tape. The two pulses observed at each repetition were due to the two arms of the interferometer, and the length estimate of 2m enabled the 10ns ambiguity caused by the comb repetition rate to be lifted. The correct pulses for each arm could then be successfully identified to determine the length of the delay line.

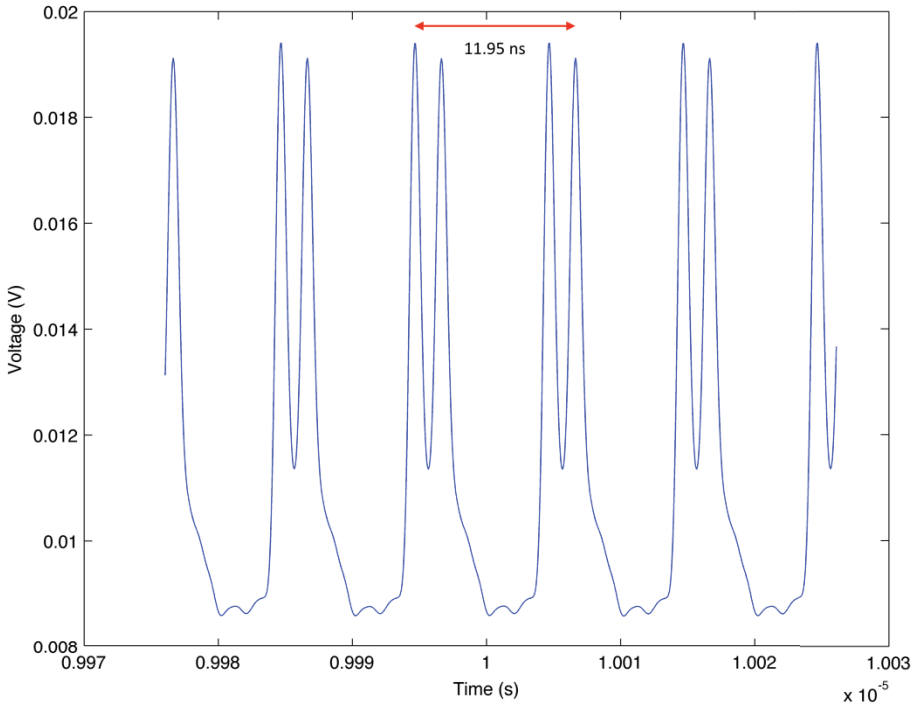

Figure 37 – Delay Line Calibration with Frequency Combs.

For the current experimental setup, this time delay was determined to be 11.95ns, which led to a delay line measuring 2.4388m. All the thickness measurements given in this thesis will be relative to this length. This calculation is easily performed using the principle that the speed of light in vacuum is equal to the distance divided by the time traveled. The refractive index of the inside of a fibre optic cable, 1.47, must also be considered:

$$c = \frac{n \cdot \ell}{\Delta t}. \qquad (46)$$

4.4 Indoors Measurement Setup

With the delay line properly calibrated, the frequency swept interferometer setup could be completed with the goal of being optimized for the indoor measurement campaign. The experimental setup for the indoor measurement campaign is depicted in Figure 38, with the specifications and part numbers of the components provided in Appendix A.

The signal from the tunable laser was input into a polarization controller, which served the purpose of ensuring that the proper polarization state was sent into the optical hybrid. A 10/90 coupler then divided the signal, with 90% being sent into the sample arm that would probe the target. A 10/90 split was required due to the minimum 0.001 mW input power required by the erbium-doped fibre amplifier (EDFA). As seen on the figure below, the delay line was accomplished by a polarization controller that also allowed the matching of the polarization states between the two arms of the reference interferometer to maximize the modulation.

Finally, the optical hybrid was selected in order to facilitate the extraction of the instantaneous phase of the reference signal through signal analysis. Designed by Optoplex Corporation, this component accepted the fields of the reference interferometer as an input and was able to generate the reference interferogram (0^o) and an offset version (90^o) [54]. The use of MATLAB then allowed the instantaneous phase of the reference signal to be determined, which was required to successfully determine the thickness of the sample. Readily available Thorlabs Inc. detectors were used capture the 0^o and 90^o signals.

With the reference interferometer properly established and calibrated, the indoor measurement campaign could begin. The purpose of this campaign was to obtain data that would enable the development of the MATLAB code that would be used for signal analysis. Since the telescope and launching head were being used in the remote sensing laboratory on another project, an optical circulator used in conjunction with a fibre collimator was used as the LADAR head. Just like on the telescope and detection sub-system that would be used for the outdoor measurement campaign, a 200μm diameter avalanche photodiode (APD) was used as the detector in the sample arm to allow better sensitivity in collecting the few photons backscattered by the sample. An electrical pre-amplifier collected the APD output, filtered the background noise and amplified the signal prior to being sent to the oscilloscope.

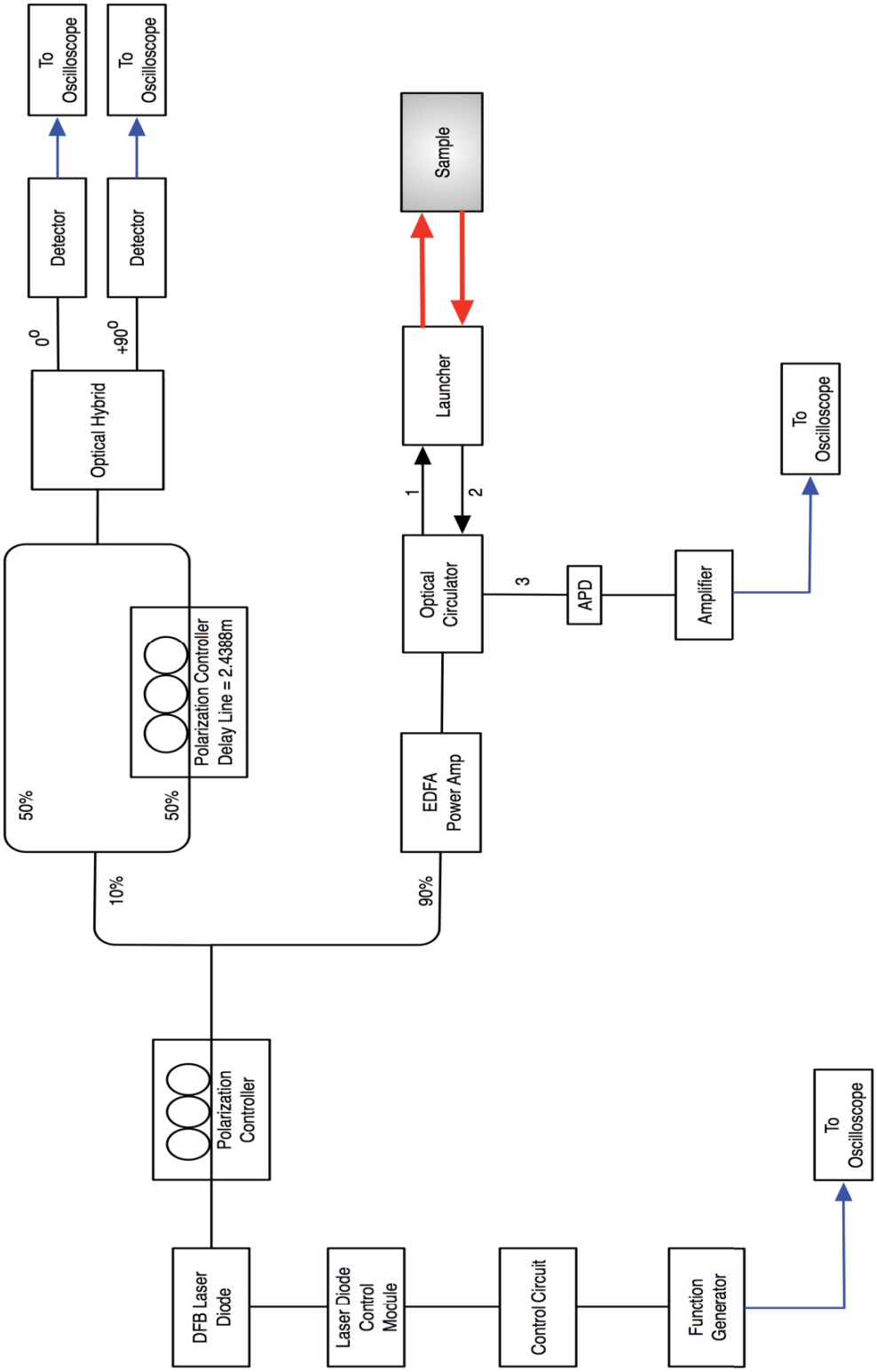

Figure 38 – Bloc Diagram of Indoors Experimental Setup.

Alignment was done manually using a laser-viewing card to ensure that the reflections from the sample were returned back into the fibre collimator. In other words, the card was used to ensure the angle of incidence was initially 0^o and the specular reflection was being detected. The sample was also slightly turned and a spectralon block placed behind the sample to detect the sample signature from its diffuse reflection; a more representative setup of the outdoor measurements that were to be performed. The sample was placed at a distance of approximately 30cm from the fibre collimator.

The first set of samples measured were single layers of acrylic and would prove to serve as a baseline for the development of the MATLAB code. Once the code was finalized and the sample thickness was successfully retrieved, additional samples were then measured to validate the code prior to moving onto the outdoor measurement campaign. These samples, ranging from one to four layers of acrylic and BK7, were selected in order to provide a large variety of sample combinations and to verify the capability of the code to detect multiple layers. The layer combinations were also chosen with the outdoor measurement campaign in mind since these same layer stacks would be measured during the outdoor measurement phase.

As previously stated, these multilayer samples were built by stacking together individual samples within the mounting assembly, shown in Figure 39. This assembly provided a 10.795cm x 10.795cm target for the laser beam.

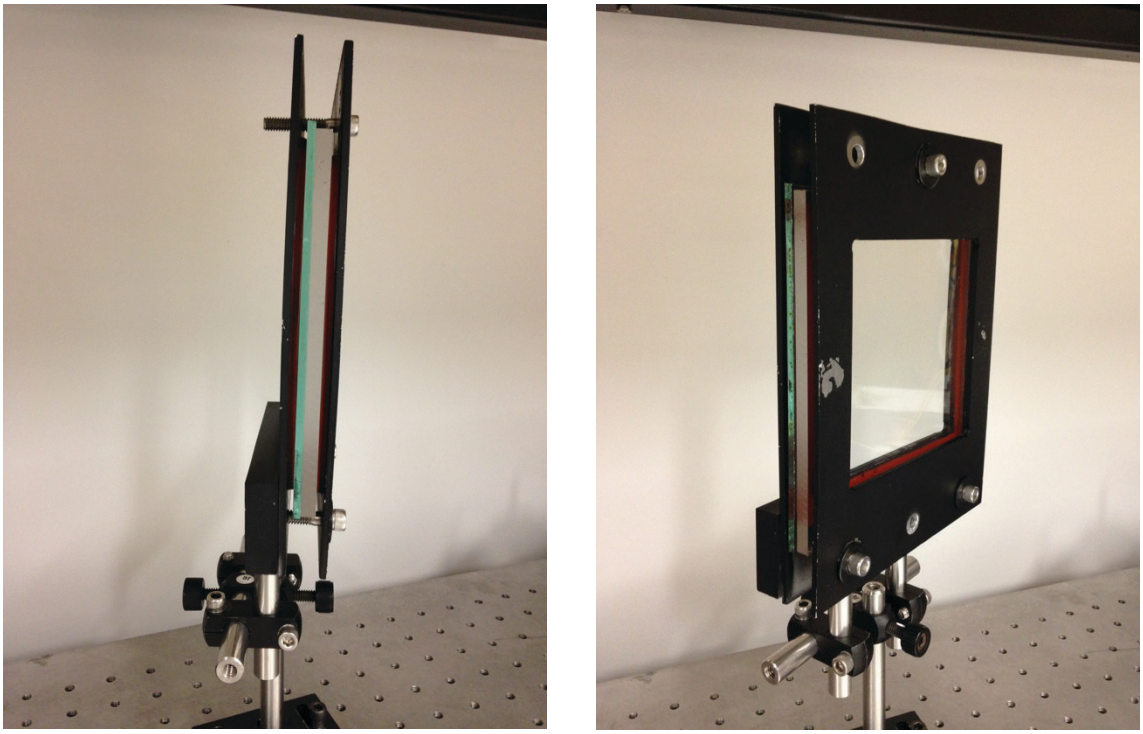

Figure 39 – Sample Mounting Assembly Side View (left) and Front View (right).

With the successful detection of multilayer samples in the laboratory, the experimental setup was moved to the third floor remote sensing laboratory to perform the outdoor measurement campaign.

4.5 Outdoor Experimental Setup

The outdoors experimental setup used to perform the detection of the multilayer samples is depicted in Figure 40, with the specifications and part numbers of the components provided in Appendix A. The following sub-sections will provide details about the beam launching, telescope and detection sub-system, and the limitations on the angle of incidence with this current setup.

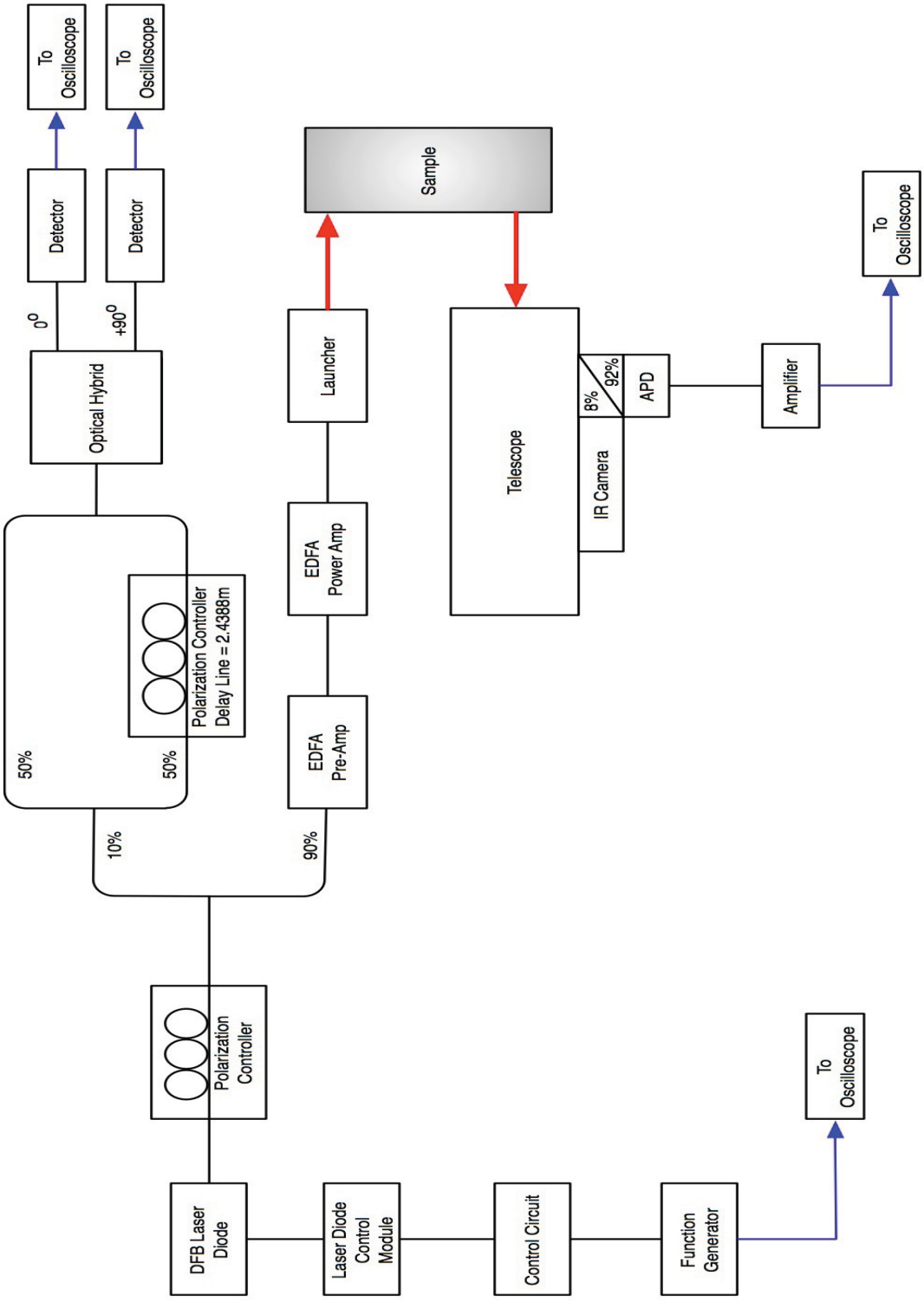

Figure 40 – Bloc Diagram of Outdoors Experimental Setup.

4.6 Beam Launching

The beam launching as well as telescope and detection sub-systems, designated as the LADAR head, were mainly designed by Sylvain Boudreau, a doctoral student from Université Laval during experiments carried out in 2011-2012. The following sections describing these systems are mainly derived from the report detailing the results of hyper spectral LADAR using frequency combs [1].

As seen on Figure 41, the output of the EDFA entered a pigtailed fibre collimator followed by an adjustable beam expander (right side of picture). The beam expander enabled the placement of the beam waist at the desired location in the FOV. The launched beam hit a 2" (50.8mm) gold mirror at 45^{o} and a gold-coated prism attached to the obscuration ring holding the telescope secondary mirror, which allowed locating the launched beam on the same axis as the observation telescope. The measurement of multiple targets was thus simplified since the beam hit all targets on the optical axis independent of the distance.

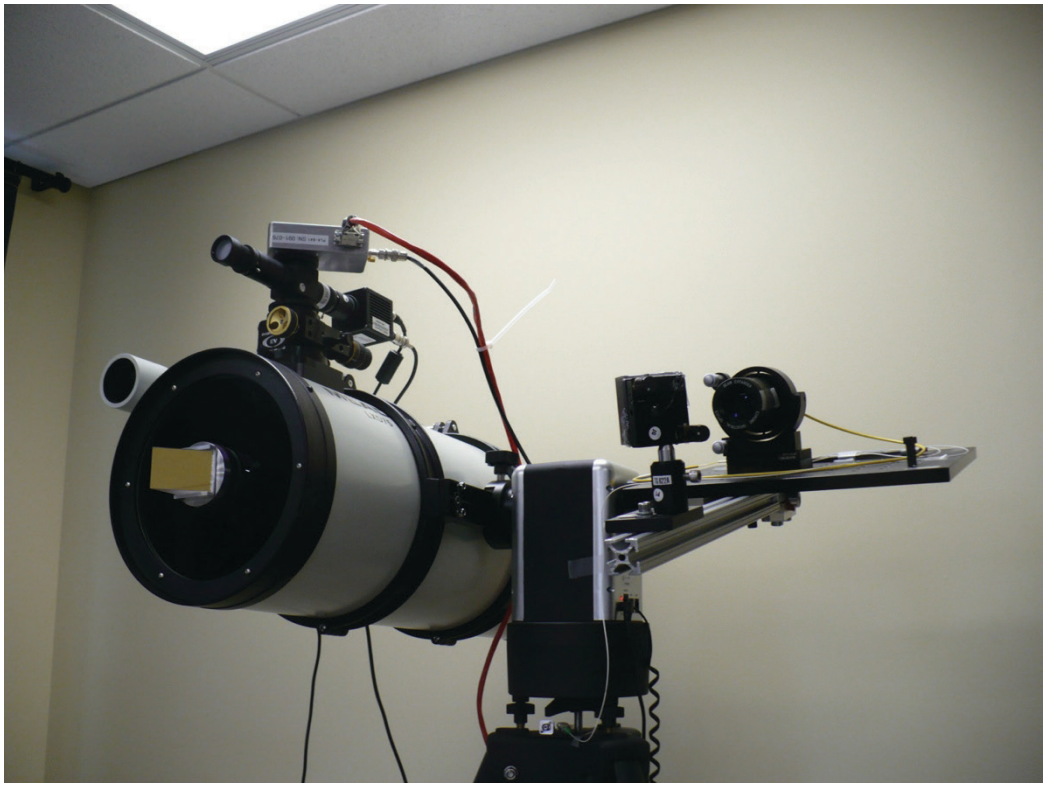

Figure 41 – Beam Launching and Telescope Subsystem.

4.7 Telescope and Detection System

A Meade LDX75 series astronomical telescope collected the reflections emitted from the samples. This telescope, identified as an 8" (203.2mm) f-4 Schmidt-Cassegrain telescope, was chosen during the initial design in 2011 due to its commercial availability and high f-number.

The detection subsystem, shown in Figure 42, had a main function of focusing the light gathered by the telescope onto an APD, which produced a flood of photoelectrons from a single incoming photon. To ensure proper alignment between the launching head, telescope, detector and the scene, a short wave IR (SWIR) indium gallium arsenide (InGaAs) camera was used. The camera was able to simultaneously image the scene in the FOV as well as image the APD. Converging light from the telescope encountered an 8/92 beam splitter, with 92% of the light being directed towards the APD.

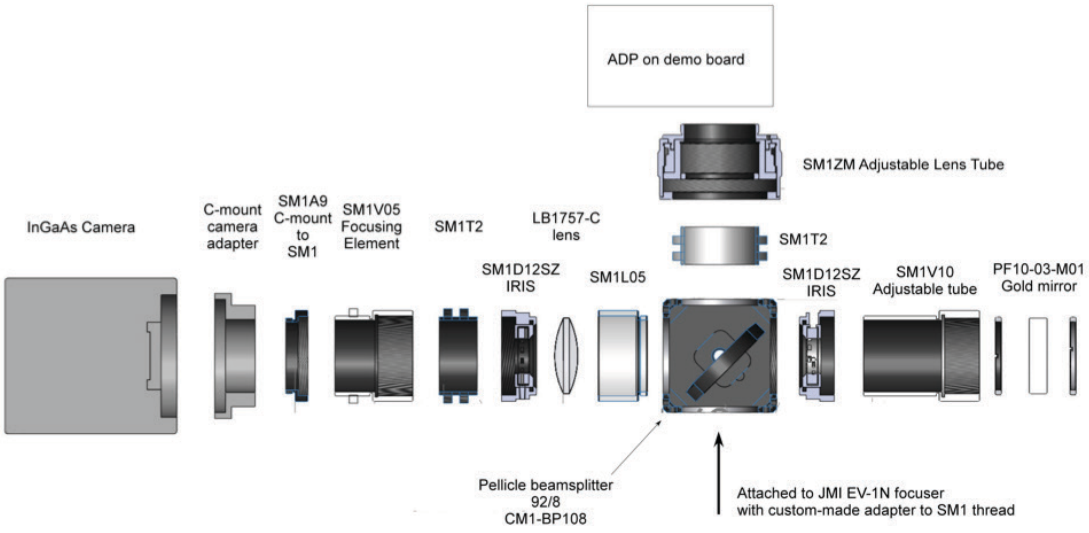

Figure 42 – Detection Subsystem, from [1].

By imaging the APD's focal plane, the camera allowed the visualization of the location of the incoming light with respect to the location of the photosensitive surface, thus drastically simplifying the bore sighting. Placing a gold mirror in the beam splitter port facing the camera had the benefit of also imaging the scene on the camera. The main advantage of the dual use of the camera was the ability to align the APD with the measured sample by superimposing the image of the APD to the image of the scene. Figure 43 provides a screenshot of the IR camera monitor. One is able to observe the

retro-reflective tape patches, which allowed for easy identification of the observed quadrant in the target box structure and provided an approximate position on this quadrant. The small dark circle in the middle of the image is the APD.

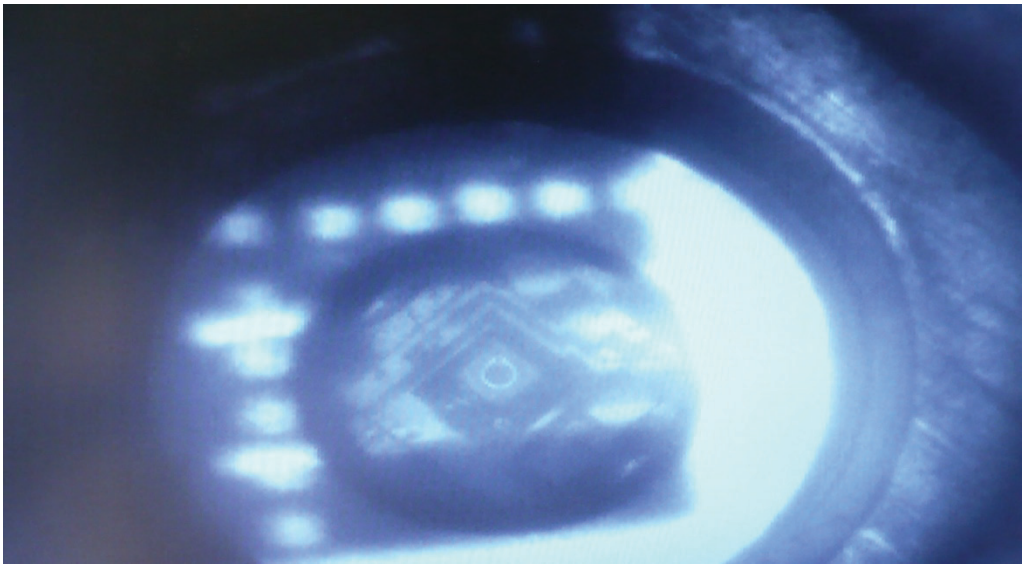

Figure 43 – Screenshot of IR Camera Monitor with Detector Centered in FOV.

4.8 Limitations on the Angle of Incidence

Prior to performing the outdoor measurements, the limitations on the angle of incidence for a sample thickness had to be determined based on the components used in the LADAR head. As previously mentioned, the pigtailed fibre collimator entered the beam expander prior to being launched towards the scene. The maximum angle of incidence for a specific sample thickness is limited by the maximum divergence half angle of the beam. Using the product specifications of the fibre collimator and the fact that its divergence angle is reduced by a factor of the magnification power of the beam expander (20X), the maximum divergence half angle was determined to be 248.5μrad. This divergence angle is the best-case scenario where the launcher is set such as to output a collimated beam. The beam would be more convergent when the beam waist is placed on the target.

As mentioned in Section 3.7, the modulation efficiency decreases as the angle of incidence increases. As such, maintaining a modulation efficiency of 60% for successful detection is desired which means that the argument of the jinc function in Eq. (44) must be less than two. Knowing the maximum divergence half angle of the beam and the central wavelength of the laser source, Eq. (44) can be used to determine the shear the system is able to tolerate:

$$2\pi\sigma\Delta Y\theta_m \leq 2, \quad (47)$$

$$\Delta Y \leq 2.00mm. \quad (48)$$

Inputting the result that the shear must be less than or equal to 2.00mm into Eq. (43) and re-arranging the equation, it is possible to obtain the angle of incidence tolerated by the experimental setup for the thickness of the sample under test. For simplification purposes, a refractive index of 1.5 for tempered glass is assumed:

$$e = \frac{1.00}{tan\left(sin^{-1}\left(\frac{sin\theta_1}{1.5}\right)\right)}. \quad (49)$$

This equation is plotted in Figure 44 and allows the extraction of the maximum angle of incidence tolerated by the experimental setup for a specific sample thickness.

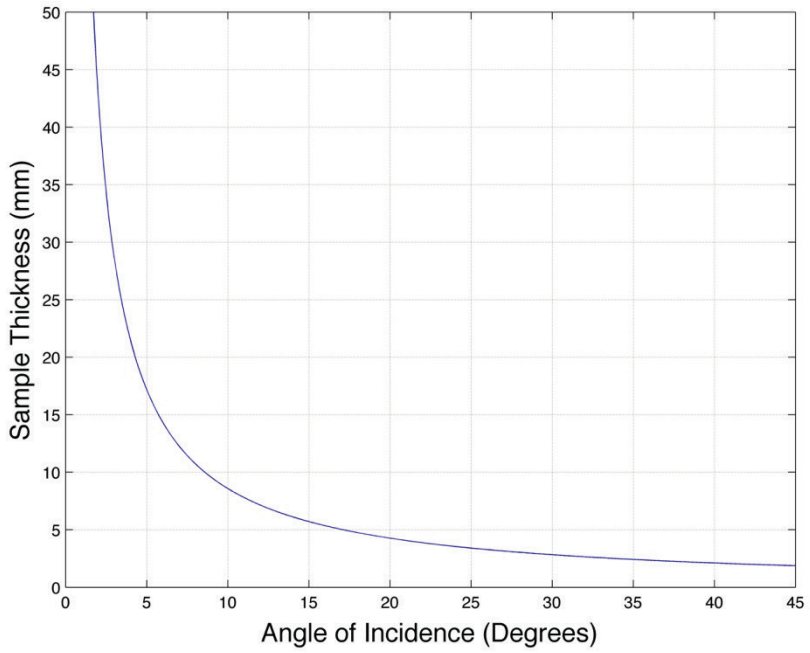

Figure 44 – Sample Thickness vs. Angle of Incidence for a 60% Modulation Efficiency Due to Shear of Interfering Beams.

4.9 Long Distance Setup

The long distance measurements were performed on the Université Laval campus, between the COPL's third floor remote sensing laboratory and the roof of the Abitibi-Price Pavilion, as depicted in a bird's eye view on Figure 45.

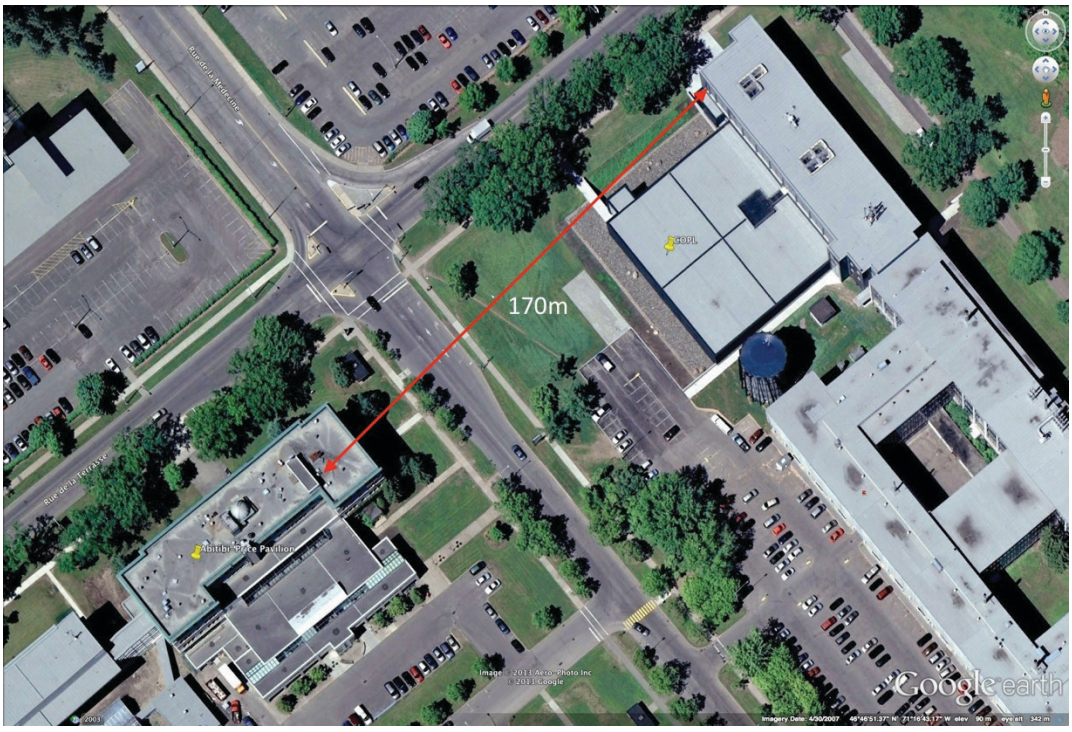

Figure 45 – Bird's Eye View of Measurement Between COPL and Abitibi-Price Pavilion, from [Google Earth].

A 1.22m x 1.22m target box, designed during the experiments performed in 2011-2012 [3], was placed on the roof of the Abitibi-Price Pavilion, with a line of sight distance between the target box and the telescope assembly measured at approximately 170m. This target box provided protection from the elements, was designed for easy mounting of the targets and was painted black to absorb any stray light. Retro-reflective tape inside the box allowed the proper alignment of the telescope and launching head with the target box. Figure 46 provides a view of the target box structure atop the Abitibi-Price Pavilion as seen from the COPL remote sensing laboratory while Figure 47 provides a close-up view of the target box structure.

Figure 46 – Target Box Structure Mounted on Roof of Abitibi-Price Pavilion seen from COPL Remote Sensing Laboratory.

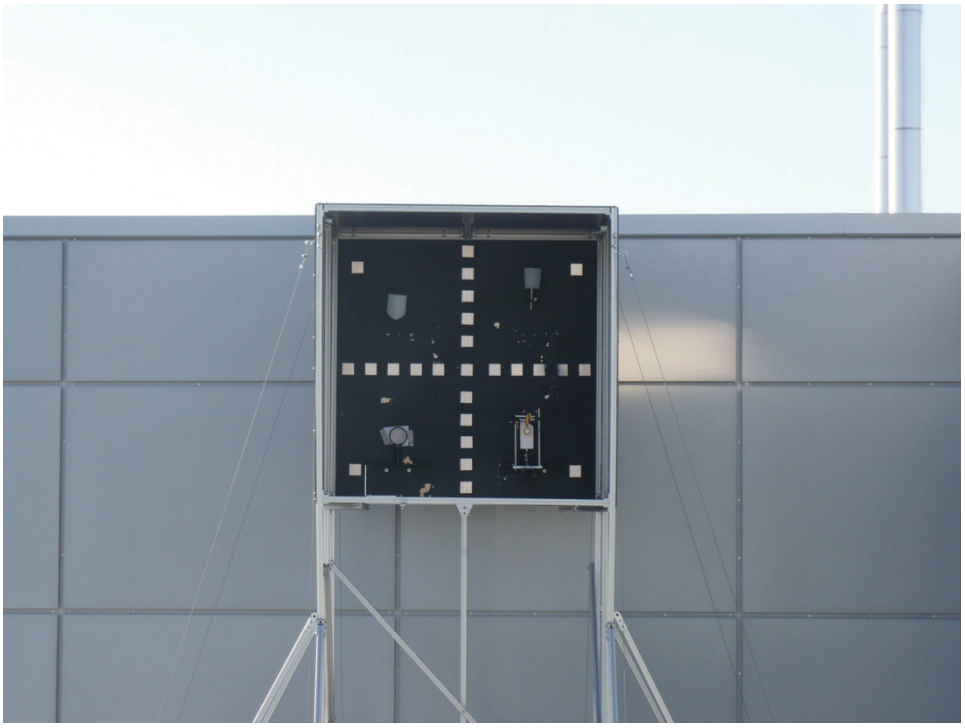

Figure 47 – Close Up of Target Box Structure.

The measurements were performed both in reflection and transmission, with a piece of paper acting as a diffuse reflector placed behind the samples. The sample assembly device was mounted on a precision rotation mount, which allowed the angle progression measurements to be performed. This rotation mount was positioned in one of the quadrants of the target box structure. The other quadrants weren't used for the measurement campaign since only one mounting assembly was manufactured.

All measured samples were initially aligned at 0^o angle of incidence to measure the specular reflection. The initial alignment was accomplished by ensuring that, while standing on a predetermined spot on the roof, one's face fell within the sample's edges while looking at their reflection on the sample. Minute adjustments using the rotation mount as well as the telescope alignment were then performed once the laser was turned on and the light was seen on the IR camera monitor. The intensity of the reflected light and the effects of rotating the samples were clearly visible on the IR camera monitor. The samples were then rotated to ensure that the specular reflection was no longer detected, starting with a 1^o angle of incidence and increasing.

A simple diagram helps validate that a 1^o turn eliminates the detection of specular reflection. As shown on Figure 48, turning the sample 1^o creates a separation of 5.936m from the incident and reflected beam, whereas the telescope has an aperture of 0.2032m.

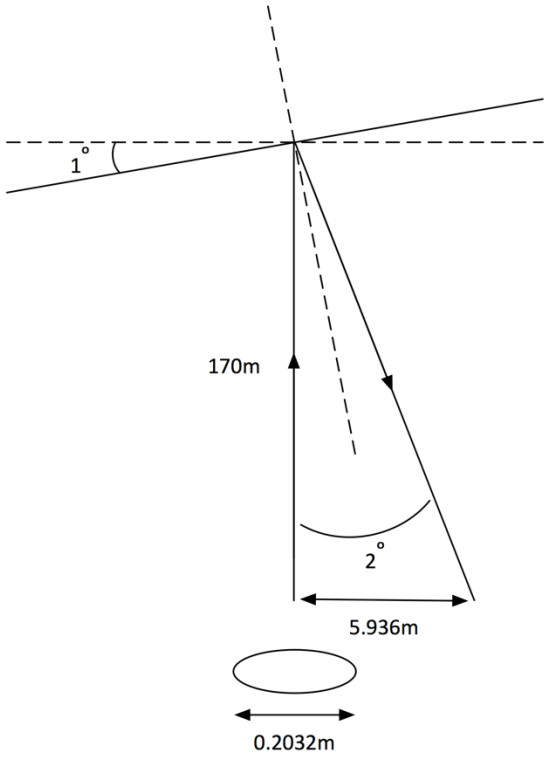

Figure 48 – Incident and Reflected Beams for a 1° Rotated Sample (Not To Scale).

4.10 Outdoors Measurement Programme

The outdoor measurement campaign was conducted during a span of two weeks in the fall of 2013 during the days with promising weather (i.e. sunny). Measurements weren't performed during rainy days since the results would be contaminated due to light diffraction caused by raindrops. Since the telescope setup was shared with another student and the target box structure had to be dismantled by mid-November per university regulations, a two-week window was scheduled and deemed sufficient to perform all necessary measurements.

In total, 10 samples were measured. The layer order is provided in Table 3, with layer 1 being placed closest to the launcher. These layer combinations were selected based on the results of the indoor measurements and to provide a breadth of results for the outdoor measurement campaign. Each sample was measured at 0°, 1° and 5° angle of incidence with selected samples being measured all the way to their maximum angle tolerated by the setup in order to verify the validity of the angle of incidence limitations calculated for a sample thickness. For each separate angle of incidence, the oscilloscope took a total of 150 acquisitions. This number of acquisitions was deemed a good quantity

for averaging purposes without taking too much time since it took nearly 15 minutes to perform these 150 acquisitions.

Of the 10 samples measured, a client from a previous contract with the research group provided two samples. These samples were industry-manufactured stratified media and would contribute to the extensiveness of the samples being measured. An additional sample was deemed too damaged for the outdoor measurements since multiple cracks could be seen across the sample's face. This sample, along with the other two, was measured in the laboratory afterwards for control purposes. Appendix B provides the results of the possible layer combinations.

Table 3 – Outdoor Measurement Campaign Sample Layer Order and Angles of Incidence Measured.

Material / ID	**Layer 1 (mm)**	**Layer 2 (mm)**	**Layer 3 (mm)**	**Layer 4 (mm)**	**Angle of Incidence Measured (^{o})**
BK7	3.184	-	-	-	0, 1, 5, 10, 15, 20, 25, 30
Acrylic	1.88	-	-	-	0, 1, 5, 10, 15, 20, 25, 30, 35
Acrylic	6.12	-	-	-	0, 1, 5, 10, 15, 20
Acrylic & BK7	6.12	3.184	-	-	0, 1, 5
Acrylic	6.12	2.19	-	-	0, 1, 5, 10, 15
Acrylic & BK7	6.12	3.184	1.88	-	0, 1, 5
Acrylic	2.19	6.12	1.88	-	0, 1, 5
Acrylic	2.19	6.12	1.88	2.947	0, 1, 5
P411	10.4	1.80	15.0	-	0, 1, 3, 6, 10
P427	15.9	2.50	12.8	-	0, 1, 3, 6, 10

Finally, since time allowed it, the single layer BK7 sample was also measured with two separate fabric samples placed behind it acting as a diffuse reflector rather than the piece of paper. The purpose of these experiments, conducted at both 1^o and 5^o angle of incidence, was to assess the impact of using a reflector with a lower diffuse reflection coefficient. The first fabric sample was a dark-color cotton fabric while the second article was a nylon fabric of the same color.

5 Results and Analysis

The following chapter provides the results from both the indoor and outdoor measurements. Prior to the presentation of the results, the signal analysis process is described, providing graphical results at key steps in the analysis. Finally, a few areas for improving future experiments of this type are discussed to conclude the chapter.

The results depicted below are an averaging of multiple acquisitions by the oscilloscope. In certain cases, some of the acquisitions had to be removed manually since they were corrupted and crashed the MATLAB code. This could be a case of a lag from the oscilloscope while saving its data onto its hard drive.

5.1 Signal Analysis Process

The following section demonstrates the steps performed during the signal analysis to retrieve the effective thickness of the sample under test. The complete MATLAB code used for the signal analysis can be found in Appendix C. All figures are from the processing of a 6.12mm acrylic sample measured indoors in reflection. The final result is analyzed in the following section.

The first step in the processing algorithm was the importing of the necessary data used for the signal analysis. These were the signals arising from: the reference interferometer, the 90^{o} offset reference interferometer and the sample under test. Multiple acquisitions were taken by the oscilloscope in order to allow data averaging to be performed. Each acquisition was therefore run through the analysis algorithm to retrieve the autocorrelation of the sample under test and then averaged prior to generating the final autocorrelation figure. Figure 49 represents the raw data imported into MATLAB prior to the analysis being performed. The raw data depicted represents the data acquired when the oscilloscope is triggered on the positive value of the square wave originating from the function generator of the tunable laser diode control circuit.

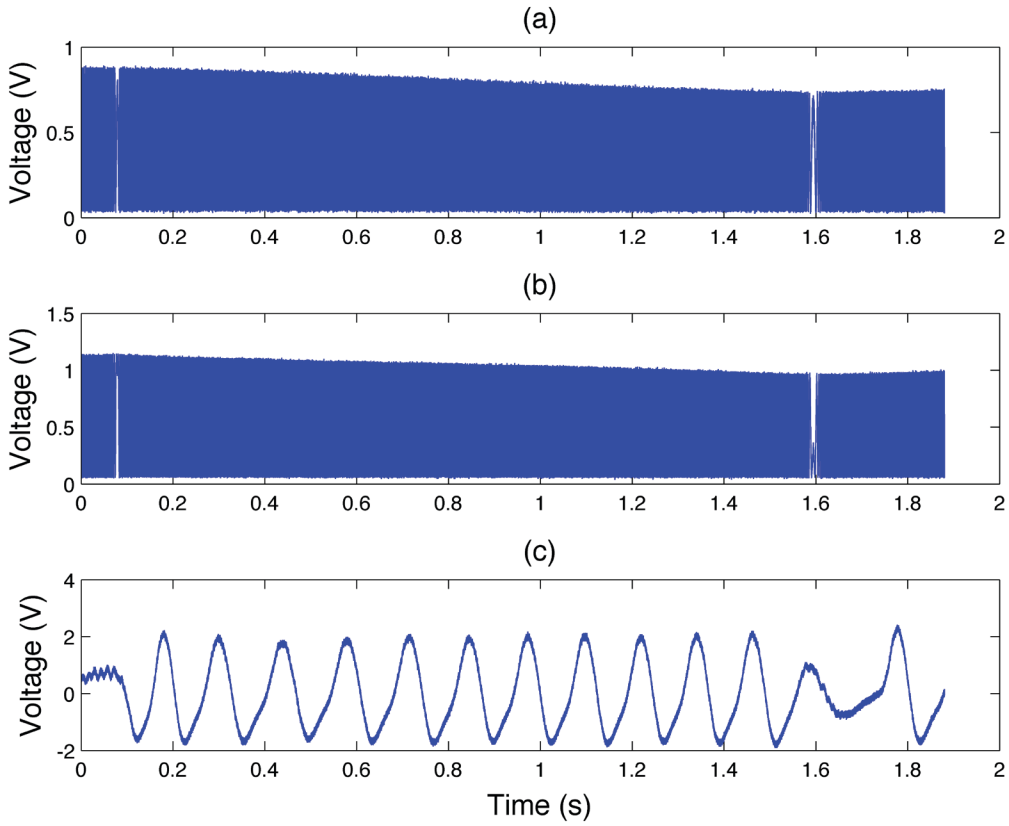

Figure 49 – Raw Data Acquired From (a) Reference Interferometer (b) Offset Reference Interferometer and (c) Sample Under Test.

The next step in the analysis process was to center the reference signal, and its 90° offset, to zero and normalize from negative one to positive one. This would ensure that both reference signals (0° and 90°) were analyzed on the same scale. A simple 50-point moving average filter through the use of a convolution was then employed to filter out the background noise. Figure 50 provides a close-up view of the overlap of the raw (blue) and filtered (red) reference interferometer signal. The multilayer sample signal was also centered and normalized in order to remove the DC component of the signal. The DC subtraction allowed the removal of the peak at the ZPD on the autocorrelation, which enabled a better identification of the peaks of interest.

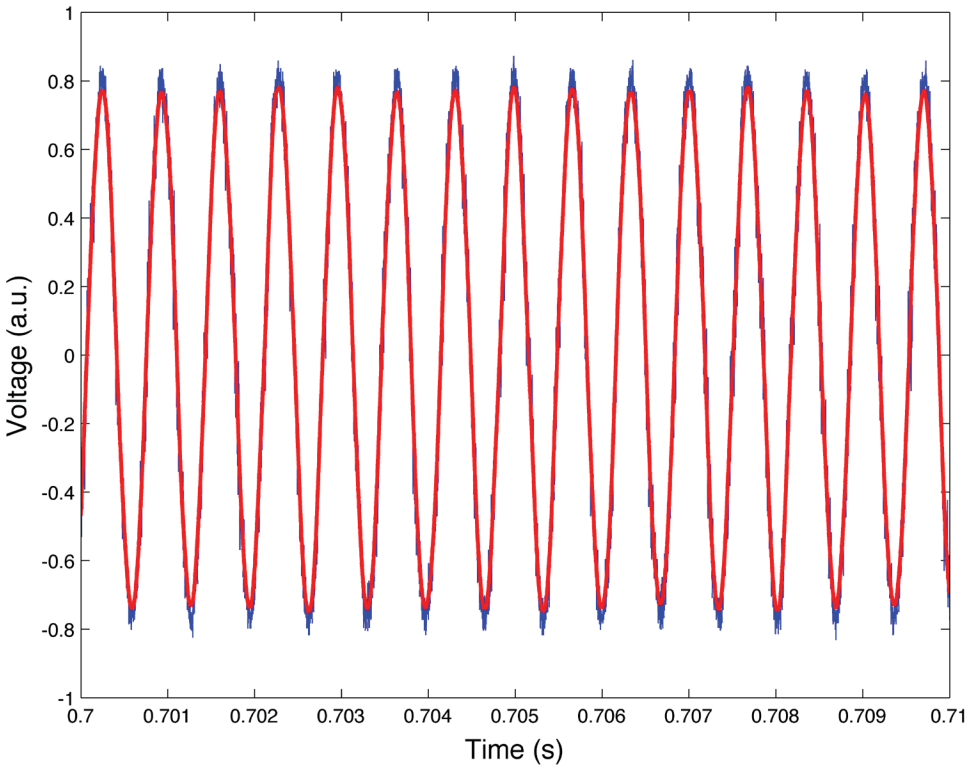

Figure 50 – Overlap of Raw Reference Signal (blue) and its Filtered Signal (red).

Following the filtering process, the instantaneous phase of the reference signal was obtained by performing the four-quadrant inverse tangent (atan2) between the reference signal and its offset. The desired start and end points on the unwrapped instantaneous phase for the interpolation process were then manually selected, as shown on Figure 51. To simplify the signal analysis, the start and end points were selected on the main slope of the phase, thus only selecting the signal when the laser diode was increasing its wavelength. Furthermore, only the positive slope was selected for the interpolation process since MATLAB's 'interp1' function was only capable of performing the interpolation on a monotonically increasing vector.

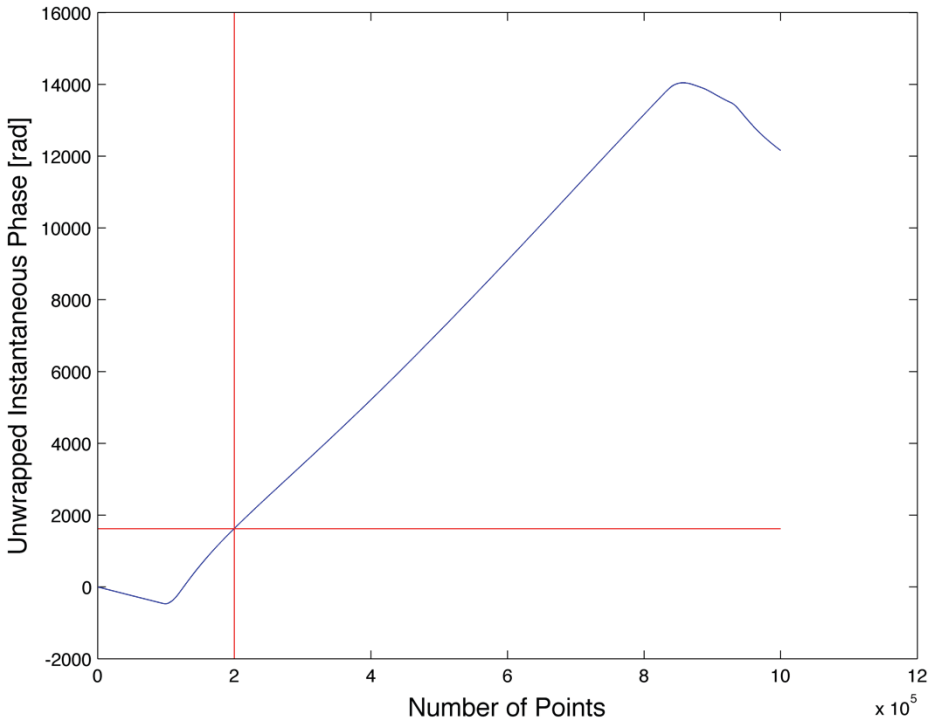

Figure 51 – Manual Selection of Start and End Points of the Instantaneous Phase of Reference Interferometer Signal.

The next step was to build the time vector, which was interpolated for every multiple of 2π of the unwrapped instantaneous phase of the reference signal. This allowed the extraction of the points where the wavenumber increment was an integer of the length of the delay line (ℓ) multiplied by the refractive index of the fibre optic cable (n). This same time vector was then used to sample the multilayer signal on an equidistant grid of known wavenumber increments. MATLAB's 'detrend' function was also applied to the multilayer signal to remove any linear trend in the signal. Prior to performing the inverse Fourier transform, a hamming window was applied to the interpolated multilayer sample signal in order to apodize the signal and remove the ringing observed on the autocorrelation figure. Figure 52 provides a graphical representation of the multilayer signal prior to and following the application of the hamming window.

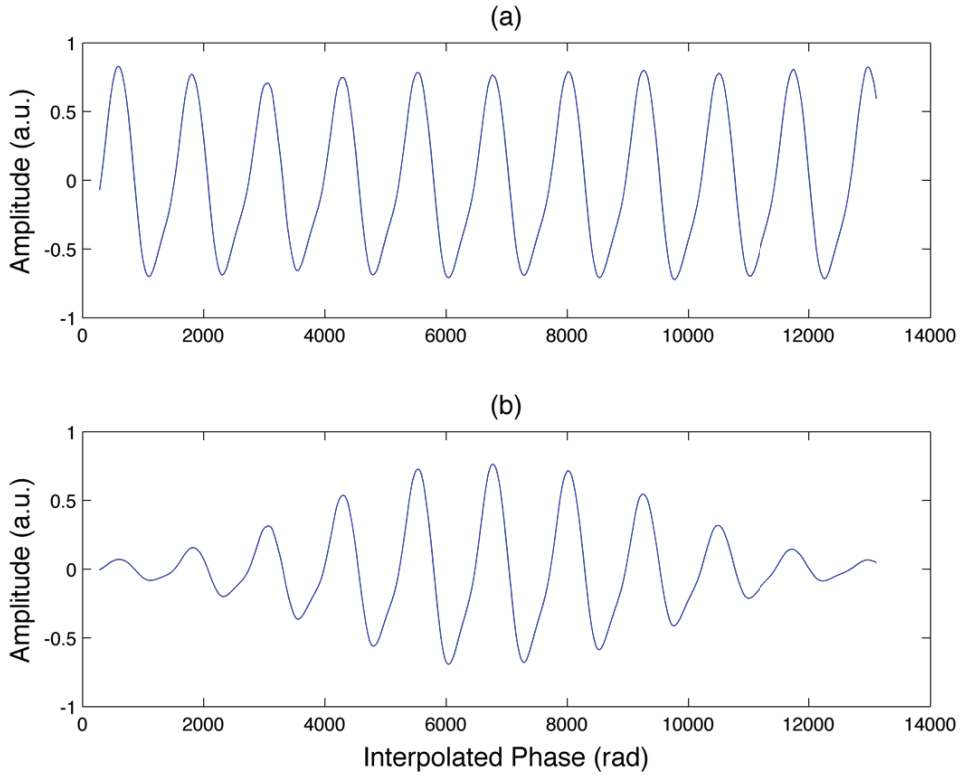

Figure 52 – Interpolated Multilayer Sample Signal (a) Prior to Application of Hamming Window and (b) Following Application of Hamming Window.

Finally, following the application of the Hamming window, the inverse Fourier transform was performed on the sample signal and the autocorrelation was generated. All the steps previously mentioned, with the exception of the selection of the points on the unwrapped instantaneous phase, were performed for each acquisition of the oscilloscope. Each result of the autocorrelation is saved into a vector, which served to average the autocorrelation of the numerous acquisitions. The averaged version of the single-sided autocorrelation is then presented, enabling the identification of the main peaks and the calculation of the sample's thickness. The peak position was divided by the sample's refractive index to determine the thickness. The autocorrelation was kept on a linear scale with its amplitude normalized to one. Figure 53 provides the single-sided calibrated autocorrelation of a single layer sample with and without the application of the Hamming window. One is also to observe how the Hamming window enabled the removal of the ringing around the peaks of interest. Furthermore, the application of the Hamming window allowed the second and third harmonics of the sample's thickness to stand out and be identified.

The one trade-off of applying the Hamming window is the widening of the peaks, which leads to a decrease in the resolution. As such, with the -3dB main lobe width of approximately 1.30 for the Hamming window, this leads to a decrease in the resolution from 0.61mm to 0.80mm [55].

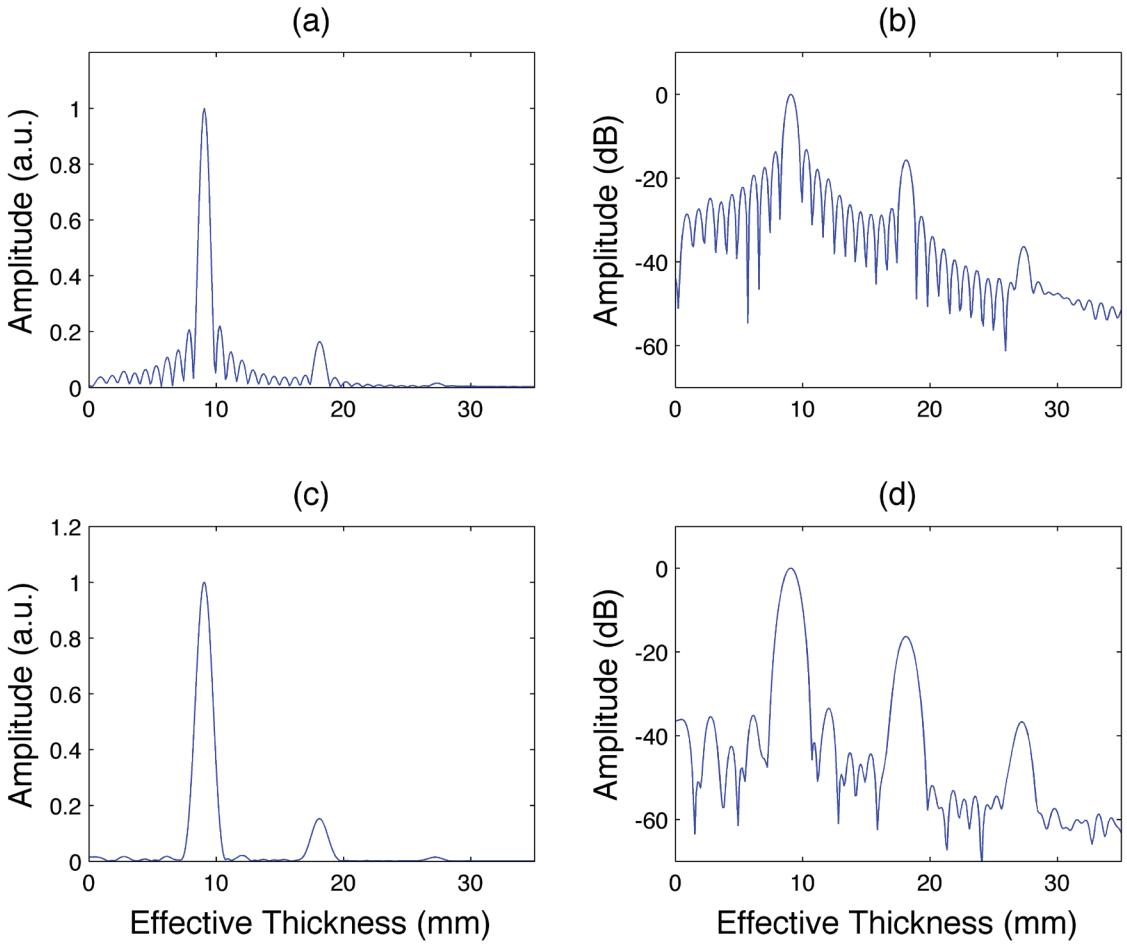

Figure 53 – Autocorrelation of Single Layer Sample Without Application of Hamming Window on (a) Linear and (b) Logarithmic Scale and With Application of Hamming Window on (c) Linear and (d) Logarithmic Scale.

5.2 Indoor Measurement Results

The indoor experiments and resulting measurements were essential to the design process of the experimental setup and the outdoor measurements that were to follow. In addition to facilitating the development of the MATLAB code used to analyze the data, these indoor measurements served as a proof of concept that a tunable laser diode could indeed be used to enable the detection of the individual layers of a multilayer sample. The

results of these samples also acted as a baseline for the outdoor measurements and their expected results.

Six sets of indoor measurements are presented in this section, consisting of:

1) A single layer of 6.12mm acrylic measured in reflection at 0^o
2) A single layer of 6.12mm acrylic measured in transmission at 5^o;
3) A double layer sample of 3.184 BK7 and 6.12mm acrylic measured in reflection at 0^o;
4) A double layer sample of 2.19mm and 6.12mm acrylic measured in transmission at 5^o;
5) A triple layer sample of 3.184mm BK7 in between layers of 1.88mm and 6.12mm acrylic measured in reflection at 0^o; and
6) A quintuple layer sample labeled “Unkown_1” measured in reflection at 0^o.

The samples presented were chosen from the numerous measurements performed in the indoor laboratory phase in order to demonstrate a breadth of results. The goal of this section is to establish that it is possible to detect both the specular reflection of the sample and the diffuse reflections from a lambertian diffuser placed behind the sample.

The refractive index for the acrylic and BK7 are calculated at a wavelength of 1.562μm, resulting in 1.48 for the acrylic and 1.5005 for the BK7 [56].

5.2.1 Single – Acrylic 6.12mm – Reflection – 0^o

Figure 54 and Table 4 represent the detection in reflection of a single layer of acrylic measuring 6.12mm. The figure is the result of the IFFT of the captured reflection spectrum, with the amplitude being normalized to one for simplification purposes. This measurement was performed with an angle of incidence of 0^o, thus detecting the specular reflection. The first peak represents the effective thickness of the layer, with the measured thickness being calculated by dividing the peak position by the refractive index. This peak resulted in a measured thickness of 6.136mm. The second peak, located at 18.10mm and identified by a red circle, can be associated to the second harmonic of the layer (12.24mm

actual; 12.23mm measured). The third harmonic of the layer can also be identified, resulting in a measured thickness of 18.11mm (18.36mm actual).

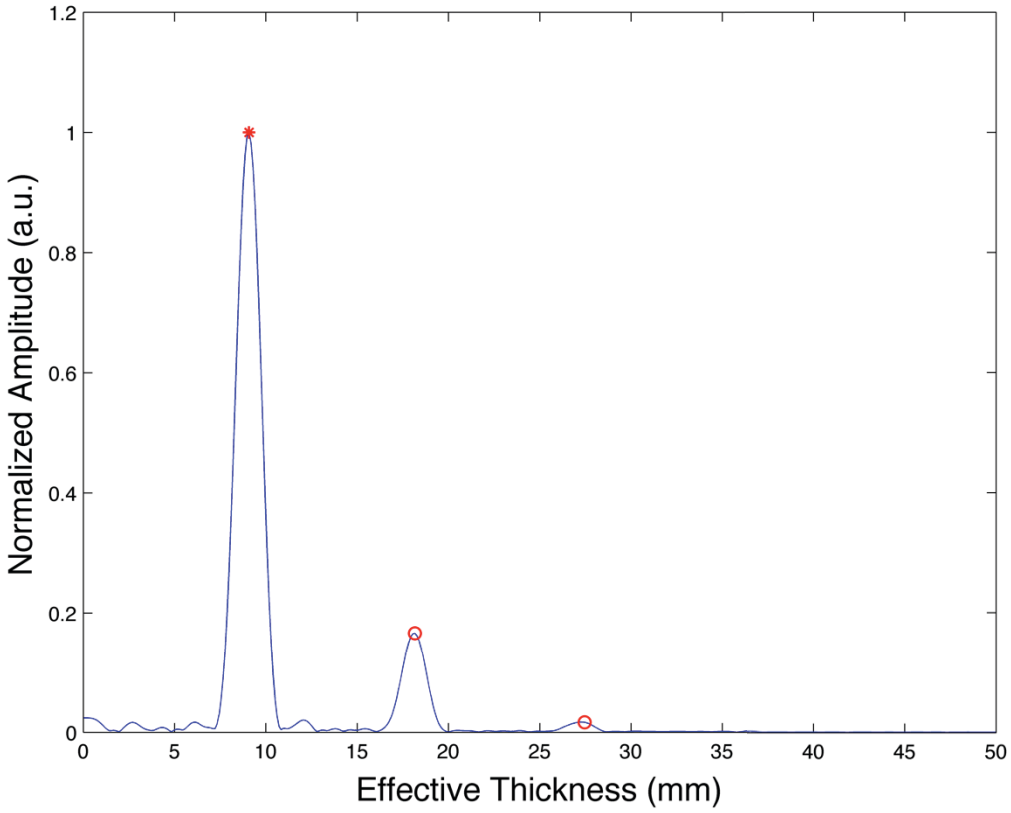

Figure 54 – Single Layer Acrylic (6.12mm); Measured Indoors in Reflection at Angle of Incidence of 0^{o}.

Table 4 – Single Layer Acrylic (6.12mm) Peak Position Explanations; Measured Indoors in Reflection at Angle of Incidence of 0^{o}.				
Actual Thickness (mm)	Peak Position (mm)	Measured Thickness (mm)	Refractive Index	Symbol
6.12	9.081	6.136	1.48	*
12.24 (2^{nd} harm of 6.12)	18.05	12.23	1.48	O
18.36 (3^{rd} harm of 6.12)	26.80	18.11	1.48	O

5.2.2 Single – Acrylic 6.12mm – Transmission – 5^{o}

Figure 55 and Table 5 represent the measurement in transmission of the same acrylic substrate measuring 6.12mm at approximately 5^{o} angle of incidence. A spectralon

block, acting as a diffuse reflector, was placed behind the sample under test. The diffuse reflection is therefore detected, successfully demonstrating that such measurements are capable of being performed. The main peak is the sample's thickness, resulting in a 6.136mm measurement. The second harmonic of the layer, resulting in a measured thickness of 12.27mm, is also identified on the figure.

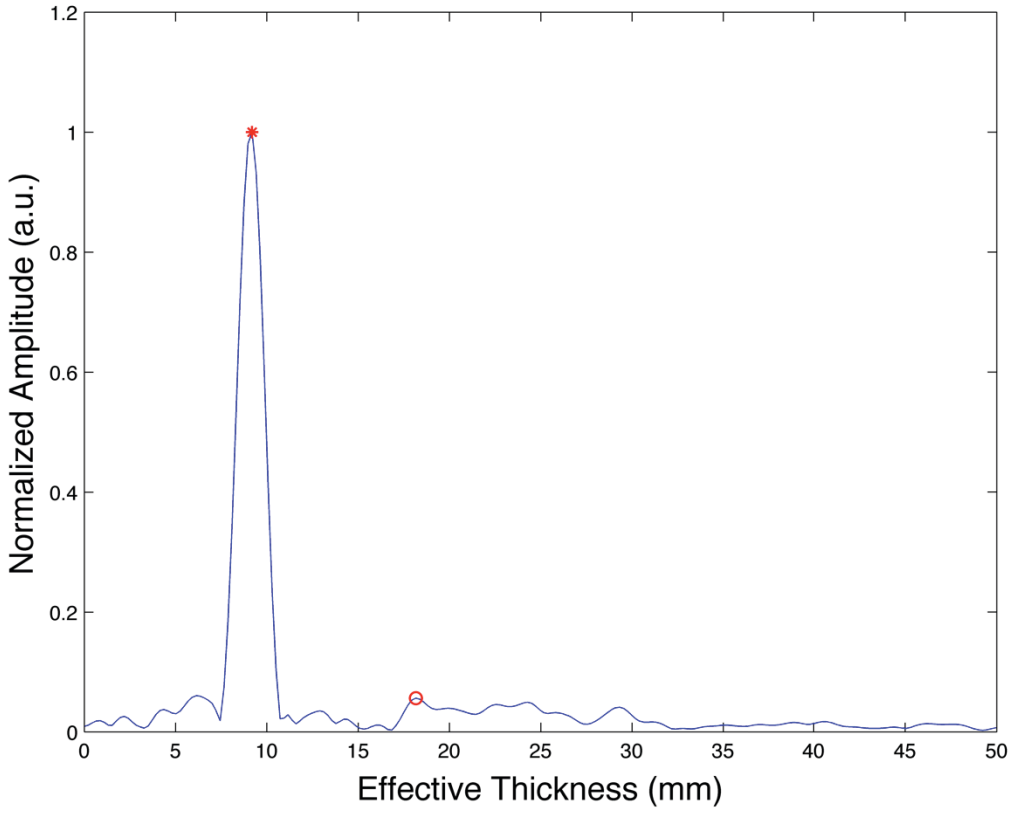

Figure 55 – Single Layer Acrylic (6.12mm); Measured Indoors in Transmission at Angle of Incidence of ~5°.

Table 5 – Single Layer Acrylic (6.12mm) Peak Position Explanations; Measured Indoors in Transmission at Angle of Incidence of ~5°.				
Actual Thickness (mm)	Peak Position (mm)	Measured Thickness (mm)	Refractive Index	Symbol
6.12	9.19	6.21	1.48	*
12.24 (2nd harm of 6.12)	18.16	12.27	1.48	o

5.2.3 Double – BK7 3.184mm & Acrylic 6.12mm – Reflection – 0°

Figure 56 and Table 6 represent the detection in reflection of a double layer sample of BK7 and acrylic at 0° angle of incidence, measuring 3.184mm and 6.12mm respectively. Consistent with the theory proposed in Section 3.5, Stratified Medium Interference, a two-layer sample generated three primary peaks, one for each individual layer and one for the total thickness of the sample. The first peak, associated with the thinner of the two layers, resulted in a measured thickness of 3.208mm. The second peak resulted in a measured thickness of 6.062mm and the third peak, associated to the total thickness, in a measured thickness of 9.418mm. The refractive index for the combination of the two layers is calculated using Eq. (45) as proposed in Chapter 3.

The second harmonic of the total thickness is also identified on the figure by a red circle. The red diamonds represent additional combinations that are observed, with the contributing layers identified in the table below.

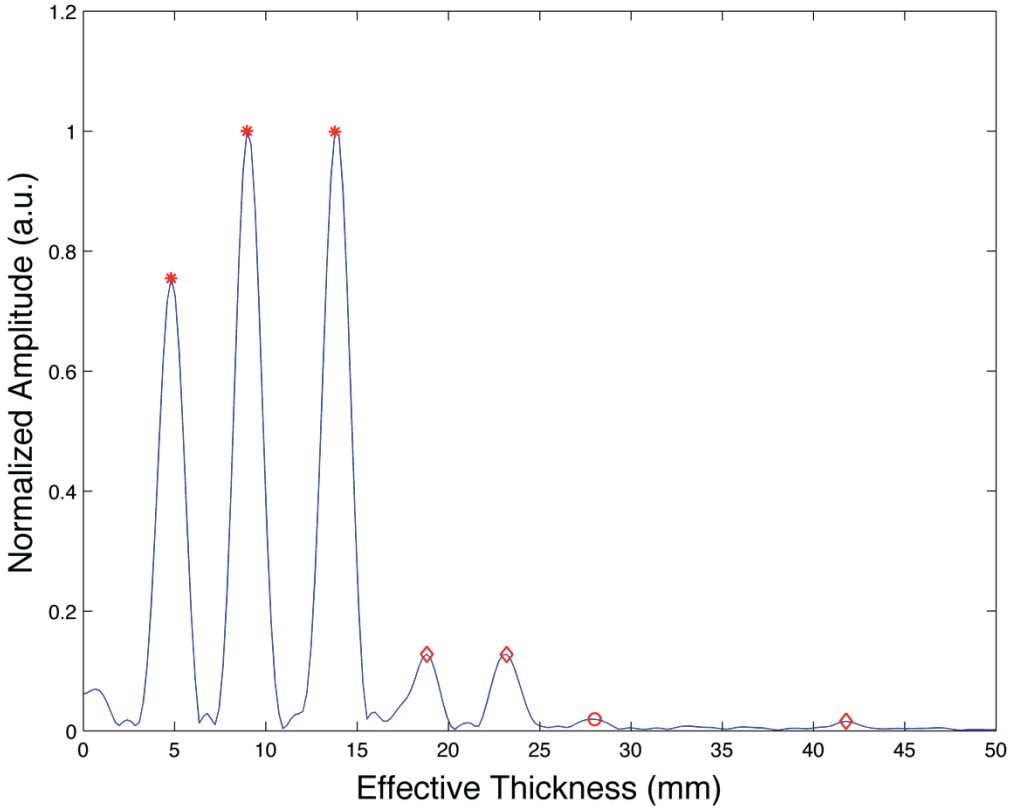

Figure 56 – Double Layer BK7 (3.184mm) & Acrylic (6.12mm); Measured Indoors in Reflection at Angle of Incidence of 0°.

Table 6 – Double Layer BK7 (3.184mm) & Acrylic (6.12mm) Peak Position Explanations; Measured Indoors in Reflection at Angle of Incidence of 0°.				
Actual Thickness (mm)	Peak Position (mm)	Measured Thickness (mm)	Refractive Index	Symbol
3.184	4.814	3.208	1.5005	*
6.12	8.971	6.062	1.48	*
9.304	14.004	9.418	1.487	*
12.488 (3.184+9.304)	18.82	12.631	1.49	◇
15.424 (6.12+9.304)	23.19	15.627	1.484	◇
18.608 (2nd harm of 9.304)	28.01	18.836	1.487	O
27.664 (12.24+15.424)	41.79	28.198	1.482	◇

5.2.4 Double – Acrylic 2.19mm & 6.12mm – Transmission – 5°

Figure 57 and Table 7 represent the measurement in transmission at approximately 5° angle of incidence of a double layer of acrylic measuring 2.19mm and 6.12mm respectively. A spectralon block was once again placed behind the sample. All three of the expected peaks appear on the figure with resulting measured thicknesses of 2.218mm and 6.210mm for the individual layers and a total measured thickness of 8.426mm. This measurement thus confirmed that a double layer sample could be detected in transmission.

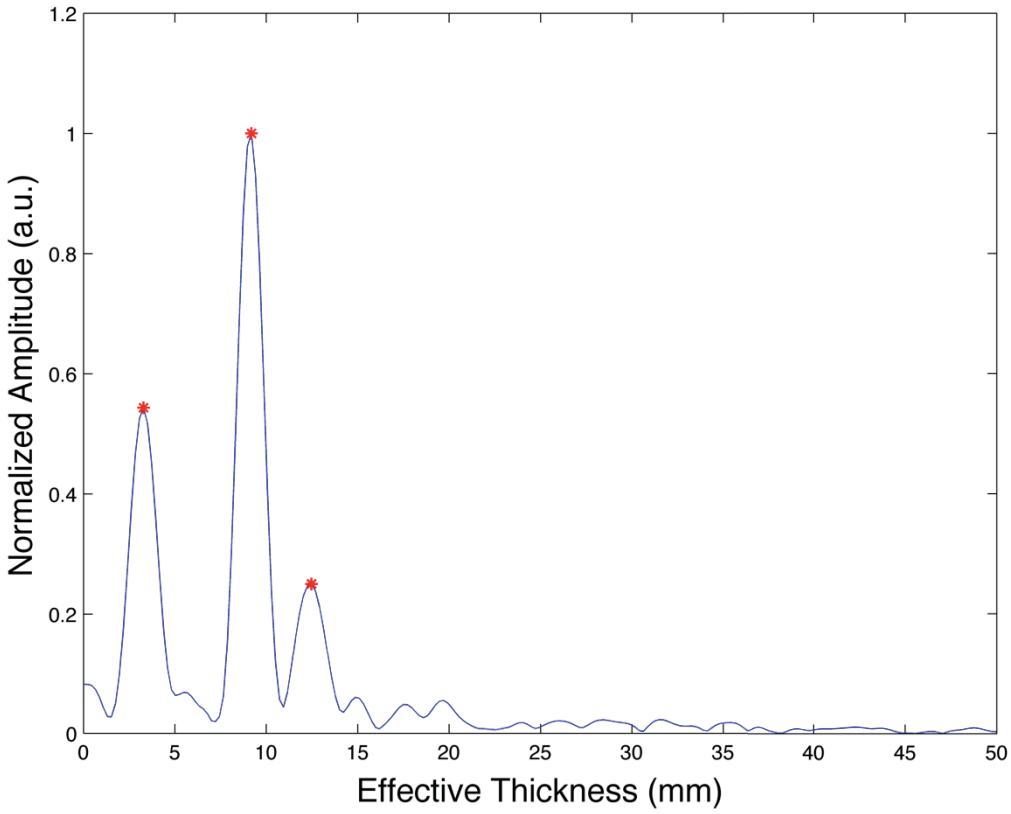

Figure 57 – Double Layer Acrylic (2.19mm & 6.12mm); Measured Indoors in Transmission at Angle of Incidence of ~5°.

Table 7 – Double Layer Acrylic (2.19mm & 6.12mm) Peak Position Explanations; Measured Indoors in Transmission at Angle of Incidence of ~5°.				
Actual Thickness (mm)	Peak Position (mm)	Measured Thickness (mm)	Refractive Index	Symbol
2.19	3.282	2.218	1.48	*
6.12	9.190	6.210	1.48	*
8.31	12.470	8.426	1.48	*

5.2.5 Triple – Acrylic 6.12mm, BK7 3.184mm & Acrylic 1.88mm – Reflection – 0°

Figure 58 and Table 8 represent the measurement in reflection of a triple layer sample, with two layers of acrylic (1.88mm and 6.12mm) and one layer of BK7 (3.184mm) placed in between. One can see on the figure that five of the six primary peaks are identified. The one peak that isn't identifiable is associated to the sum of the 1.88mm acrylic and 3.184mm BK7. The reason this peak isn't present is due to the limited

resolution of 0.80mm of the system. The peak, which should be located at 7.56mm, is too close from the one at 9.19mm. A small kink on the left wing of the 9.19mm is nevertheless visible around 7.56mm.

The weaker surface quality of the 1.88mm of acrylic in comparison to the other layers could explain why its peaks have lower amplitudes. This aspect of surface quality is further explored in the next section. Additionally, since the 1.88mm layer was furthest from the launcher, a lack of optical power could be an explanation for the lower amplitudes of the peaks associated to the layer and its combinations. Since it was confirmed that the 1.88mm acrylic layer was successfully measured by itself, the possibility that this thickness is undetectable is ruled out.

Several secondary peaks are identified on the figure. These are either the second harmonics of a layer or the sum of two peaks. It becomes evident with the measurement of a three-layer sample how the increase in the number of peaks present increases the difficulty in successfully identifying the primary peaks and determining the thickness of the individual layers.

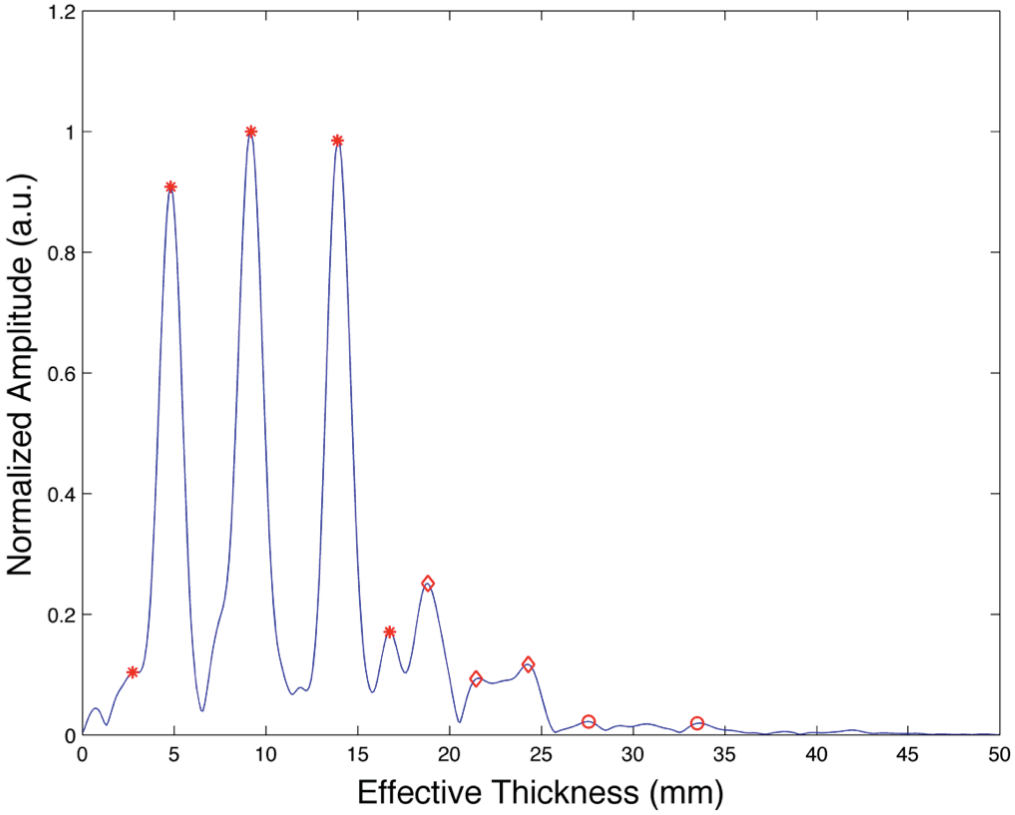

Figure 58 – Triple Layer Acrylic (6.12mm), BK7 (3.184mm) & Acrylic (1.88mm); Measured Indoors in Reflection at Angle of Incidence of 0^{o}.

Table 8 – Triple Layer Acrylic (6.12mm), BK7 (3.184mm) & Acrylic (1.88mm) Peak Position Explanations; Measured Indoors in Reflection at Angle of Incidence of 0°.				
Actual Thickness (mm)	Peak Position (mm)	Measured Thickness (mm)	Refractive Index	Symbol
1.88	2.735	1.848	1.48	*
3.184	4.814	3.208	1.5005	*
6.12	9.190	6.209	1.48	*
9.304	13.895	9.344	1.487	*
11.184	16.74	11.265	1.486	*
12.488 (3.184+9.304)	18.82	12.631	1.49	◇
14.368 (3.184+11.184)	21.44	14.398	1.489	◇
17.304 (6.12+11.184)	24.29	16.368	1.484	◇
18.608 (2nd harm of 9.304)	27.57	18.541	1.487	O
22.368 (2nd harm of 11.184)	33.48	22.530	1.486	O

5.2.6 Quintuple – “Unknown_1” – Reflection – 0°

Figure 60 and Table 9 represent the measurement in reflection at 0° angle of incidence for the sample labeled “Unknown_1”. While on visual inspection it was found that the sample appears to have been damaged and had multiple cracks on its surface, this sample was still measured on the indoors experimental setup since the beam width was small enough not to be influenced by the cracks and the sample could be positioned to minimize the impact of this defect. Since the materials used in this sample are unknown, a refractive index of 1.5 for standard tempered glass in considered.

Analyzing the figure below, one can see that there aren’t as many peaks as the 15 expected for a five-layer sample. The reason for this is that two individual layers appear as one. As such, the number of peaks present would lead one to believe that a four-layer sample is being measured rather than a five-layer sample. Figure 59 represents the layer combinations that are being observed on the autocorrelation figure, where the middle two layers (5.50mm and 1.00mm) appear as one layer. The combination of these four layers (3.00mm, 5.00mm, 6.00mm and 6.50mm) is the result being observed.

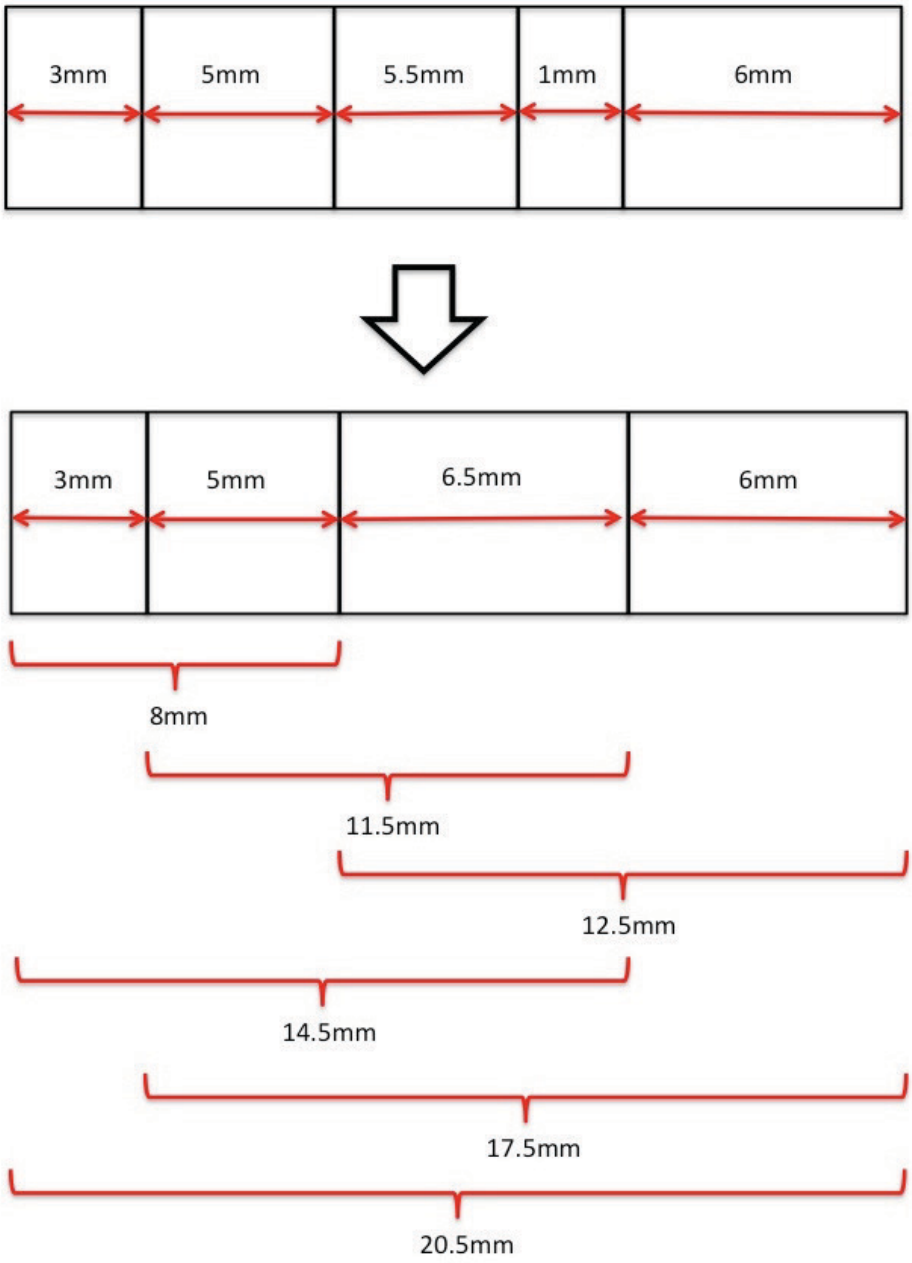

Figure 59 – Layer Combinations of Sample "Unknown_1" Observed During Its Measurement.

Typically, a four-layer is supposed to generate ten primary peaks but only seven are identified in the figure and table below. The missing peaks are associated with the 5.00mm, 6.00mm and 11.5mm possibilities. The reason for these absent peaks is the resolution limitations of the system. Since the system's resolution is calculated to be approximately 0.80mm, the 6mm and 6.5mm, as well as 11.5mm and 12.5mm, are too closely related for their peaks to be differentiated. The 5.00mm layer appears to be have

been enveloped by the peak associated to the 6.5mm layer. This was caused by the application of the Hamming window to the sampled multilayer sample prior to performing the IFFT.

It is evident through visual inspection of the sample that it underwent heat and pressure treatments. As such, it is perfectly plausible to believe that two layers would be fused together to the point of essentially nullifying their mutual interface. This same layer behaviour is also observed during indoor measurements on the other two industrially manufactured samples, labeled “P411” and “P427”. For sample “P411”, the first two layers (1.8mm and 10.4mm) appear as one while the same occurs for the final two layers (2.5mm and 12.8mm) of sample “P427”.

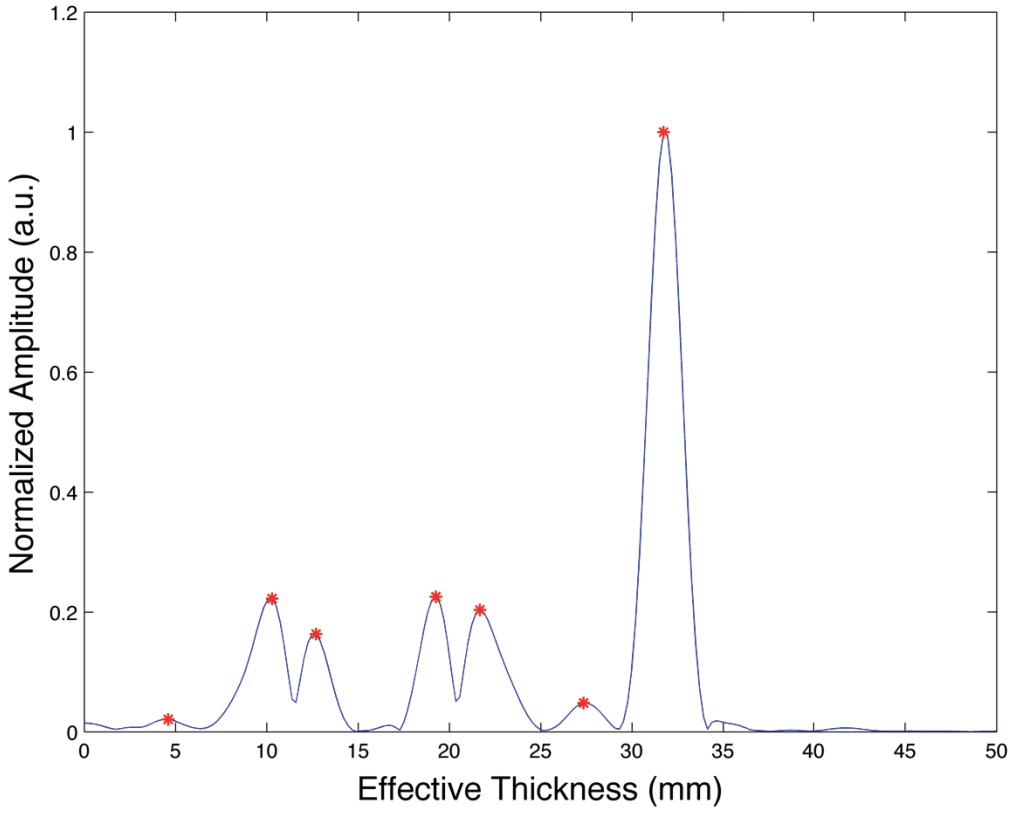

Figure 60 – Quintuple Layer "Unknown_1"; Measured Indoors in Reflection at Angle of Incidence of 0^{o}.

Table 9 – Quintuple Layer "Unknown_1" Peak Position Explanations; Measured Indoors in Reflection at Angle of Incidence 0°.				
Actual Thickness (mm)	Peak Position (mm)	Measured Thickness (mm)	Refractive Index	Symbol
3.00	4.595	3.063	1.5	*
6.50	10.28	6.853	1.5	*
8.00	12.69	8.46	1.5	*
12.5	19.26	12.84	1.5	*
14.5	21.66	14.44	1.5	*
17.5	27.35	18.233	1.5	*
20.5	31.84	21.23	1.5	*

5.2.7 Concluding Remarks on Indoor Results

The indoor measurements successfully proved that a tunable laser diode source could be used to characterize the individual layers of a multilayer sample. In addition to validating the MATLAB code used to detect the individual layers, the results from the samples measured also served as a baseline for the outdoor measurements that were to be performed.

One of the major takeaways from the indoor experiments is the difficulty in identifying all expected peaks for samples consisting of three or more layers. Combined with the resolution limitations of the experimental setup and the close relation between some of the layers' thicknesses, the presence of the numerous peaks complicated the peak identification process and this same difficulty will also be observed during the outdoor measurement results.

The results obtained for the samples provided by a third party also demonstrated the behaviour of heat and pressure treated samples. Due to the manufacturing process of these samples, the results showed how the interface between some of the layers was nullified to the point where the experimental results displayed these two layers as one. This is an important point to keep in mind since it can lead to falsely identifying the number of layers within the sample.

5.3 Outdoor Measurement Results

With the successful detection of multilayer samples in an indoor environment measuring both specular and diffuse reflection, the experimental setup was moved to the COPL's third floor remote sensing laboratory. As outlined in Chapter 4, the experimental setup was connected to the telescope and detection subsystem already optimized for the outdoor measurements at a distance of 170m. The outdoor measurements were performed from the 15^{th} to the 25^{th} of October 2013 during the days with promising weather. In order to have the most optimal testing conditions, all efforts were made in those two weeks to perform the measurements during sunny days with no possibility of rain.

Each sample was measured at the angles of incidence outlined in Table 3 in the outdoors measurement programme. The samples were placed in the mounting assembly and installed on the precision rotation mount. The initial alignment was accomplished by ensuring that, while standing on a predetermined spot on the roof, one's face fell within the sample's edges while looking at his reflection on the sample. This marked spot was determined prior to performing the outdoor experiments by having an individual stand on the roof and be guided to the point where its head covered the sample as seen on the IR camera monitor. Once the sample was mounted and the laser turned on, minute adjustments were made using the rotation mount and the telescope alignment based on the light reflections seen on the IR camera monitor.

To ensure the experimental setup alignment was not changed from day to day, in particular the 45^{o} mirror directing the light from the beam expander to the telescope, a frequency comb input was used. Viewing the returned light from one of the retro-reflective squares on the oscilloscope, optimal alignment was achieved by slightly adjusting the mirror position until the intensity was maximized. Rather than use the signal from the laser diode, the frequency comb was chosen to ensure proper alignment since it was simpler to visualize and maximize the amplitude of the combs on the oscilloscope. This simple process at the start of each day's experiments ensured the experimental setup was properly aligned with the desired target.

All the results presented are identified by their measured angle of incidence. For clarification purposes, 0^{o} represents measurements in reflection and the detection of the specular reflections. All other angles of incidences, such as 1^{o}, 5^{o} etc., represent the

measurements in transmission with a piece of paper acting as a diffuse reflector located behind the sample, unless stated otherwise. The measurements performed in transmission imply that the diffuse reflections off the piece of paper were being detected.

For each of the samples, general observations on the peaks detected on the figure are presented, followed by a discussion on any experimental anomalies that arose during testing. The results from the measurements performed at the additional angles of incidence are also discussed.

5.3.1 Single – BK7 3.184mm

As per the outdoors measurement programme, a single layer of 3.184mm BK7 was measured in transmission from 1^o to 30^o with a piece of paper acting as a diffuse reflector placed in behind the sample. Figure 61 represents the measurements performed at angles of 1^o, 10^o, 20^o and 30^o. A zoom on the main peak is shown in Figure 62. There are several key takeaways from the following figures. The first observation is that as the angle of incidence increases, the sample appears thinner. The fact that the sample appeared thinner was to be expected and can be confirmed through Eq. (28) as the cosine of the angle. Measuring the sample at 5^o resulted in a measured thickness of 3.208mm while a 20^o measurement yielded a thickness of 3.062mm. Table 10 provides the results of the 20^o angle of incidence measurement.

The second observation is the amplitude of the measured peak, which decreases as a result of the shear. As explained in Section 3.7, Off Axis Effect, the modulation efficiency of the interference is inversely proportional to the angle of incidence.

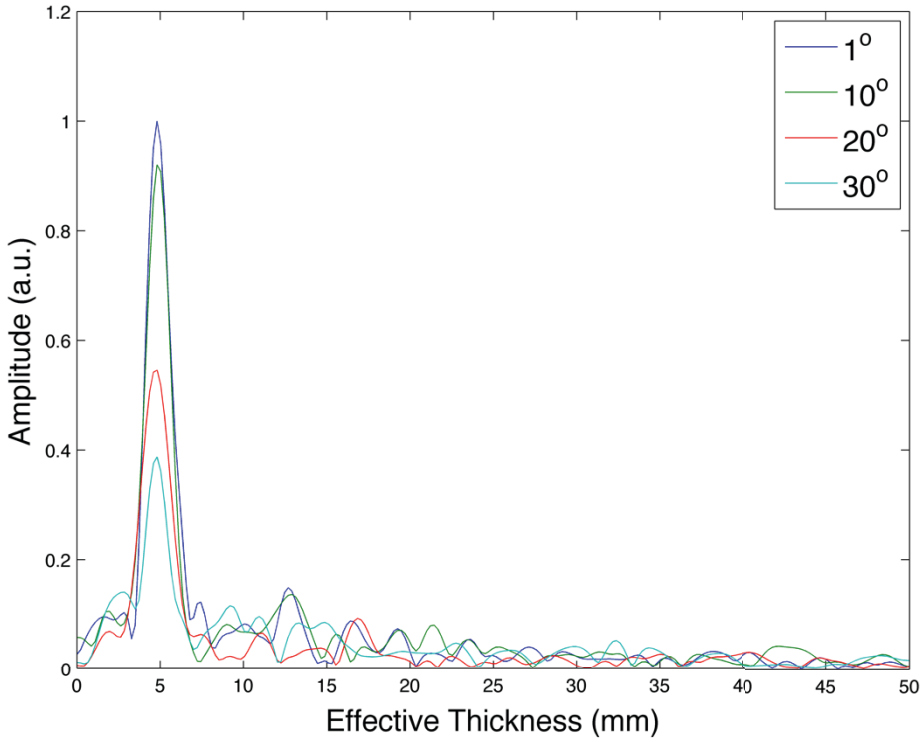

Figure 61 – Single Layer BK7 (3.184mm); Measured Outdoors in Transmission at Angle of Incidence of 1° to 30°.

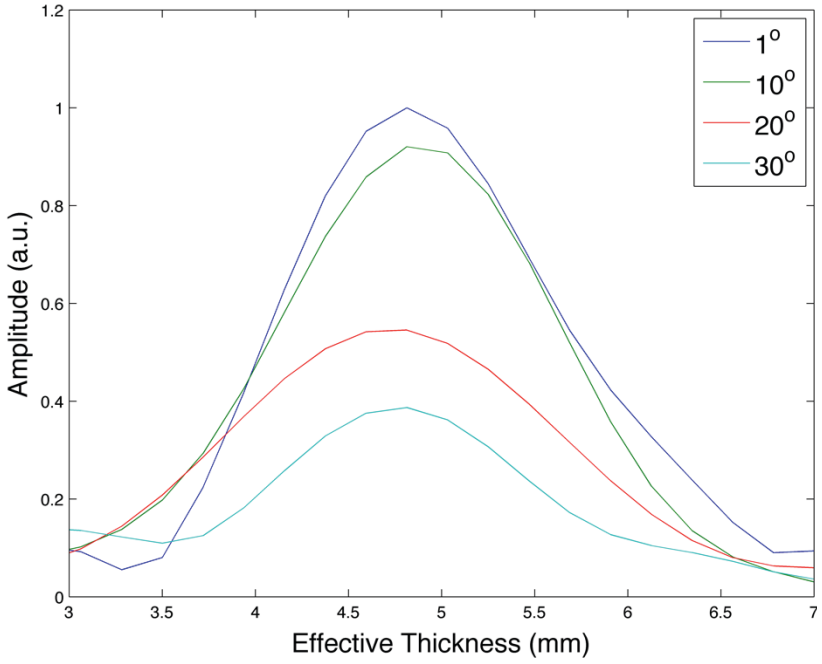

Figure 62 – Zoom on Main Peak of Single Layer BK7 (3.184mm); Measured Outdoors in Transmission at Angle of Incidence of 5° – 30°.

Table 10 – Single Layer BK7 (3.184mm) Peak Position Explanations; Measured Outdoors in Transmission at Angle of Incidence of 20°.			
Actual Thickness (mm)	Peak Position (mm)	Measured Thickness (mm)	Refractive Index
3.184	4.595	3.062	1.5005

These measurements validated the theory presented with regards to the relationship between the angle of incidence, the beam divergence and the modulation efficiency of the interference. The calculations on the limitations of the angle of incidence for this experimental setup, presented in Chapter 4, were also validated. Figure 63 provides the expected and measured normalized amplitudes for the single layer of BK7 as a function of the angle of incidence. The expected amplitudes were calculated using the modulation efficiency formula provided in Chapter 3, while the measured amplitudes were normalized with respect to the maximum amplitude of the peak for 1° angle of incidence. One important observation is how the measured normalized amplitude is below 0.6 for the angles of incidence greater than 15° while still yielding successful detection of the sample's thickness. This implies that the sample's thickness was still capable of being detected even with the modulation efficiency below 60%.

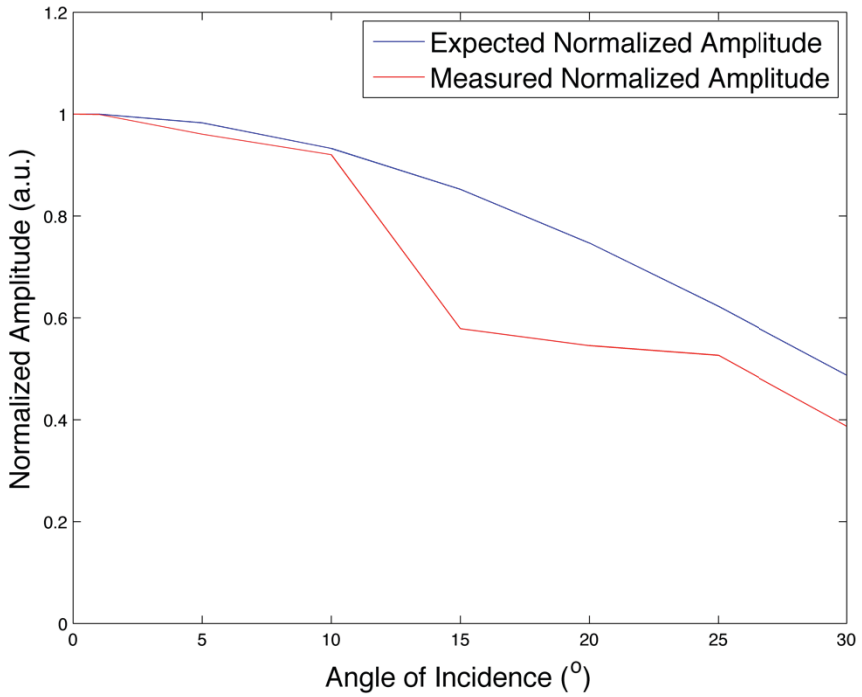

Figure 63 – Expected and Measured Normalized Amplitudes of Single Layer BK7 as a function of the Angle of Incidence.

5.3.2 Single – BK7 3.184mm – Alternative Diffuse Reflectors

The detection of a single layer of BK7 measuring 3.184mm performed in transmission at 1° angle of incidence with a dark-colored cotton fabric replacing the piece of paper is shown in Figure 64 and Table 11. The successful detection of the sample thickness, resulting in a measured thickness of 3.254mm, demonstrates that a sample's thickness can be retrieved with a diffuse reflector having a lower diffuse reflection coefficient.

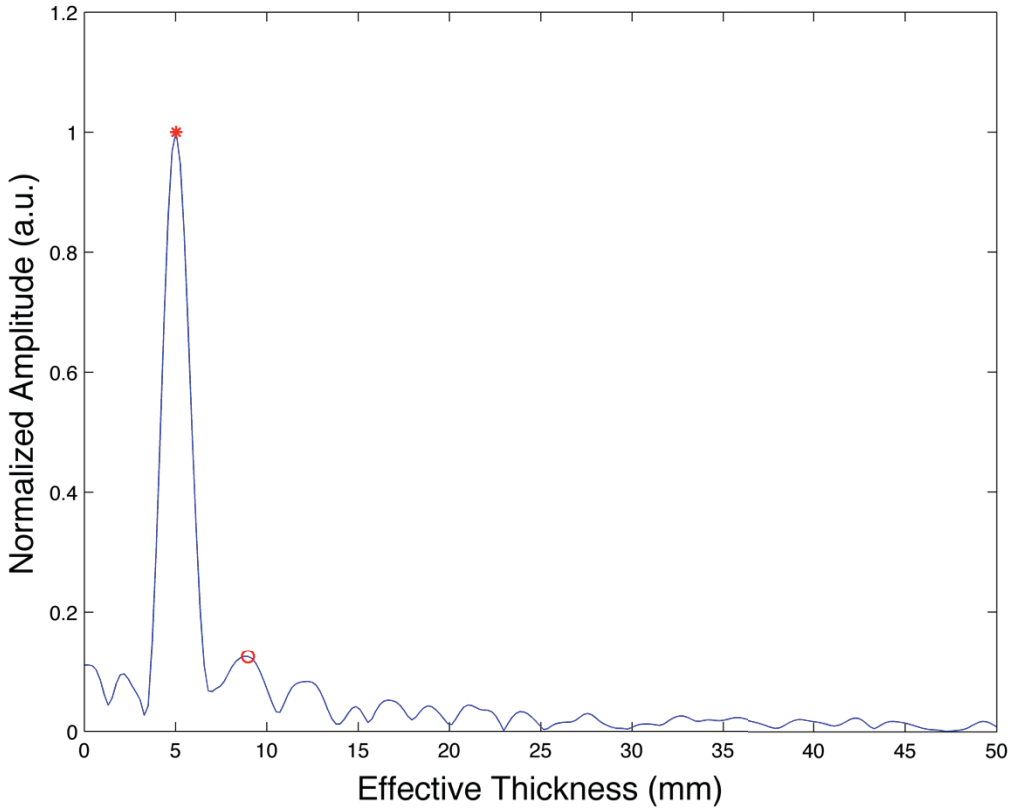

Figure 64 – Single Layer BK7 (3.184mm); Measured Outdoors in Transmission at Angle of Incidence of 1° with Cotton Sample.

Table 11 – Single Layer BK7 (3.184mm) Peak Position Explanations; Measured Outdoors in Transmission at Angle of Incidence of 1° with Cotton Sample.				
Actual Thickness (mm)	Peak Position (mm)	Measured Thickness (mm)	Refractive Index	Symbol
3.184	5.033	3.254	1.5005	*
6.368 (2nd harm of 3.184)	9.19	6.125	1.5005	o

Measurements were also performed at 5° angle of incidence with the cotton sample acting as a diffuse reflector. The results, similar to those at 1° angle of incidence, provided further confirmation that a cotton sample could indeed return enough light for the layer thickness to be detected. In addition to the cotton sample, a nylon sample of the same color was also used as a diffuse reflector. The measurements, performed at both 1° and 5° angle of incidence, returned near identical results to those performed with the cotton sample.

The measurements taken with fabric samples acting as diffuse reflectors provided optimism that if such an experimental setup were to be field deployed, the detection of a sample could be performed with any suitable lambertian diffuser and not necessarily a flat and cooperative surface. While not performed during these experiments, it would be worthwhile in future experiments to verify if using a fabric sample as a diffuse reflector could provide similar positive results for a multilayer sample.

5.3.3 Single – Acrylic 1.88mm

Figure 65 and Table 12 represent the detection of a single layer of acrylic measuring 1.88mm performed in transmission at an angle of incidence of 10°. As can be seen in Table 12, the main peak on the figure can be associated to a measured thickness of 1.922mm. The second and third harmonics of the layer's thickness are identified, but several spurious spikes are also present.

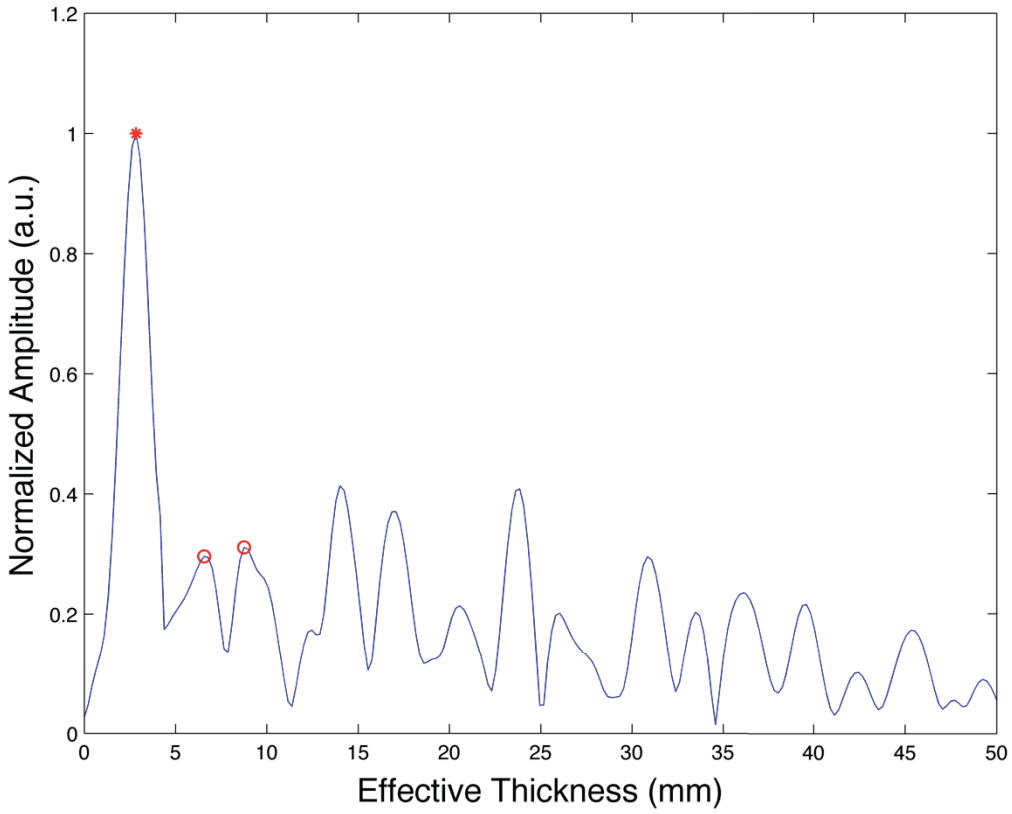

Figure 65 – Single Layer Acrylic (1.88mm); Measured Outdoors in Transmission at Angle of Incidence of 10°.

Table 12 – Single Layer Acrylic (1.88mm) Peak Position Explanations; Measured Outdoors in Transmission at Angle of Incidence of 10°.				
Actual Thickness (mm)	Peak Position (mm)	Measured Thickness (mm)	Refractive Index	Symbol
1.88	2.845	1.922	1.48	*
3.76 (2nd harm of 1.88)	6.320	4.27	1.48	o
5.64 (3rd harm of 1.88)	8.753	5.914	1.48	o

Measurements for this sample were also performed for angles of incidence from 0° to 35° in order to further validate the theory concerning the limitations on the angle of incidence. The results, however, were not as successful as those performed for the BK7 sample. While the results for the measurements performed under 15° provided positive results, it became difficult to extract the sample thickness for the larger incidence angles. As will be seen in subsequent results, discussed below, this layer proved to be difficult to measure when combined with other layers.

While the results were successful for the angle progression measurements of the BK7 sample, the acrylic samples provided some difficulty when it came to measuring at large angles. One explanation for the difficulty in detecting the acrylic sample in comparison to the BK7 sample is the difference in transmittance of both materials at the lasing wavelength. At the central wavelength of 1562nm used for this experimental setup, the acrylic sample, also known as poly (methyl methacrylate) (PMMA), has a transmittance of approximately 85% for a 2mm thick sample. As the sample's thickness increases, the transmittance decreases, going as low as 60% for a 20mm sample. In comparison, the BK7 has a transmittance of nearly 95% at the same wavelength [57]. Figures 65 and 66 provide a visual representation of the transmission spectrum for both materials.

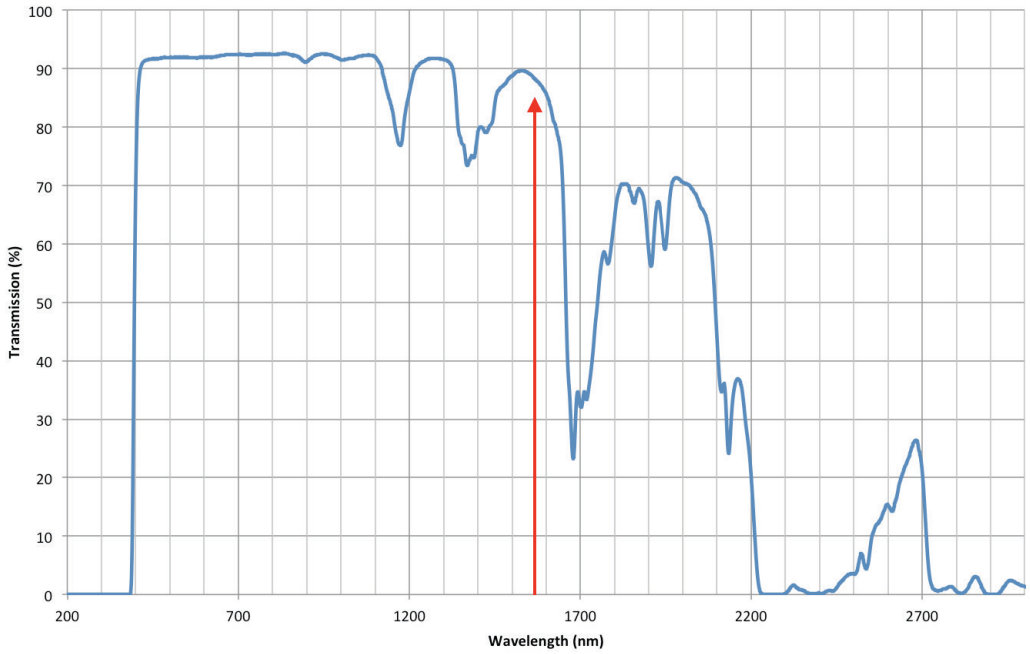

Figure 66 – Acrylic Substrate Transmission for 2mm Sample, from [57].

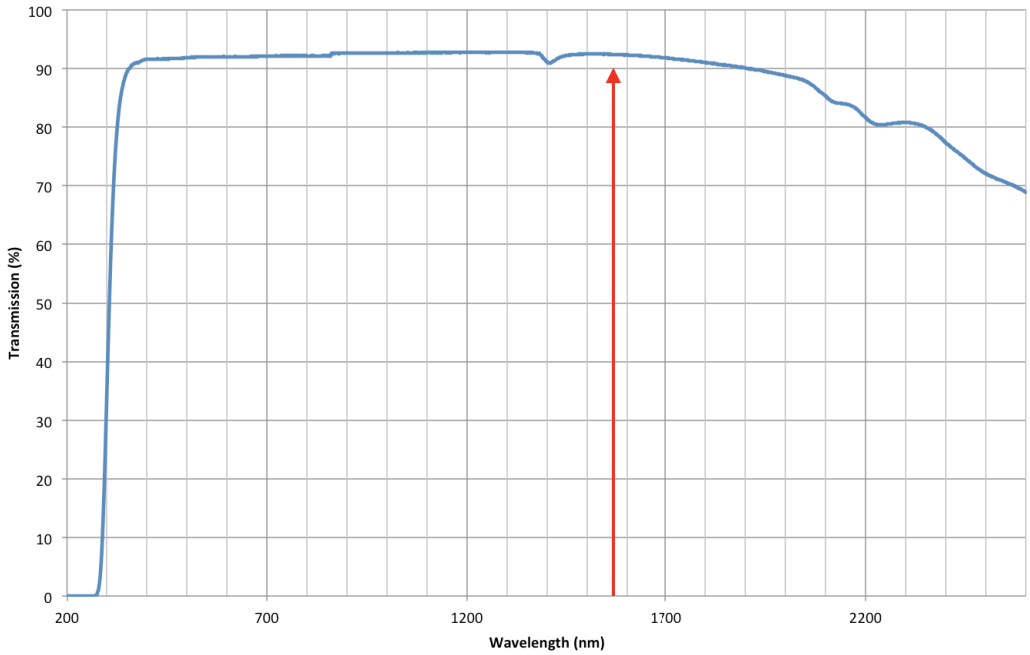

Figure 67 – BK7 Substrate Transmission for 10mm Sample, from [57].

In addition, the contrast in surface quality between the acrylic and BK7 also contributed to the difference in detecting both materials. With the acrylic sample's surface quality being considered inferior to that of the BK7, this implies that the interferometric modulation can be averaged out over the beam size. Surface quality measurements of the samples are underway to validate this hypothesis. The combination of the lower transmittance and inferior surface quality of the acrylic sample explains why the angle progression measurements weren't as successful as those performed with the BK7 sample.

5.3.4 Double – Acrylic 6.12mm & BK7 3.184mm

Figure 68 and Table 13 represent the detection in reflection at 0^{o} angle of incidence of a double layer sample of acrylic and BK7, measuring 6.12mm and 3.184mm respectively. The sample is mounted so that the acrylic layer is located closest to the launcher. As can be seen on the figure below, the individual layer thicknesses are well identified and result in very precise measurements.

The total thickness's peak is identifiable but its amplitude is lower compared to the other two main peaks. Alignment of the individual layers could have been an issue when detecting the specular reflection since the interfaces need to be perfectly parallel to yield successful results. The interfaces generating the total thickness peak could be slightly

offset with respect to each other, which could cause the low amplitude peak. The difference in surface quality between the acrylic and BK7 could also have been a contributing factor for the lower amplitude.

Measurements were also performed at 1° and 5° angle of incidence, yielding similar results. The total thickness peak's amplitude was consistently smaller compared to the other two peaks.

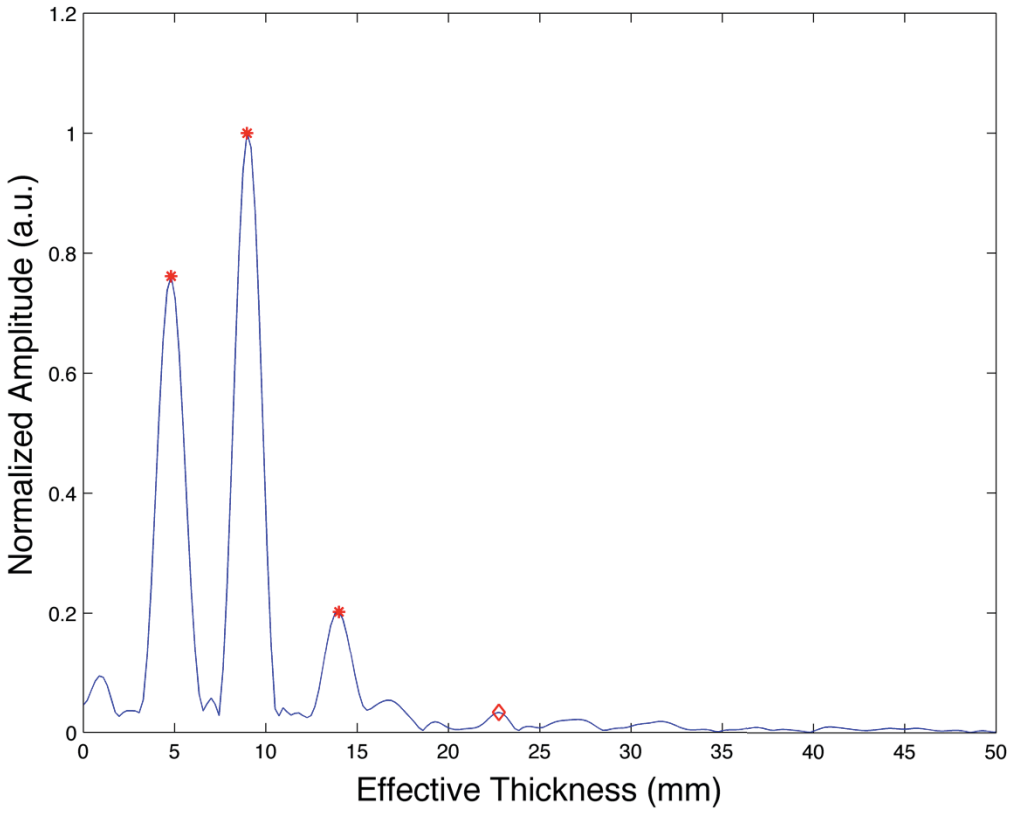

Figure 68 – Double Layer Acrylic (6.12mm) & BK7 (3.184mm); Measured Outdoors in Reflection at Angle of Incidence of 0°.

Table 13 – Double Layer Acrylic (6.12mm) & BK7 (3.184mm) Peak Position Explanations; Measured Outdoors in Reflection at Angle of Incidence of 0°.				
Actual Thickness (mm)	Peak Position (mm)	Measured Thickness (mm)	Refractive Index	Symbol
3.184	4.814	3.208	1.5005	*
6.12	9.081	6.136	1.48	*
9.304	13.79	9.274	1.487	*
15.424 (6.12+9.304)	22.76	15.337	1.484	◇

5.3.5 Double – Acrylic 6.12mm & 2.19mm

The measurement of a double layer of acrylic measuring 6.12mm and 2.19mm respectively, and performed in transmission at 10° angle of incidence, is shown in Figure 69 and Table 14. Noise appears to have a more significant impact for these measurements and this could be due the presence of raindrops during some of the final measurements. All efforts were made to avoid measurements during this weather; however, it proved to be unavoidable during this day's experiments.

The peak located at 5.689mm effective thickness is believed to be a spurious peak originating from an external source. This same peak was observed for all of this sample's measurements, and was also present during measurements of the triple layer of acrylic, as well as the "P411" and "P427" samples. These samples were measured one after the other during a two-day span of the outdoors measurement campaign. The presence of this same peak for numerous samples of different layer thicknesses leads to believe that it is a spurious peak most likely coming from a parasitic reflection somewhere in the setup. During the indoor measurement in reflection of this double layer acrylic sample, this spurious peak was not observed. In addition, the fact that the peak located at 14.55mm effective thickness is a combination of this spurious peak and one of the layers measured (8.971mm effective thickness) further validates that this spurious peak originated from an unwanted reflection.

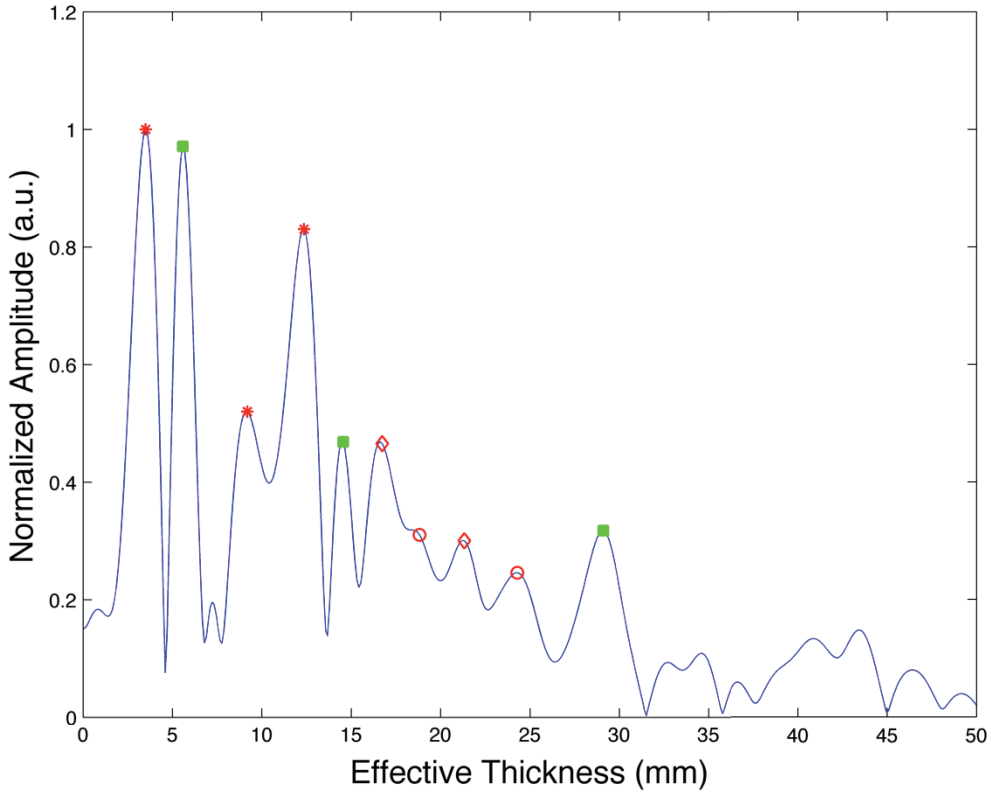

Figure 69 – Double Layer Acrylic (2.19mm & 6.12mm); Measured Outdoors in Transmission at Angle of Incidence of 10°.

Table 14 – Double Layer Acrylic (2.19mm & 6.12mm) Peak Position Explanations; Measured Outdoors in Transmission at Angle of Incidence of 10°.				
Actual Thickness (mm)	Peak Position (mm)	Measured Thickness (mm)	Refractive Index	Symbol
2.19	3.282	2.218	1.48	*
Unknown	5.689	3.844	1.48	■
6.12	8.971	6.061	1.48	*
8.31	12.691	8.575	1.48	*
Unknown	14.55 (5.689+8.971)	9.831	1.48	■
10.5 (2.19+8.31)	16.62	11.230	1.48	◇
12.24 (2nd harm of 6.12)	18.60	12.568	1.48	O
14.43 (6.12+8.31)	21.33	14.412	1.48	◇
16.62 (2nd harm of 8.31)	24.40	16.486	1.48	O
Unknown	29.21 (2nd harm of 14.55)	19.736	1.48	■

This sample was also measured at angles up to and including 15°, with similar results being obtained for all angles. In each case, the spurious peak at 5.689mm was present and had one of the highest amplitudes.

5.3.6 Triple – Acrylic 6.12mm, BK7 3.184mm & Acrylic 1.88mm

The results of the measurement in transmission at 1° angle of incidence of a triple layer sample of acrylic and BK7 are presented in Figure 70 and Table 15. The BK7 layer, measuring 3.184mm, is placed in between the acrylic layers of 1.88mm and 6.12mm, with the 6.12mm layer placed closest to the launcher. From the table and figure below, one can see that five of the six expected peaks are identified, with the thin layer of 1.88mm being the only one unidentified.

The two peaks with the higher amplitudes are associated with the BK7 layer. The first is the individual layer's thickness and the other is the BK7's combination with the 6.12mm layer of acrylic. The difference in surface quality between the BK7 and the acrylic may explain why these layer combinations produced higher peak amplitudes compared to the individual acrylic layers and the total sample thickness.

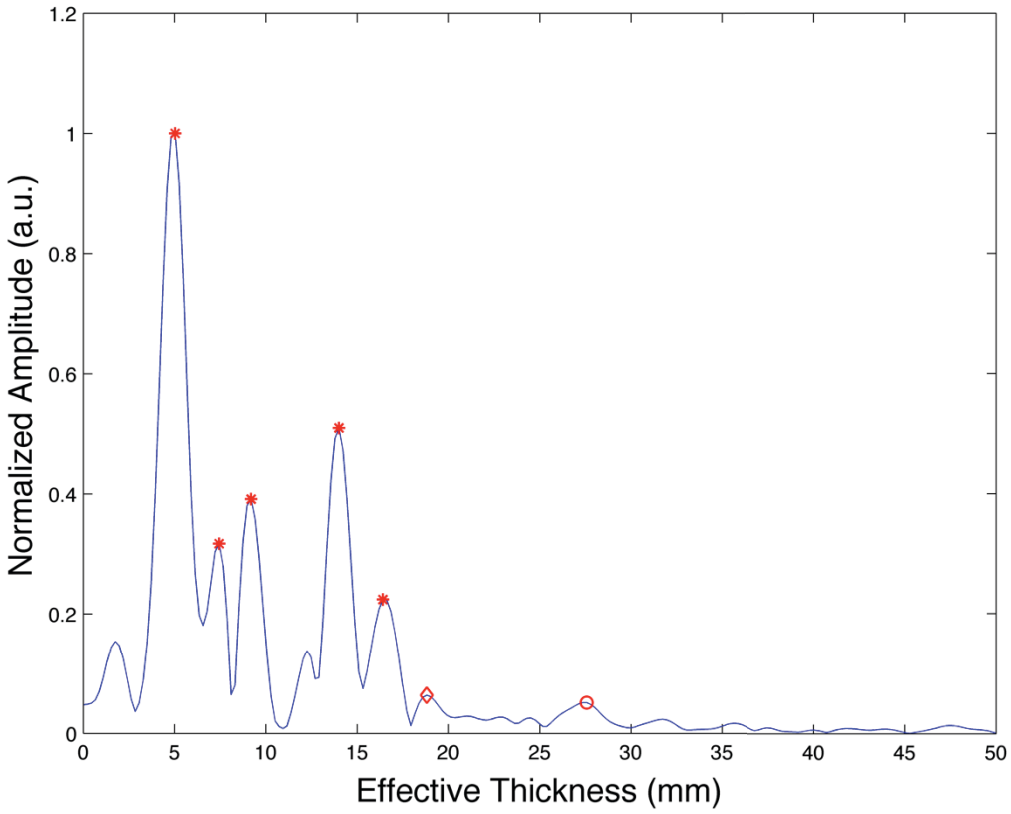

Figure 70 - Triple Layer Acrylic (6.12mm), BK7 (3.184mm) & Acrylic (1.88mm); Measured Outdoors in Transmission at Angle of Incidence of 1°.

Table 15 – Triple Layer Acrylic (6.12mm), BK7 (3.184mm) & Acrylic (1.88mm) Peak Position Explanations; Measured Outdoors in Transmission at Angle of Incidence of 1°.				
Actual Thickness (mm)	Peak Position (mm)	Measured Thickness (mm)	Refractive Index	Symbol
3.184	5.033	3.354	1.5005	*
5.064	7.44	4.983	1.493	*
6.12	9.19	6.061	1.48	*
9.304	14.0	9.418	1.487	*
11.184	16.41	11.043	1.486	*
12.488 (3.184+9.304)	18.82	12.631	1.49	◇
18.608 (2nd harm of 9.304)	27.57	18.541	1.487	O

This sample was also measured at 0^o and 5^o angle of incidence. At 0^o, similar results were observed. The peaks corresponding to the 1.88mm layer and its combination with the other layers proved difficult to extract. When measuring the sample at 5^o, the BK7 layer was the only peak that was easily identifiable. Peaks for the 6.12mm layer of acrylic and its combination with the BK7 layer were present but had relatively low amplitudes. The only peak associated with the 1.88mm layer that was identifiable on the figure was when it was combined with the BK7 layer.

An important point to highlight from these experiments is that for samples with three or more layers, it becomes increasingly difficult to be able to successfully identify all individual layers and their combinations. Without knowing the specifications of the sample under test, one would be hard pressed to successfully identify all layers. This will be further observed in the following sub-sections providing results for other three and four layer samples.

5.3.7 Quadruple – Acrylic 2.19mm, 6.12mm, 1.88mm & 2.947mm

Figure 71 and Table 16 represent the detection of a four layer acrylic sample measured in transmission at 5^o angle of incidence. The layers are placed in the following order, starting with the layer located closest to the launcher: 2.19mm, 6.12mm, 1.88mm and 2.947mm. The missing primary peaks can be explained by the 0.80mm resolution limitations of the experimental setup. As such, the 1.88mm is undetected in comparison to the 2.19mm layer. The same applies for the 8.00mm combination in comparison to the 8.31mm combination.

The additional peaks that have been identified in the figure and table below correspond to the sum of two layer combinations or, the second harmonics of an individual layer or a layer combination. This is an important finding as it demonstrates how a layer's second harmonic can influence the results and complicate the detection process. As with the results obtained for a three-layer sample, it becomes increasingly difficult to extract all individual layers and their combinations for a four-layer sample. This is particularly true when the sample's individual layers are closely related to one another and nearly every peak observed on the figure can be associated to a layer combination.

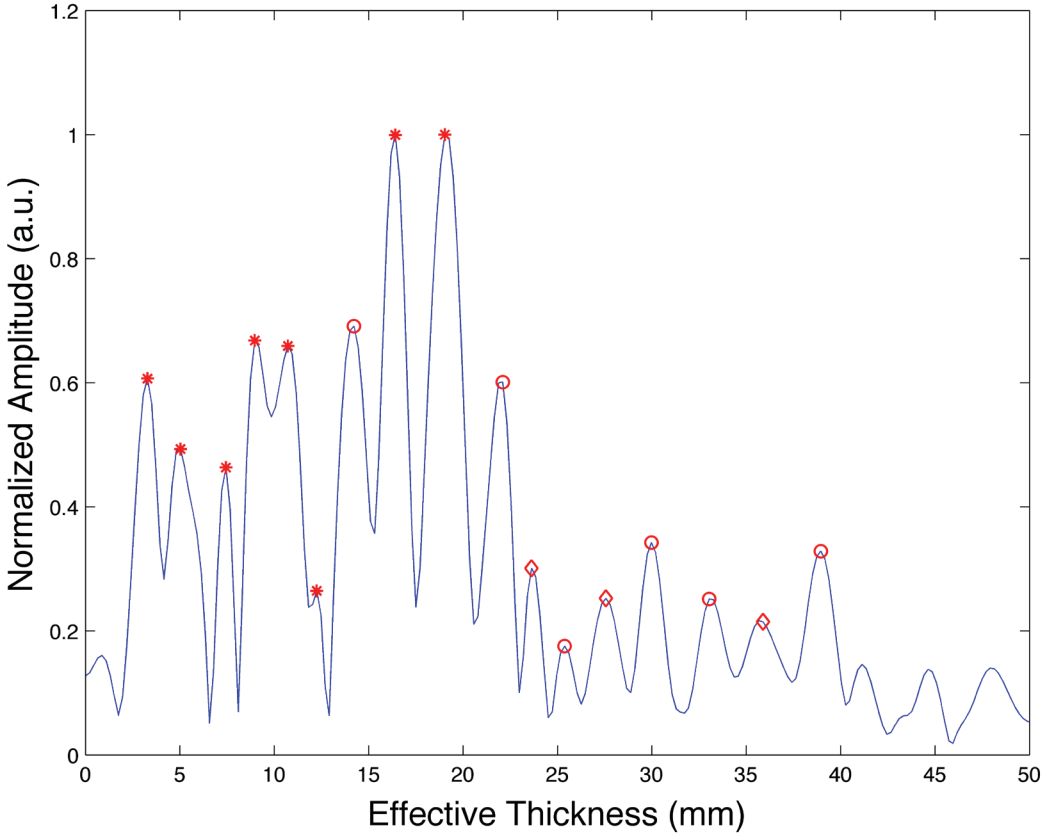

Figure 71 – Quadruple Layer Acrylic (1.88mm, 2.19mm, 2.947mm & 6.12mm); Measured Outdoors in Transmission at Angle of Incidence of 5^{o}.

Table 16 – Quadruple Layer Acrylic (1.88mm, 2.19mm, 2.947mm & 6.12mm) Peak Position Explanations; Measured Outdoors in Transmission at Angle of Incidence of 5°.				
Actual Thickness (mm)	Peak Position (mm)	Measured Thickness (mm)	Refractive Index	Symbol
2.19	3.282	2.218	1.48	*
2.947	4.814	3.105	1.48	*
4.827	7.44	5.027	1.48	*
6.12	8.971	5.914	1.48	*
8.00	10.72	7.243	1.48	*
8.31	12.25	8.277	1.48	*
9.654 (2nd harm of 4.827)	14.22	9.166	1.48	O
10.947	16.41	11.088	1.48	*
13.137	19.26	13.014	1.48	*
16.00 (2nd harm of 8.00)	22.10	14.933	1.48	O
16.31 (8.00+8.31)	23.63	15.820	1.48	◇
16.62 (2nd harm of 8.31)	25.38	17.149	1.48	O
19.257 (8.0+10.947)	27.57	18.628	1.48	◇
20.38 (2nd harm of 10.19)	29.98	20.257	1.48	O
21.894 (2nd harm of 10.947)	33.04	22.324	1.48	O
24.084 (10.947+13.137)	35.89	24.25	1.48	◇
26.274 (2nd harm of 13.137)	38.95	26.318	1.48	O

Comparable results were obtained when this sample was measured at angles of 0° and 1°. In both cases, a large majority of the peaks present on the figure could be associated to either one of the layers, layer combinations or layer harmonics.

5.3.8 Triple – "P411"

Figure 72 and Table 17 represent the detection of the sample labeled "P411" measured in transmission at 6° angle of incidence. This is a three-layer laminated sample with a layer of 1.8mm placed in between layers of 10.4mm and 15.0mm. For these measurements, the 10.4mm layer was placed closest to the launcher. Similar to the measurements performed in the laboratory for this sample, the first two layers (1.8mm and 10.4mm) appear as one single layer on the figure. This was to be expected from the laboratory measurement results. The "P411" sample is considered a true laminated sample with heat and pressure treatments, and it was therefore perfectly reasonable to expect the interface between the two layers to be essentially nullified.

The total thickness, however, is neither detected at this angle of incidence nor was it detected at angles of 1° and 3°. Even using the known theory and adding the two main peaks to obtain an idea of the expected total thickness doesn't yield better results. The reason for the inability to detect the total thickness could be attributed to a lack of optical power or the composition of the sample's material, which greatly attenuates the incoming light. Another possibility for the unsuccessful detection of the total thickness could be the surface quality of the sample, which can average out the interferometric modulation. As predicted by the calculations on the limitations of the angle of incidence, measurements performed at 10° angle of incidence were unsuccessful. This was to be expected since, at 10° angle of incidence, the modulation efficiency was calculated to be 28% for the 12.2mm combination layer and 8% for the 15.0mm layer.

While it is possible that the first peak, located at 5.689mm effective thickness, could be associated to the second harmonic of the thin layer of 1.8mm, it is believed that this peak is actually the spurious peak previously discussed since it was not detected during this sample's indoor measurement. This same peak was also observed for the measurements performed at 1° and 3° angle of incidence, and was present during measurements other samples as discussed above. The presence of this same peak for numerous samples of different layer thicknesses leads to believe that it is a spurious peak generated from an external source rather than the second harmonic of the thin layer.

This sample, as well as the "P427" sample, proved to be much more difficult to achieve initial alignment compared to the samples manufactured in house at the university. The task of achieving 0° angle of incidence took much longer than the previous samples

and was likely caused by surface quality of the sample. As previously stated, initial alignment was achieved by standing on a marked spot on the roof and ensuring that one's face fell within the sample's edges while looking at their reflection on the sample. The trouble of achieving the initial alignment could have led to the difficulty in detecting all layers of the sample.

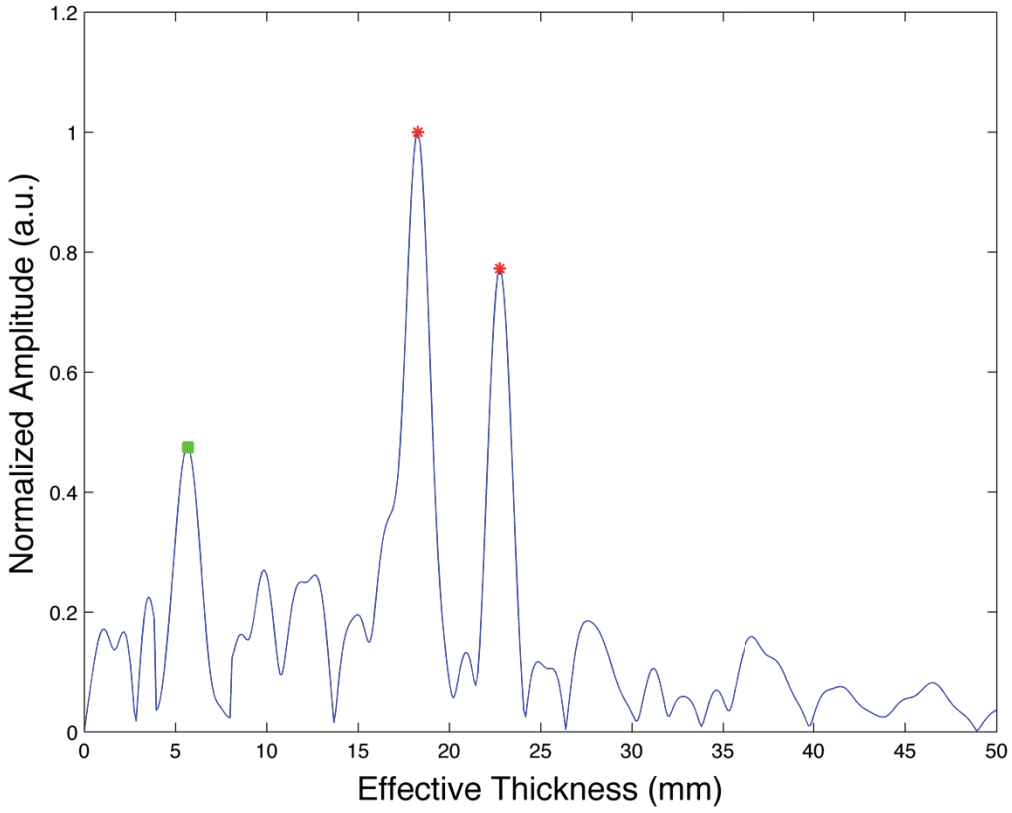

Figure 72 – Triple Layer "P411"; Measured Outdoors in Transmission at Angle of Incidence of 6°.

Table 17 – Triple Layer "P411" Peak Position Explanations; Measured Outdoors in Transmission at Angle of Incidence of 6°.				
Actual Thickness (mm)	Peak Position (mm)	Measured Thickness (mm)	Refractive Index	Symbol
Unknown	5.689	3.793	1.5	■
12.2	18.16	12.11	1.5	*
15	22.76	15.17	1.5	*

5.3.9 Triple – “P427”

The detection of the sample labeled “P427” measured in transmission at 3° angle of incidence is shown in Figure 73 and Table 18. This is also a true laminated sample with a 2.5mm layer placed in between 12.8mm and 15.9mm layers. For these measurements, the 15.9mm layer is placed closest to the launcher. Five of the six expected peaks are identified on the figure below. The only unidentified peak is 15.3mm; the sum of the final two layers measuring 2.5mm and 12.8mm. The inability to identify this peak can be attributed to the resolution of the system.

In addition, like the measurements of the “P411” sample, a peak was identified at 5.689mm effective thickness. This peak cannot correspond to the second harmonic of the thin layer, which means it can only be the spurious peak originating from an external source.

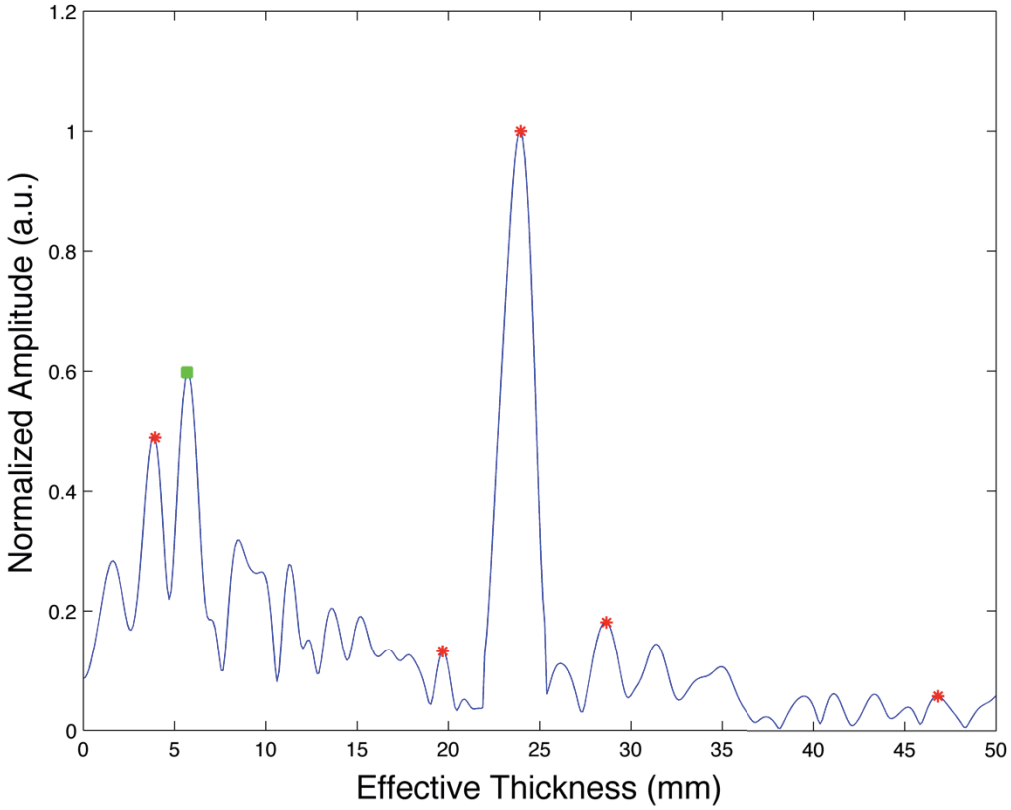

Figure 73 – Triple Layer “P427”; Measured Outdoors in Transmission at Angle of Incidence of 3°.

Table 18 – Triple Layer "P427" Peak Position Explanations; Measured Outdoors in Transmission at Angle of Incidence of 3°.				
Actual Thickness (mm)	Peak Position (mm)	Measured Thickness (mm)	Refractive Index	Symbol
2.50	3.282	2.188	1.5	*
Unknown	5.689	3.793	1.5	■
12.8	19.69	13.127	1.5	*
15.9	23.96	15.973	1.5	*
18.4	28.56	19.04	1.5	*
31.2	46.83	31.22	1.5	*

This sample was also measured at angles of 0°, 1°, 6° and 10°. Comparable results were achieved for the 0° and 1° measurement while the 6° measurement only yielded a peak for the 15.9mm layer, situated closest to the launcher. The 10° measurement returned no useful results, which was to be expected based on the angle of incidence limitations of the experimental setup. At this angle of incidence, the modulation efficiency calculated for the 12.8mm layer was 23% while the 15.9mm layer returned a modulation efficiency of less than 1%.

5.3.10 Concluding Remarks on Outdoor Results

The outdoor measurements successfully proved that the individual layers of a multilayer sample were capable of being retrieved at a distance of 170m, and this at multiple angles of incidence. The calculated limitations of the experimental setup on the angle of incidence were not fully validated. That being said, the angle progression measurements of the single layer of BK7 were successful and stayed true to the theory, while the acrylic layers proved to be more of a challenge. During the angle progression measurements of the single layer of BK7, the results reflected how as the angle of incidence increased, the sample appeared thinner and the peak's amplitude diminished due to the decrease in the modulation efficiency.

The difference in surface quality between the acrylic and BK7 material is an important observation that can be made from the results. The BK7 material, with a higher quality polished surface, continually generated more promising results compared to the acrylic material. Even when combined with the acrylic layers, the BK7 layer's peak stood out from the rest, in addition to its combinations with the other layers. The surface quality

of the sample being measured is an important factor to take into consideration when performing such measurements. Furthermore, the acrylic material also had a lower transmittance than the BK7 at the operating wavelength of the experimental setup. The selection of the proper wavelength to improve the chances of detection is also extremely critical.

The use of a cotton and nylon sample successfully demonstrated the application of alternative diffuse reflectors. Replacing the piece of paper located behind the sample, the fabric samples, acting as diffuse reflectors, still enabled to extraction of the sample's thickness. This is an extremely interesting finding that demonstrates the possibility of detecting a sample with any suitable lambertian diffuser.

Another observation is the difficulty in extracting all expected peaks when the sample was three or more layers. The increase in the number of peaks, combined with the noise present and the appearance of second harmonics, provided an extra degree of difficulty in determining all individual layers. The close proximity of some of the expected peaks with relation to each other also added complexity to the detection process and these peaks were not always resolved. Knowing the material and the expected peak positions prior to the measurements simplified the peak detection process, but this may not always be the case. For the measurement of two-layer samples, the peak positions of the two individual layers could be added to determine the sample's total thickness when it wasn't positively identified. The combination of the resolution of the experimental setup and the large number of peaks present for three or more layers greatly limited the successful identification of the thickness of the individual layers. This would prove to be an even greater challenge in the field deployment of such a setup, and the user has no knowledge of the sample under test.

The samples provided by the third party demonstrated interesting, yet predictable, results. The measurement results demonstrated how the interface between two individual layers was essentially nullified due to the manufacturing process with heat and pressure treatments. This led to two layers being identified as one during the peak identification process, and a false identification of the number of individual layers within the sample. Similar results were observed when these samples were measured using the frequency combs setup [3].

Finally, the weather did play a role in the detection process. While all efforts were made to perform the measurements during sunny days with no possibility of rain, such efforts were not always accomplished due to weather's unpredictability. As was seen with the measurement of the double layer of acrylic measuring 2.19mm and 6.12mm, even the presence of light raindrops increased the noise level and the difficulty in successfully detecting the individual layer thicknesses.

5.4 Areas for Improvement

While the current experimental setup was successful in determining the individual layers of a multilayer sample at a distance of 170m, limitations were still present and could be modified to improve the results.

In a 2013 ABB report, Raphaël Desbiens presented the development of a retrieval algorithm for a stratified medium [50]. It was stipulated that more than just the thickness of the medium could be retrieved using the same interferometry techniques adapted for this thesis. In addition to the effective optical thickness, information such as the refractive index, the angle of incidence, the ordering of the layers and the polarization angle could also be retrieved. The key to simultaneously retrieving all this information was performing multiple measurements at different but known polarization angles (three being optimal). Implementing the measurement of the multilayer sample with three distinct polarization states would be a slightly more complex experimental setup but would help eliminate the degeneracy of the information and improve the results. Furthermore, his retrieval algorithm demonstrated the ability to determine a stratified medium's characteristics through the application of a least-squares minimization, comparing the measurements obtained to a simulation model. A similar retrieval algorithm would need to be implemented for the field deployment of such an instrument, thereby improving the chances of successfully identifying the thickness of all the individual layers.

Another avenue to explore would be to expand the tuning range of the laser. While the current laser diode was constantly being pushed to its maximum, a different tunable source could be implemented that would allow for a wider tuning range thus improving the spatial resolution of the setup. Thorlabs Inc. offers special types of laser diodes such as external-cavity laser diodes and distributed Bragg reflector lasers that are capable of being tuned over 40nm, all the while maintaining a very narrow line width of several hundred

kHz. The drawback of these types of lasers, however, is their high price and fragility compared to typical laser diodes.

A pre-amplifier is currently be used to collect the APD output, filter the background noise and amplify the signal prior to being sent to the oscilloscope. While the component is essential, it also provides its own noise that does slightly impact the results. Different methods could be adapted to achieve the same outcome while avoiding the additional noise. Digital filtering methods could be implemented during the analysis steps and a more efficient amplifier could be employed.

As previously stated, optimal alignment with the target will not always be achieved and as such, measurements will be performed at angles of incidence different than 0^{o}. It was observed that the beam divergence did limit the maximum achievable angle of incidence for successful measurements. Through the beam expander, the beam divergence could be reduced to allow for more precise measurements of a sample at greater angles of incidence.

Throughout the outdoor measurements, it was also observed how the change in temperature within the laboratory caused the laser's wavelength and interferometric paths to drift. This was to be expected since the fibres were exposed to the ambient air and the window of the remote sensing laboratory was open for launching. Thermally isolating the experimental setup, as much as possible, would protect the fibres from being exposed to these changes in temperature and assist in generating more consistent results.

Finally, the MATLAB code currently used to extract the thickness of the multilayer sample isn't fully autonomous. During the interpolation portion of the code, the user is required to manually select the start and end points of the unwrapped instantaneous phase that will be used to determine all jumps of 2π. Efforts are currently underway to modify the code to determine these points automatically and become fully independent. This would be an important step for a field-deployed setup where the user's ultimate goal is to obtain the thickness of the individual layers of the multilayer sample.

6 Conclusion

This thesis was able to demonstrate the development of an incoherent LADAR detection technique using a tunable laser diode source to identify and characterize multilayer samples with sub-mm resolution at long-range distances, accomplishing the goal set out at the beginning of this research process. Using readily available optical components and no additional money spent, a simple interferometry setup was designed and numerous multilayer sample measurements were accomplished. The experimental setup was designed utilizing the fundamental concepts of FTS, OCT and FMCW LADAR presented in Chapter 2.

The five main objectives outlined at the beginning of the thesis were accomplished. In addition to the number of layers of a sample, the thickness of the individual layers and the total thickness of the sample were detected. Furthermore, these measurements were performed in an outdoor environment at a distance of 170m and at multiple angles of incidence.

The multilayer samples, manufactured in house at Université Laval and provided by a third party, were composed of one to five individual layers with varying thicknesses. Each sample was measured at multiple angles of incidence to verify the performance capabilities and determine the limitations of the experimental setup.

The indoor experimental phase of this research proved vital to validate and calibrate the experimental setup and should be repeated in future experiments of this type. This indoor phase served as confirmation that with the aid of the Fourier transform, the light behaviour within a Fabry-Pérot etalon could be used to enable the extraction of the etalon's thickness. By considering a multilayer sample to be numerous Fabry-Pérot etalons stacked together, it was possible to successfully identify the individual layer thicknesses of the stratified medium. The difference in performing measurements in reflection and transmission was also confirmed during the indoor phase.

This thesis has shown that the technique of using a tunable laser diode works well for the identification of multilayer samples. Even when the specular reflection is not detected, the possibility to detect the sample at an angle still exists. One important factor to this achievement is the measurement in transmission, using a lambertian diffuser

behind the multilayer sample. The advantages of this approach have been demonstrated in this thesis.

While successful results were achieved for several of the samples under test, limitations were still observed. The primary being the difficulty in successfully identifying the individual thicknesses associated to samples with three or more layers. Without the knowledge of the expected results, the peak identification process proved to be a difficult endeavour because of the number of peaks present and their varying amplitudes. A more sophisticated retrieval algorithm would need to be implemented in order to successfully retrieve the unidentified interfaces.

One important observation that must be taken away from this thesis is the limitations on the angle of incidence due to beam shearing when detecting in transmission. Ensuring a small beam divergence, or even the implementation of dual beam launcher, could mitigate the angle limitation of this experimental setup. The second key observation is the high variability upon the sample itself. The surface quality was a key variable that greatly influenced the success of the measurements and was observed in the difficulty to detect the acrylic layers. This leads to believe that, while the technique show large promises, a study of the impact of the surface quality, along with beam size and divergence is required.

Even with such limitations, the results are nonetheless extremely positive and serve as a proof of concept that a simple interferometry setup with a tunable laser diode source is capable of being employed to characterize multilayer samples. Numerous steps must still be taken to improve the results and optimize this experimental setup for field deployment. Additionally, such a setup could be ultimately implemented for the benefit of a 3D imaging system.

References

[1] Boudreau S, Levasseur S, Perilla C, Potvin S, Genest J. *Spectral LADAR using frequency combs*. DRDC Valcartier Contractor Report 2012-TASK3.

[2] Genest J, Boudreau S, Levasseur S. *LIDAR, LADAR and passive remote sensing with optical frequency combs*. DRDC Valcartier Contractor Report 2012-TASK4.

[3] Genest J, Boudreau S, Deschênes JD, Levasseur S. *Long distance reflectometry – detection of complex refractive layers*. DRDC Valcartier Contractor Report 2012-TASK4.

[4] Chattopadhyay D, Rakshit P. *Electronics: fundamentals and applications*. New Delhi: New Age Publishers; 2006.

[5] Richmond R, Cain S. *Direct detection LADAR systems*. Bellingham, WA: SPIE Press; 2009.

[6] NASA. *The Apollo 15 Lunar Laser Ranging RetroReflector*. [Online] Available from: http://www.nasa.gov [Accessed 5 Feb 2014].

[7] Weitkamp C. *LIDAR: Range-resolved optical remote sensing of the atmosphere*. New York: Springer; 2005.

[8] Jones A, Brewer P, Johnsone E, Macklin M. High-resolution interpretative geomorphological mapping of river valley environments using airborne LIDAR data. *Earth Surf. Process. and Landforms*. 2007; 32 (10): 1574-1592.

[9] Mccoy M, Asner G, Graves M. Airborne lidar survey of irrigated agricultural landscapes: an application of the slope contrast method. *Journal of Archaeological Science*. 2011; 38 (9): 2141-2154.

[10] Wilford J. Mapping Ancient Civilzation, in a Matter of Days. *New York Times*. 11 May 2010: p.D1. Available from http://www.nytimes.com.

[11] Wired. *Ford Unveils Its First Autonomous Vehicle Prototype* [Online] Available from: http://www.wired.com [Accessed 4 Feb 2014].

[12] Wang G, Liu L, Liu Z, Lü B, Mu R. The application of sea-surface wind detection with Doppler LIDAR in Olympic sailing. *Advances in Atmospheric Sciences*. 2011; 28: 1471-1480.

[13] Amzajerdian F, Pierrottet D, Petway L, Hines G, Roback V. LIDAR systems for precision navigation and safe landing on planetary bodies. Proc. of SPIE; 2011; Vol. 8192.

[14] Klipp E. *How LIDAR works.* [Image online]. Available from: http://soundwaves.usgs.gov/2010/02/meetings5.html [Accessed 20 Jan 2014].

[15] Hariharan P. *Basics of interferometry*. Amsterdam: Elsevier Academic Press; 2007.

[16] Genest J, Tremblay P. *GEL 66010 Understanding Fourier-transform Spectrometers Course Manual.* Université Laval; 2008.

[17] ScienceWorld Wolfram. *Fourier-transform Spectrometer Setup*. [Image online]. Available from: http://scienceworld.wolfram.com [Accessed 25 Jan 2014].

[18] Kauppinen J, Partanen J. *Fourier transforms in spectroscopy*. Weinheim: Wiley-VCH; 2001.

[19] Léna P, Mugnier L. *Observational astrophysics*. Heidelberg: Springer-Verlag Berlin Heidelberg; 2012.

[20] Morel E, Torga J. Spectral low coherence interferometry: A complete analysis of the detection system and signal processing. In: Padron I. (eds.) *Interferometry - research and applications in science and technology*. InTech; 2012.

[21] Hee M, Izatt J, Swanson E, Huang D, Schuman J, Lin C, Puliafito C, Fujimoto J. Optical coherence tomography of the human retina. *Archives of Ophthalmology*. 1995; 113 (3): 325-332.

[22] Brezinski M. *Optical coherence tomography*. Burlington, Mass.: Elsevier Academic Press; 2006.

[23] Novacam. *How LCI works*. [Online] Available from: http://www.novacam.com [Accessed 5 Feb 2014].

[24] Fercher A, Drexler W, Hitzenberger C, Lasser T. Optical coherence tomography - principles and applications. *Reports on progress in physics*. 2003; 66 (2): 239-303.

[25] Leitgeb R, Hitzenberger C, Fercher A. Performance of fourier domain vs. time domain optical coherence tomography. *Optics Express*. 2003; 11 (8): 889-894.

[26] Stifter D. Beyond biomedicine: a review of alternative applications and developments for optical coherence tomography. *Applied Physics B*. 2007; 88 (3): 337-357.

[27] Zheng J. *Optical frequency-modulated continuous-wave interferometry*. New York: Springer; 2005.

[28] Thorlabs Inc. *Thorlabs - Swept Source OCT Systems Specifications Sheet*. Available from http://www.thorlabs.com [Accessed 20 Mar 2014].

[29] Dieckmann A. FMCW-LIDAR with tunable twin-guide laser diode. *Electronics Letters*. 1994; 30 (4): 308-309.

[30] Nöding M, Amann M. FMCW-lidar with widely tunable laser diodes: influence of the tuning behaviour on the distance measurement. *Journal of optics*. 1998; 29 (3): 212.

[31] Pierrottet D, Amzajerdian F, Petway L, Barnes B, Lockard G, Rubio M. Linear FMCW laser radar for precision range and vector velocity measurements. 2008; 1076: 1076-04.

[32] Gao S, Hui R. Frequency-modulated continuous-wave lidar using I/Q modulator for simplified heterodyne detection. *Optics Letters*. 2012; 37 (11): 2022-2024.

[33] Baumann, E., Giorgetta, F. R., Coddington, I., Sinclair, L. C., Knabe, K., Swann, W. C. and Newbury, N. R. 2013. Comb-calibrated frequency-modulated continuous-wave ladar for absolute distance measurements. *Optics letters*, 38 (12), pp. 2026-2028.

[34] Lumetrics Inc. *OptiGauge MLS – Precision MultiLayer Thickness Measurement System Data Sheet*. Available from http://www.lumetrics.com [Accessed 3 Feb 2014].

[35] Novacam. *Microcam Profilometer Systems Data Sheet*. Available from http://www.novacam.com [Accessed 3 Feb 2014].

[36] Filmetrics. *F20 & F70 Thin Film Analyzer Data Sheets*. Available from http://www.filmetrics.com [Accessed 3 Feb 2014].

[37] Bridger Photonics. *SLM Series Absolute Distance Measurement Systems Brochure*. Available from http://www.bridgerphotonics.com [Accessed 3 Feb 2014].

[38] Patten R. Michelson interferometer as a remote gauge. *Applied Optics*. 1971; 10 (12): 2717-2721.

[39] Sorin W, Gray D. Simultaneous thickness and group index measurement using optical low-coherence reflectometry. *Photonics Technology Letters, IEEE*. 1992; 4 (1): 105-107.

[40] Coppola G, Ferraro P, Iodice M, De Nicola S. Method for measuring the refractive index and the thickness of transparent plates with a lateral-shear, wavelength-scanning interferometer. *Applied optics*. 2003; 42 (19): 3882-3887.

[41] Kim S, Na J, Kim M, Lee B. Simultaneous measurement of refractive index and thickness by combining low-coherence interferometry and confocal optics. *Optics express*. 2008; 16 (8): 5516-5526.

[42] Taurand G. *Mesures de réflectométrie prises avec un interféromètre à peignes de fréquence*. M.Sc. Thesis. Université Laval; 2010.

[43] Fathi M, Donati S. Thickness measurement of transparent plates by a self-mixing interferometer. *Optics letters*. 2010; 35 (11): 1844-1846.

[44] Fathi M, Donati S. Simultaneous measurement of thickness and refractive index by a single-channel self-mixing interferometer. *Optoelectronics, IET*. 2012; 6 (1): 7-12.

[45] Hussain B, Nawaz M, Ahmed M, Raja M. Measurement of thickness and refractive index using femtosecond and terahertz pulses. *Laser Physics Letters*. 2013; 10 (5): 055301.

[46] Precision Photonics. *Etalon Introduction Technical Paper*. Available from http://www.precisionphotonics.com [Accessed 6 Feb 2014].

[47] Thorlabs - Tutorials. Available from: http://www.thorlabs.com/tutorials [Accessed 17 Apr. 2014].

[48] Burrows E, Liou K. High resolution laser LIDAR utilizing two-section distributed feedback semiconductor laser as a coherent source. *Electronics Letters*. 1990; 26 (9): 577-579.

[49] Saleh B, Teich M. *Fundamental of photonics.* New York: Wiley; 1991.

[50] Desbiens R, Boudreau S, Genest J. *Algorithms*. DRDC Valcartier Contractor Report 2013 – TBD.

[51] Abramowitz M. Specular and Diffuse Reflection. *Molecular Expressions Optical Microscopy Primer*. Available from http://micro.magnet.fsu.edu. [Accessed 1 Feb 2014].

[52] Buus J, Amann M, Blumenthal D, Amann M. *Tunable laser diodes and related optical sources*. Hoboken, N.J.: John Wiley & Sons; 2005.

[53] Johnson, L. A. 2006. Laser diode burn-in and reliability testing. Communications Magazine, IEEE, 44 (2), pp. 4-7.

[54] Optoplex Corporation. *90-Degree Optical Hybrid Data Sheet*. Available from http://www.optoplex.com. [Accessed 6 Feb 2014].

[55] National Instruments Corporation. *Characteristics of Different Smoothing Windows*. Available from http://www.zone.ni.com [Accessed 15 April 2014].

[56] Refractive Index Database. *Refractive Index.INFO*. Available from http://www.refractive index.info [Accessed 22 April 2014].

[57] Thorlabs. *Thorlabs Product Information*. Available from http://www.thorlabs.com [Accessed 23 April 2014].

Appendix A Experimental Setup Components

The following table outlines the components used in the outdoors experimental setup.

Table 19 – Experimental Setup Components.		
Name	**Item**	**Description**
Function Generator	Agilent 33120A	COPL: 4235 S/N: MY-4000-1460
Laser Diode Control Module	ILX Lightwave LDC 3900	Combination Module 39427 COPL: 441279
DFB Laser Diode	HP LSC 2641/C2	λ_0 = 1562.233 nm
Polarization Controller	Thorlabs FPC030	1 in. diameter spool
Fibre Optic Coupler		90/10 Split
Fibre Optic Coupler		50/50 Split
Polarization Controller	Newport F-POL-PT	Length of Fibre: 2.4388 m
Optical Hybrid	Optoplex 90^o Optical Hybrid	COPL: 638107-B S/N: ULA H09 002
Detector (0^o)	Thorlabs PDA 10CS	COPL: 528 709 80% Coupling
Detector (90^o)	Thorlabs PDA 10CS	COPL: 528 709 20% Coupling
Detector (0^o) Power Supply	GlobTek Inc GT-51084-12N12	COPL: 1111
Detector (90^o) Power Supply	GlobTek Inc GT-51084-12N12	COPL: 2009
EDFA Pre-Amp	INO FAD-180	S/N: FO-188
EDFA Power Amp	Pritel LNHPFA-37-IO	S/N: 1807-10-006
Fibre Collimator	OZ Optics LPC-03-1550-9/125-5-0.4-1.81GR-40-3-3-1	S/N: 11964-02
Beam Expander	Edmund Optics NT55-579	20x Magnifying Power, Adjustable
Telescope	Meade LDX75 Series SN-8AT	f = 812 mm, f# = 4 COPL: 633203
Telescope Mount	iOptron Mini Tower Pro	#8100
Beam Splitter	Thorlabs CM1-BP108	8/92 Split
IR Camera	Goodrich ISR Systems 8000-0267 Rev. 13	S/N: 110459878
APD	Princetone Lightwave PLA 841	200µm active area COPL: 779608-C S/N: 039-096
Amplifier	Perkin Elmer Model 5113 Pre-Amp	COPL: 307617 S/N: 46200
Oscilloscope	LeCroy 715Zi	1.5 GHz, 20 GS/s S/N: xx

In addition to the IR camera, the following components were used for the detection subsystem (shown in Figure 42).

Table 20 – Detection Subsystem Items List.

Name in Figure	**Description**
InGaAs Camera	8000-0267 rev13 From Sensors Unlimited
C-mount adapter	Provided with camera
SM1A9	Thorlabs, C-mount to SM1 adapter
SM1V05	SM1 Rotating Adjustable Focusing Element, L = 1/2", 0.32" Travel
SM1T2	SM1 (Ø1.035”-40) Coupler, External Threads, 0.5” Long
SM1D12SZ	SM1-Threaded Zero Aperture Iris, Ø12 mm max aperture
LB1757-C lens	N-BK7 Bi-Convex Lens, Ø1", f = 30.0 mm, ARC: 1050-1620 nm
SM1L05	SM1 Lens Tube, L = 1/2", One Retaining Ring Included
CM1-BP108	Cube-Mounted Pellicle Beam splitter, 8:92, Uncoated, 400-2400 nm
SM1ZM	SM1 Zoom Housing for Ø1" Optics, Non-Rotating, 4 mm Travel
SM1V10	SM1 Rotating Adjustable Focusing Element, L = 1", 0.81" Travel
PF10-03-M01	Ø1" (25.4 mm) Protected Gold Mirror

Appendix B Sample Layer Combinations

Using the data from Table 3 and the knowledge that each layer combination will also generate a peak, we can produce a table with the expected peak positions (sorted in ascending order with the actual layers identified by an asterisk).

Table 21 – Sample Layer Combinations.

Material / ID	Layer Combinations (mm)
Acrylic & BK7	3.184*
	6.12*
	9.304
Acrylic	2.19*
	6.12*
	8.31
Acrylic	2.947*
	6.12*
	9.067
Acrylic & BK7	1.88*
	3.184*
	5.064
	6.12*
	9.304
	11.184
Acrylic	1.88*
	2.19*
	4.827
	6.12*
	8.00
	8.31
	10.19
Acrylic	1.88*
	2.19*
	2.947*
	4.827
	6.12*
	8.00
	8.31
	10.19
	10.947
	13.137
P411	1.80*
	10.4*
	12.2
	15.0*
	16.8
	27.2

P427	2.50*
	12.8*
	15.3
	15.9*
	18.4
	31.2
Unknown_1	1*
	3*
	5*
	5.5*
	6*
	6.5
	7
	8
	10.5
	11.5
	12.5
	13.5
	14.5
	17.5
	20.5

Appendix C MATLAB Code

```
%%%%%%%%%%%%%%%%%%%%%%%%%%%%%%%%%%%%%%%%%%%%%%%%%%%%%%%%%%%%%%%%%%%%%%%%
% Multi Layer Mark 33
% 15 April 2014
% Michel Gosselin
%%%%%%%%%%%%%%%%%%%%%%%%%%%%%%%%%%%%%%%%%%%%%%%%%%%%%%%%%%%%%%%%%%%%%%%%

clear all;
close all;
clc;

%% CONSTANTS

c = 3.0e8;  % Speed of Light

n_BK7 = 1.5005; %Refractive index of BK7 @ 1.562 um
n_Acrylic = 1.48; %Refractive index of acrylic @ 1.0 um
n_FibreOptic = 1.47; %Refractive index of fibre optic cable

% Length of reference interferometer fibre [m]
ref_length = 2.4388; %Calculated using frequency comb pulse (9 sep 2013)

%% DELAY LINE CALIBRATION & ANGLE OF INCIDENCE VERIFICATION

% [tm1 vm1 m1data] = rlecroy('C2sdelai2v400004.trc');
% [tm2 vm2 m2data] = rlecroy('C4sdelai2v400004.trc');
% plot(tm1,vm1)
% % plot(tm1(300:675),vm1(300:675))
% title('Delay Line Calibration');
% xlabel('Time (s)');
% ylabel('Voltage (V)');
%
% x = 0:0.1:45;
% e = 2.0./(2*tand(asind(sind(x)/1.5)));
% plot(x,e)
% xlabel('Angle of Incidence (Degrees)','fontsize',16);
% ylabel('Sample Thickness (mm)','fontsize',16);
% % title('Thickness vs. Angle of Incidence','fontsize',16);
% ylim([0 50]);
% grid on;

%% DATA ACQUISITION

% Input directory where data is stored.
% If data is not separated into individual folders for data to average,
% must identify keyword in variable 'list_C*' to identify data sets.

folder_name = uigetdir('/Users/michelgosselin/Documents/MATLAB/MultiLayer Sample Data');
%For Mac OS X
% folder_name = uigetdir('C:\'); %For Windows PC

list_C2 = dir(['' folder_name '/','C2*.trc']);
```

```
list_C3 = dir(['' folder_name '/','C3*.trc']);
list_C4 = dir(['' folder_name '/','C4*.trc']);

count = length(list_C2); %Number of data sets

file_C2 = list_C2(1).name;
file_C3 = list_C3(1).name;
file_C4 = list_C4(1).name;

[tm1 vm1] = rlecroy(['' file_C2]); %0 Degree Offset
[tm2 vm2] = rlecroy(['' file_C3]); %90 Degree Offset
[tm3 vm3] = rlecroy(['' file_C4]); %MultiLayer Sample

% IMPORTANT - Signals might need to changed depending on setup of channels with oscillscope

signal_ref = vm1;
signal_ref_offset = vm2;
signal_sample = vm3;
% signal_trigger = vm4;
time = tm1;

L = length(time);
freq_sampling = 1/(time(2)-time(1));
fs_lidar = 5e6;
t_lidar = (0:1:L-1)./fs_lidar;

% figure;
% subplot(411),plot(t_lidar,signal_trigger),title('Signal Trigger');
% subplot(412),plot(t_lidar,signal_ref),title('Signal Reference');
% subplot(413),plot(t_lidar,signal_ref_offset),title('Signal Reference Offset');
% subplot(414),plot(t_lidar,signal_sample),title('Signal MultiLayer Sample');

%% FILTERING (1ST ITERATION)

avg_ref = mean(signal_ref);
avg_offset = mean(signal_ref_offset);
avg_sample = mean(signal_sample);

signal_ref_center = signal_ref - avg_ref;
signal_ref_offset_center = signal_ref_offset - avg_offset;
signal_sample_center = signal_sample - avg_sample;

signal_ref_norm = signal_ref_center/max(abs(signal_ref_center));
signal_ref_offset_norm = signal_ref_offset_center/max(abs(signal_ref_offset_center));
signal_sample_norm = signal_sample_center/max(abs(signal_sample_center));

filter_size = 50;
ref_filter_box = ones(filter_size,1)./filter_size;

signal_ref_smoothed = conv(signal_ref_norm,ref_filter_box,'same');
signal_ref_offset_smoothed = conv(signal_ref_offset_norm,ref_filter_box,'same');
```

```
% Compare filtered signal to original
%
% figure
% plot(t_lidar,signal_ref_norm,'black')
% hold on
% plot(t_lidar,signal_ref_smoothed,'green','linewidth',2)
%
% figure
% plot(t_lidar,signal_ref_offset_norm,'black')
% hold on
% plot(t_lidar,signal_ref_offset_smoothed,'green','linewidth',2)
%
% figure
% %subplot(313),plot(t_lidar,signal_trigger_smoothed),title('Signal Trigger');
% subplot(311),plot(t_lidar,signal_ref_smoothed),title('Signal Reference');
% subplot(312),plot(t_lidar,signal_ref_offset_smoothed),title('Signal Reference Offset');
%
% Verify relation between ref and ref offset signal (I&Q)
% Desired result should be perfect circle from -1 to +1 on both x & y-axis
%
% figure
% plot(signal_ref_smoothed,signal_ref_offset_smoothed);
% grid on;
% axis square;
% extremum_max = max([signal_ref_smoothed signal_ref_offset_smoothed]);
% extremum_min = min([signal_ref_smoothed signal_ref_offset_smoothed]);
% xlim([extremum_min extremum_max]);
% ylim([extremum_min extremum_max]);

%% INTERPOLATION OF PHASE & TIME (1ST ITERATION)

phase = atan2(signal_ref_offset_smoothed,signal_ref_smoothed); %Arctan b/w I&Q signals
unrolled_phase = unwrap(phase); %Unwrap phase of I&Q

% Manual selection of start and end points of main slope of unrolled phase
% to perform interpolation.

%Select x vector for 1st iteration.  Use same x for remaining iterations.
dlg = msgbox('SELECT START AND END POINTS OF MAIN SLOPE OF UNROLLED
PHASE.','UNROLLED PHASE','modal');
uiwait(dlg);
f1 = figure;
plot(unrolled_phase)
title('Unrolled Phase of Reference Signal');
xlabel('Number of Points');
ylabel('Unrolled Phase [rad]');
[x,y] = ginput(2);
close(f1)
x = round(x);

% Automatic selection of start and end points of main slope of unrolled
% phase to perform interpolation.  Attempt to find derivative and create
% index of the sign (plus or minus 1).  MATLAB has difficulty due to
% numerous small variations of unrolled phase, even after filtering.
```

```
% upordown = sign(diff(unrolled_phase_smoothed));
% figure
% plot(upordown)

% for n = 1:length(t_lidar)-1
%     if upordown(n) == 1
%         counter(n) = n;
%     else counter(n) = 0;
%     end
%     if n == length(t_lidar)-1
%         break
%     end
% end
%
% for n = 1:length(t_lidar)-2
%     if abs(counter(n+1) - counter(n)) > 1
%         index(n) = n;
%     end
% end
%
% index = unique(index);
%
% if upordown(1) == -1
%     index(1) = [];
% end
% %
% % index = [1,L];
%
% for m = 1:2:length(index)-1
% %    if m == length(index)-1
% %         new_phase(m-1,:) = unrolled_phase(index(m):length(x));
% %         new_time(m-1,:) = x(index(m):length(x));
% %     else
%     new_phase((m+1)/2,:) = unrolled_phase(index(m):index(m+1));
%     new_time((m+1)/2,:) = t_lidar(index(m):index(m+1));
% %     time_interp((m+1)/2,:) = interp1(new_phase((m+1)/2,:),new_time((m+1)/2,:),phase_interp);
% %     signal_sample_interp((m+1)/2,:) =
interp1(new_time((m+1)/2,:),signal_sample_norm(1,:),time_interp((m+1)/2,:));
% % %     end
% end

new_phase = unrolled_phase(min(x):max(x)); %Keep unrolled phase from selected x interval
new_phase_smoothed = smooth(new_phase)';
new_time = t_lidar(min(x):max(x)); %Keep time from selected x interval
if y(1) < y(2) %Determine if slope of new phase is (+) or (-)
   phase_interp =
(2*pi)*(round(new_phase_smoothed(1)/(2*pi))):(1/16)*pi:round(new_phase_smoothed(end));
else
   phase_interp = (2*pi)*(round(new_phase_smoothed(1)/(2*pi))):-
(1/16)*pi:round(new_phase_smoothed(end));
end

signal_test = detrend(signal_sample_norm(min(x):max(x))); %Detrend sample signal
time_interp = interp1(new_phase_smoothed,new_time,phase_interp,'spline','extrap'); %Each time
value where phase = 2*pi
```

```
signal_sample_interp = interp1(new_time,signal_test,time_interp,'spline','extrap'); %Each sample
signal value where phase = 2*pi

%% FOURIER TRANSFORM (1ST ITERATION)

interp_length = length(signal_sample_interp);

window = hamming(interp_length);

signal_sample_interp_window = signal_sample_interp .* window';

NFFT = 2^nextpow2(interp_length); %Next power of 2 from length of y

sample_fft = ifft(signal_sample_interp_window,NFFT);

sample_fft_sum = zeros(count,length(sample_fft));
sample_fft_sum(1,:) = sample_fft; %Build sample fft vector in order to average

phase_array = zeros(count,length(phase));
phase_array(1,:) = unrolled_phase; %Build phase vector for comparison
phase_size(1,:) = length(phase);

h = waitbar(0,'PROCESSING MULTIPLE DATA ENTRIES.  PLEASE WAIT...');

%% SECOND ITERATION TO BUILD FFT VECTOR

%% DATA ACQUISTION (2ND ITERATION)

for j = 2:count
    file_C2 = list_C2(j).name;
    file_C3 = list_C3(j).name;
    file_C4 = list_C4(j).name;

    [tm1 vm1] = rlecroy(['' file_C2]); %0 Degree Offset
    [tm2 vm2] = rlecroy(['' file_C3]); %90 Degree Offset
    [tm3 vm3] = rlecroy(['' file_C4]); %MultiLayer Sample

% IMPORTANT - Signals might need to changed depending on setup of channels
% with oscillscope / Signaux doivent possiblement Ítre changÈs dÈpendant
% de la configuration des canaux sur l'oscilloscope.

signal_ref = vm1;
signal_ref_offset = vm2;
signal_sample = vm3;

%% FILTERING (2ND ITERATION)

% If this error messages appears, it is possible that some trace files were
% not saved properly for all channels, ie. only one '38.trc' exists rather
% than four.
% "Error using conv (line 27)
% A and B must be vectors.
%
```

```
% Error in MultiLayer_Mark_30 (line 309)
% signal_sample_smoothed = conv(signal_sample_norm,sample_filter_box,'same');

avg_ref = mean(signal_ref);
avg_offset = mean(signal_ref_offset);
avg_sample = mean(signal_sample);

signal_ref_center = signal_ref - avg_ref;
signal_ref_offset_center = signal_ref_offset - avg_offset;
signal_sample_center = signal_sample - avg_sample;

signal_ref_norm = signal_ref_center/max(abs(signal_ref_center));
signal_ref_offset_norm = signal_ref_offset_center/max(abs(signal_ref_offset_center));
signal_sample_norm = signal_sample_center/max(abs(signal_sample_center));

filter_size = 50;
ref_filter_box = ones(filter_size,1)./filter_size;

signal_ref_smoothed = conv(signal_ref_norm,ref_filter_box,'same');
signal_ref_offset_smoothed = conv(signal_ref_offset_norm,ref_filter_box,'same');

%% INTERPOLATION OF PHASE & TIME (2ND ITERATION)

phase = atan2(signal_ref_offset_smoothed,signal_ref_smoothed); %ArcTan b/w I&Q signals
unrolled_phase = unwrap(phase); %Unwrap phase of I&Q
phase_array(j,:) = unrolled_phase;
phase_size(j,:) = length(phase);

% Manual selection of start and end points of main slope of unrolled phase to perform interpolation.

% X points have been determined in 1st iteration.
% If loop to ensure phase length has not changed.

if phase_size(j) ~= phase_size(j-1) %Compare size of phase from previous signal; if NOT EQUAL,
request new start and end points
    dlg = msgbox('DATA LENGTH IS DIFFERENT FROM PREVIOUS ENTRIES. RE-SELECT
START AND END POINTS OF MAIN SLOPE OF UNROLLED PHASE.','UNROLLED
PHASE','warn','modal');
    uiwait(dlg);
    f1 = figure;
    plot(unrolled_phase)
    title('Unrolled Phase of Reference Signal');
    xlabel('Number of Points');
    ylabel('Unrolled Phase [rad]');
    [x,y] = ginput(2);
    close(f1)
    x = round(x);
end

% Waitbar
waitbar(j/count,h);

new_phase = unrolled_phase(min(x):max(x)); %Keep unrolled phase from selected x interval
new_phase_smoothed = smooth(new_phase)';
```

```
new_time = t_lidar(min(x):max(x)); %Keep time from selected x interval
if y(1) < y(2) %Determine if slope of new phase is (+) or (-)
    phase_interp =
(2*pi)*(round(new_phase_smoothed(1)/(2*pi))):(1/16)*pi:round(new_phase_smoothed(end));
else
    phase_interp = (2*pi)*(round(new_phase_smoothed(1)/(2*pi))):-
(1/16)*pi:round(new_phase_smoothed(end));
end

signal_test = detrend(signal_sample_norm(min(x):max(x))); %Detrend sample signal
time_interp = interp1(new_phase_smoothed,new_time,phase_interp,'spline','extrap'); %Each time
value where phase = 2*pi
signal_sample_interp = interp1(new_time,signal_test,time_interp,'spline','extrap'); %Each sample
signal value where phase = 2*pi
% signal_sample_interp = smooth(signal_sample_interp)';

%% FOURIER TRANSFORM (2ND ITERATION)

interp_length = length(signal_sample_interp);

window = hamming(interp_length);

signal_sample_interp_window = signal_sample_interp .* window';

sample_fft = ifft(signal_sample_interp_window,NFFT);

sample_fft_sum(j,:) = sample_fft; %Build sample fft vector in order to average

end %End of for loop for 2nd iteration to build fft vector

close(h);

%% FIGURE(S) PLOTTING

x_axis = 32*(1/2)*1000*n_FibreOptic*ref_length*linspace(0,1,NFFT); %x axis of fft

rows = length(sample_fft_sum(:,1));

% Figure naming convention
file_name = folder_name(74:end);
average = 'Average';
individual = 'Individual';
phase = 'Phase';

file_name_avg = [file_name '_' average];
file_name_ind = [file_name '_' individual];
file_name_phase = [file_name '_' phase];

% Average IFFT of sample
sample_fft_average = sum(sample_fft_sum)./rows; %Place in comment if sample_fft_final in use

figure
plot(x_axis(1:NFFT/2),abs(sample_fft_average(1:NFFT/2)./max(sample_fft_average(1:NFFT/2))))
```

```
xlabel('Effective Thickness (mm)','fontsize',16);
ylabel('Normalized Amplitude (a.u.)','fontsize',16);
xlim ([0 50]);
ylim ([0 1.2]);
hold on;

auto_corr = abs(sample_fft_average(1:NFFT/2)./max(sample_fft_average(1:NFFT/2)));

[pks,locs] = findpeaks(auto_corr./max(auto_corr),'MINPEAKHEIGHT',0.40);

Peak = zeros(1,length(pks));

for n=1:length(pks) %Location of peaks
   Peak(n) = abs(x_axis(locs(n)));
end

for m=1:length(pks)
   plot(Peak(m),pks(m),'*r','linewidth',1);
end

% print ('-dpng','-r720',file_name) %Export graphics figure to MATLAB directory

disp(Peak);
disp(pks);
```